DIGITAL SELF-INTERFERENCE CANCELLATION FOR IN-BAND FULL-DUPLEX COMMUNICATION

by
HAYRETTİN AYAR

Submitted to the Graduate School of Engineering and Natural Sciences
in partial fulfilment of
the requirements for the degree of Doctor of Philosophy

Sabancı University
December 2021

DIGITAL SELF-INTERFERENCE CANCELLATION FOR IN-BAND FULL-DUPLEX COMMUNICATION

Approved by:

Approval: December 16, 2021

Hayrettin Ayar 2021 ©

All Rights Reserved

ABSTRACT

DIGITAL SELF-INTERFERENCE CANCELLATION FOR IN-BAND FULL-DUPLEX COMMUNICATION

HAYRETTİN AYAR

EE, Ph.D DISSERTATION, DECEMBER 2021

Dissertation Supervisor: Prof. ÖZGÜR GÜRBÜZ

Keywords: in-band full-duplex, self-interference, linear digital self-interference cancellation, non-linear self-interference cancellation, neural networks, cyclic prefix noise, orthogonal frequency division multiplexing, FPGA implementation, software defined radio

By allowing simultaneous transmit and receive operations in the same frequency band, In-Band Full-Duplex (IBFD) communication has been proven as a new technology with the potential of a two fold increase in spectral efficiency, as compared to the conventional half-duplex systems. However, as the transmitter creates a high level of self-interference (SI) at the receiver on the same radio, considerable amount of SI cancellation is required for achieving this gain and successfully decoding the signal-of-interest (SoI) arriving from the distant node. For this purpose, in IBFD radios, various SI cancellation techniques are proposed to suppress the SI signal by employing propagation domain antenna suppression, analog domain cancellation, and non-linear and linear digital SI cancellation in the literature. In this thesis, we study linear digital SI cancellation techniques and non-linearity problem induced by the hardware components on the IBFD radios, considering Orthogonal Frequency Division Multiplexing (OFDM) based wireless systems.

OFDM is the pertinent waveform for current and next generation wireless systems, whose spectral efficiency can be potentially doubled by IBFD communication. However, in OFDM based IBFD systems, linear digital self-interference cancellation (DSIC) employed at baseband does not provide sufficient cancellation in the cyclic prefix (CP) region. When the propagation delay between two communicating radios is non-zero, the CP noise affects the data region of the desired signal. In the first

part of this thesis, we propose CP noise reduction (CPNR) technique for OFDM based IBFD radios. In the CPNR solution, we enhance SI channel estimation and SI signal reconstruction for time and frequency DSIC techniques. We have evaluated CPNR with time and frequency domain DSIC via both simulations as well as MATLAB and FPGA implementations on our Software Defined Radio (SDR) based IBFD radio. In the laboratory tests, the total suppression of the IBFD radio is improved by 6 dB by employing CPNR in frequency-domain DSIC and EVM for bidirectional communication is improved by up to 5%, allowing realistic propagation delays. In addition to improving the total suppression and EVM performance, CPNR is also shown to enhance the multi-path resiliency of DSIC techniques.

In the second part of the thesis, we consider the non-linearity problem in IBFD radios at high transmit power levels, and we propose a new architecture along with time and frequency domain non-linear estimation algorithms. In this architecture, non-linear and linear SI cancellation stages are isolated via an RF switch, so that non-linear estimation can be performed separately from and prior to linear SI cancellation. Following one of the alternative proposed estimation algorithms, the non-linear SI signal is obtained as a reference to linear SI cancellation. Our experimental results obtained on OFDM based IBFD SDR set-up demonstrate that the amount of total SI suppression is improved by up to 13 dB over state-of-the-art digital, integrated linear and non-linear SI cancellation schemes. Moreover, in our solution, since non-linear estimation is decoupled from SI channel estimation, the SI cancellation performance is immune to changes in the (multi-path) environment; unlike existing schemes, which require re-optimization of model parameters for each setting. Last but not least, estimation overhead for digital SI cancellation is eliminated, and computational complexity is lowered by four to six orders-of-magnitude with the proposed algorithms.

ÖZET

BANT İÇİ TAM ÇİFT YÖNLÜ HABERLEŞME İÇİN SAYISAL ÖZGİRİŞİM GİDERİMİ

HAYRETTİN AYAR

EE, DOKTORA TEZİ, ARALIK 2021

Tez Danışmanı: Prof. Dr. ÖZGÜR GÜRBÜZ

Anahtar Kelimeler: bant içi tam çift yönlü, öz girişim, doğrusal sayısal öz girişim giderimi, doğrusal olmayan öz girişim giderimi, sinir ağları, döngüsel önek gürültüsü, dikgen frekans bölmeli çoklama, FPGA geliştirme, yazılım tanımlı radyo

Bant İçi Tam Çift Yönlü (BİTÇY) iletişimin, geleneksel yarı çift yönlü ile karşılaştırıldığında, aynı frekans bandında eşzamanlı gönderme ve alma işlemlerine olanak sağlayarak spektral verimlilikte iki kat artış potansiyeline sahip yeni bir teknoloji olduğu kanıtlanmıştır. Bununla birlikte, aynı radyodaki alıcıda yüksek düzeyde öz girişim (ÖG) oluştuğundan, bu kazancı elde etmek ve uzak radyodan gelen İstenen Sinyal'i (İS) başarılı bir şekilde çözmek için önemli miktarda ÖG giderimi gerekmektedir. Bu amaçla, BİTÇY radyolarda, literatürde anten düzeyinde ÖG giderimi, analog ÖG giderimi ve doğrusal ve doğrusal olmayan sayısal ÖG giderimi kullanılarak ÖG sinyalini bastırmak için çeşitli teknikler önerilmiştir. Bu tezde, Dikgen frekans bölmeli çoklama (DFBÇ) tabanlı kablosuz sistemler için doğrusal sayısal ÖG giderim teknikleri ve BİTÇY radyolardaki donanım bileşenlerinin neden olduğu doğrusal olmayan etkiler üzerinde çalışılmaktadır.

DFBÇ, spektral verimliliği BİTÇY iletişim ile potansiyel olarak ikiye katlanabilen mevcut ve yeni nesil kablosuz sistemler için uygun bir dalga biçimidir. Ancak, DFBÇ tabanlı BİTÇY sistemlerde, temel bantta kullanılan doğrusal sayısal OG (SÖGG), döngüsel önek (DÖ) bölgesinde yeterli giderim sağlamamaktadır. İletişim kuran iki radyo arasındaki yayılma gecikmesi sıfır olmadığında, DÖ gürültüsü İS'nin veri bölgesini etkilemektedir. Bu tezin ilk kısmında, DFBÇ tabanlı BİTÇY radyolar için DÖ gürültü azaltma (DÖGA) tekniğini öneriyoruz. DÖGA çözümünde, zaman ve frekans alanlı SÖGG tekniklerindeki ÖG kanal kestirimi ve ÖG sinyali yeniden oluşturma iyileştirilmektedir. DÖGA'yı, Yazılım Tanımlı Radyo (YTR) tabanlı

BİTÇY radyomuzda hem simülasyonlar hem de MATLAB ve FPGA uygulamaları aracılığıyla zaman ve frekans alanı SÖGG teknikleri ile değerlendirdik. Laboratuvar testlerinde, frekans alanlı SÖGG'de DÖGA kullanılarak BİTÇY radyonun toplam bastırılması 6 dB iyileştirildi ve çift yönlü iletişim için Hata Vektör Genliği (HVG), gerçekçi yayılma gecikmelerine için %5'e kadar iyileştirildi. Toplam bastırma ve HVG performansını iyileştirmeye ek olarak, DÖGA'nın SÖGG tekniklerinin çok yollu esnekliğini artırdığı da gösterilmiştir.

Tezin ikinci kısmında, BİTÇY radyolarda yüksek gönderim güçlerindeki doğrusal olmayan problemi ele alarak yeni bir BİTÇY mimarisi ile zaman ve frekans alanında doğrusal olmayan kestirim algoritmaları önermekteyiz. Bu yeni mimaride, doğrusal olmayan ve doğrusal ÖG giderimi aşamaları bir RF anahtarı aracılığıyla izole edilmektedir, böylece doğrusal olmayan kestirim, doğrusal ÖG gideriminden ayrı olarak ve öncesinde gerçekleştirilebilmektedir. Önerilen alternatif kestirim algoritmalarından birinin ardından, doğrusal olmayan ÖG sinyali, doğrusal ÖG giderimi aşamasına referans olarak sağlanmaktadır. DFBÇ tabanlı BİTÇY YTR düzeneğinde elde edilen deneysel sonuçlarımız, toplam ÖG bastırım miktarının, son teknolojii entegre doğrusal ve doğrusal olmayan ÖG giderimi yöntemlerine göre 13 dB'ye kadar iyileştirildiğini göstermektedir. Ayrıca, çözümümüzde doğrusal olmayan kestirm, doğrusal ÖG kanal kestiriminden ayrıştırıldığından, model parametrelerinin yeniden optimize edilmesini gerektiren mevcut yöntemlerden farklı olarak, ÖG giderim performansı çok yollu ortamdaki değişikliklere karşı bağışıktır. Son olarak, sayısal DÖGG için kestirim yükü tamamıyla giderilmiş ve hesaplama karmaşıklığı, önerilen doğrusal olmayan kestirim algoritmalarıyla dört ila altı büyüklük sırasına kadar düşürülmüştür.

ACKNOWLEDGEMENTS

First of all, I would like to express my sincere gratitude to my thesis supervisor, Dr. Özgür GÜRBÜZ, for her guidance and suggestions throughout my research. Without her consistent support, continuous inspiration and motivating guidance, this thesis could not have been completed. I would like to thank the members of my thesis committee, Dr. İbrahim TEKİN, Dr. Hüsnü YENİGÜN, Dr. Sinem ÇÖLERİ and Dr. Ali Emre PUSANE for reviewing the thesis and for serving in the committee. I would like to extend my special thanks to Dr. İbrahim TEKİN and Dr. Hüsnü YENİGÜN for their valuable advises and guidance during my progress meetings.

My deepest gratitude goes to my parents who gave me birth and brought me up and passed away long time ago. I also would like to thank my family in law for their invaluable support and prayers throughout this process.

No words of thanks can sum up the gratitude that I owe to my beloved wife, Canan AYAR, for her continuous support, patience and understanding during my study. Her prayer for me was what sustained me this far.

Finally, I would also like to thank The Scientific and Technological Research Council of Turkey (TÜBİTAK) for the financial support during my study.

to my family

TABLE OF CONTENTS

LIST OF TABLES

LIST OF FIGURES

LIST OF ABBREVIATONS

HDL Hardware Description Language 77

HVG Hata Vektör Genliği vii

IBFD In-Band Full-Duplex 21

IBFD-SW Switched IBFD Radio 46

IFFT Inverse Fast Fourier Transform 16

LNA Low Noise Amplifier 53

LS Least Squares 14

LTS Long Training Sequence 27

LUT Lookup Table 103

MP Memory Polynomial 18

NLC Non-linear Complex Estimation 49

NLF Non-linear Frequency-Domain Estimation 51

NLP Non-linear Polar Estimation 49

NN Neural Network 19

OFDM Orthogonal Frequency Division Multiplexing 21

OG Öz Girişim vi

PA Power Amplifier 53

PC Personal Computer 77

PL Programmable Logic 77

PS Processor System 77

RAM Random Access Memory 92

RF Radio Frequency 53

rms Root Mean Square 32

RSSI Received Signal Strength Indicator 106

SDK Software Development Kit 78

SDR Software Defined Radio 36

SI Self-Interference 14

SNR Signal-to-Noise Ratio 33

SoI Signal-of-Interest 14

SÖGG Sayısal Öz Girişim Giderimi vi

TDL Tapped Delay Line 32

TE Time-Domain Estimation 14

TE-FR Time-Domain Estimation Frequency-Domain Reconstruction 17

TE-TR Time-Domain Estimation Time-Domain Reconstruction 17

TR Time-Domain Reconstruction 16

XPS Xilinx Platform Studio 78

XSG Xilinx System Generator 78

YTR Yazılım Tanımlı Radyo vi

1. INTRODUCTION

Increased demand for high data rates in wireless networks has accelerated technologies promising improved spectral efficiency. One of the proposed solutions is in-band full-duplex (IBFD) wireless communication, where a radio frequency (RF) transceiver transmits and receives signals simultaneously in the same band [1], [7], [8], [9], [10], [11], resulting improved spectral efficiency approximately by a factor of two [12], [13]. For 5G Advanced systems, IBFD communication is not only expected to support the demand for high throughput services, low-latency applications and seamless global roaming, but it will also be employed in spectrum virtualization, novel relaying/backhaul solutions and enhanced interference coordination [14], [15]. Moreover, by utilizing IBFD at the base stations, cross-division duplex (allowing simultaneous downlink and uplink operation within the same time slot) can be employed to enhance uplink coverage in time division duplex (TDD) carriers [16]. Another application of IBFD is joint/simultaneous communication and sensing and cognitive radio, which are upcoming features of 6G systems [17].

The main challenge in realizing the IBFD communication is the strong self-interference (SI) signal introduced at the receiver, due to the limited isolation between the transmitter and receiver chains on the same radio [18]. Since the propagation path for the SI signal is shorter than that of the signal of interest (SoI) arriving from a distant radio, the SI signal at the receiver is much stronger than SoI [19]. In order to receive the SoI with acceptable quality, SI has to be reduced to the receiver's noise level. For this purpose, in IBFD radios, SI cancellation techniques are applied at different stages [1, 3, 4, 7, 12, 18–27]: Passive suppression is achieved at the antenna level either by isolating the transmit antenna and receive antenna of the same node by means of physical separation [21] or by ensuring horizontal and vertical polarization for a single antenna [25]. Analog cancellation is achieved by circuits employing active analog components [26]. Digital SI cancellation (DSIC) is applied as the last step at the baseband level, where first the SI channel is estimated, then the SI signal is reconstructed, followed by subtraction of the reconstructed signal from the received signal [4], [18], [21], [27]. By cancelling the SI signal without disturbing the SoI, IBFD communication between two nodes can be established.

Today's broadband wireless systems are mostly based on orthogonal frequency division multiplexing (OFDM), due to the high data rates provided with high multi-path resiliency, as in 4G cellular [28], IEEE 802.11 Wireless Local Area Networks (WLANs) [29], WiMAX [30] etc. For this reason, DSIC techniques for IBFD communication are designed mostly for OFDM based physical layer [1], [4], [18], [21]. In [1] and [27], we have evaluated different DSIC techniques, where minimum mean square error and least squares approaches applied in time-domain estimation (abbreviated as TE) or frequency-domain estimation (FE) of the SI channel, followed with time-domain reconstruction (TR) or frequency-domain reconstruction (FR) of the SI signal. Via detailed simulations and tests on WARP v3 OFDM based IEEE 802.11g software defined radio (SDR) board, time-domain DSIC was shown to provide outperform frequency-domain DSIC when there is no or small multi-path, while the opposite was observed under severe multi-path. In [7], we have integrated time-domain DSIC with different monostatic antennas on our SDR based test-bed and we have obtained performance limits and characterization of the proposed IBFD radio architecture.

For 5G, 3rd Generation Partnership Project (3GPP) group has declared that an OFDM waveform with cyclic prefix (CP) is supported [31]. The CP at the beginning of each OFDM symbol provides a guard interval for avoiding inter-symbol interference (ISI), i.e., leakage, induced by the multi-path channel effects. However, CP-enabled OFDM involves challenges in DSIC for IBFD communication: When CP is appended at the beginning of an OFDM symbol, the symbol duration is increased and the frequency-domain orthogonality of the waveforms is disturbed. As a result, the neighbour sub-carriers interfere with the guard sub-carriers in the channel. DSIC (time and frequency domain, i.e., TE and FE, methods) cannot completely estimate, hence cannot completely suppress the SI signal, unless the interference on the guard sub-carriers is estimated. Additional noise is introduced in frequency-domain reconstruction (FR), when ISI (i.e., leakage) between OFDM symbols is not correctly reflected. In our simulations in [32], we have observed the effect of both estimation and ISI errors, resulting in ripples on the residual SI signal, which we have named as *CP noise*. In practical realistic scenarios, due to propagation delay between the nodes, the CP and data regions of the two nodes will not be aligned. Then, the CP region of one node will appear in the data region of the other node and it will interfere with the SoI, eventually degrading SI cancellation. Therefore, the CP noise problem should be alleviated to allow IBFD communication in OFDM systems in realistic, asynchronous scenarios.

In the first part of this thesis, we investigate the CP noise problem in OFDM based IBFD radios, considering all linear DSIC techniques, TE-TR, TE-FR, FE-TR and

FE-FR, employing time or frequency domain SI channel estimation and SI signal reconstruction. Then, we propose a novel solution, named Cyclic Prefix Noise Reduction (CPNR), composed of two steps: 1) Additional training tones are inserted into the guard sub-carriers within the communication band, during training period, covering the transition region between two OFDM symbols, so as to obtain enhanced SI channel estimates. 2) An additional new reconstruction technique is introduced in frequency-domain for reconstructing the transition regions. We present detailed performance evaluation of the CPNR solution via simulations as well as tests on our IBFD radio SDR set-up and the Field Programmable Gate Array (FPGA) implementation. We show that CPNR is crucial for OFDM based IBFD radios not only for improving total SI cancellation, but also for allowing IBFD communication in realistic, asynchronous scenarios.

As demonstrated in experimental results in [1], [3] and [7], the performance of linear SI cancellation, although maximized with CPNR, is degraded at high transmit power levels. This is due to the fact that the SI signal is distorted in linear as well as non-linear fashion until it arrives to the baseband chain of the receiver. The received baseband SI signal is distorted not only linearly by the SI channel, but also in a non-linear fashion, due to the power amplifier (PA) on the transmit chain and low noise amplifier (LNA) on the received chain, at high transmit power levels. The effects of non-linearity are analyzed and non-linear only and/or integrated non-linear and linear SI cancellation schemes have been extensively studied in the literature: The memory polynomial (MP) is the main non-linear DSIC technique employed in IBFD radios [4, 5, 18, 20, 33–39]. In [4], non-linear and linear effects are estimated together with the MP model at the baseband level by utilizing the long training sequences (LTS) in the preamble of a packet. The estimation is performed at eight times higher sampling rate requiring modification of the hardware. Here, the coefficients of the MP model are estimated at each transmission resulting in high computational cost. For reduced complexity, orthogonalized least mean squares (OLMS) and a recursive least squares (RLS) are apllied in [37] and [38], respectively, while providing similar performance to the MP model. In conjunction with linear DSIC, neural network (NN) based DSIC solutions are proposed in [39], utilizing real-valued NN, complex-valued NN, and recurrent NN. However, NN based solutions are not able to provide higher total SI cancellation than the MP model although they reduce the computational complexity of the MP model. Moreover, they are all implemented in time-domain being subject to non-linear and linear SI effects. In the abovementioned solutions, if there is a change in the multi-path environment, update on the the non-linear model is required and hence the coefficients need to be re-estimated for the new channel causing excessive estimation overhead. Furthermore, they employ active

analog cancellation curcuitry considered as additional hardware cost. In another solution proposed in [2], an auxiliary receive chain is used to provide a reference non-linear SI signal to linear SI cancellation at the expense of additional hardware.

In the second part of this thesis, we propose decoupling linear and non-linear SI cancellation via a new, switched IBFD radio architecture (IBFD-SW), which can be easily implemented by simple hardware additions on a conventional half-duplex radio. On the IBFD-SW radio architecture, we propose time-domain and frequency-domain algorithms for estimating the non-linear SI signal, which is provided as a reference to linear cancellation. With our solution, not only significant performance improvement (up to 13 dB higher SI cancellation) is obtained over prominent digital non-linear SI cancellation schemes, but also robust multi-path resiliency is achieved at no (estimation) overhead and notably reduced computational complexity cost.

1.1 Thesis Contributions

The contributions and main findings of this thesis can be summarized as follows:

- The CP noise problem in OFDM based IBFD radio is introduced and analyzed, addressing the issues in SI channel estimation, issues in SI signal reconstruction, and issues in IBFD communication.
- The performance of the proposed CPNR solution is investigated first via extensive simulations, considering all DSIC techniques under additive white Gaussian noise (AWGN) and IEEE 802.11 indoor channel model, modeling multi-path and time varying channel effects on the SI channel. It is shown that the amount of performance improvement by CPNR depends on the DSIC scheme employed, channel SNR and multi-path. As an example, for 25 dB SNR and 75 ns *rms* delay spread, by employing CPNR, 7-8 dB higher digital cancellation is obtained for DSIC with FR (TE-FR and FE-FR) and only 0.5-2.5 dB is achieved for DSIC with TR (TE-TR and FE-TR), as compared to the respective cases without CPNR. As multi-path gets more severe, the improvement by CPNR increases up to 10 dB for FE-FR.
- The proposed CPNR solution along with DSIC techniques are implemented on the WARP v3 IBFD radio SDR board integrated with a dual port slot coupled antenna. On this set up, total SI suppression performance is measured, while

a channel emulator modeling the IEEE 802.11 indoor channel is applied on the baseband samples for considering the effect of multi-path. It is shown that for low multi-path spread, applying CPNR enhances TE-FR, FE-TR and FE-FR techniques (by about 6 dB) and brings their performance close to that of TE-TR with CPNR. CPNR is shown to enhance the multi-path resiliency of DSIC techniques. For instance, for 150 ns rms delay spread, highest improvement with CPNR is obtained for FE-FR as 13 dB.

- The IBFD radio test bed is extended to include two IBFD radios and the quality of bidirectional IBFD communication between two radios is measured in terms of Error Vector Magnitude (EVM), considering DSIC techniques with and without CPNR and modeling different propagation delays between the nodes. The test results demonstrate that for frequency-domain DSIC, with CPNR, EVM can be improved by up to 5 percent, allowing asynchronous nodes with realistic propagation delays.

- DSIC technique FE-TR and CPNR are implemented on the FPGA of the WARP v3 SDR board. It is demonstrated that the test results for total SI suppression and EVM with the FPGA implementation are highly consistent with the earlier test results obtained on the SDR based IBFD radio, where the algorithms were executed on MATLAB.

- The complexity costs of all DSIC techniques with and without CPNR have been evaluated in terms of number of floating point operations. It is shown that, DSIC techniques FE-FR and TE-FR with CPNR require 20 percent lower complexity as compared to the time-domain DSIC with CPNR.

- A new switched radio architecture (IBFD-SW) along with non-linear estimation algorithms are proposed for solving the non-linear SI problem in OFDM based IBFD radios. On IBFD-SW radio architecture, non-linear estimation is performed prior to linear SI cancellation to produce a reference SI signal which involves the non-linear behavior, but none of linear channel effects.

- Two methods are proposed for non-linear estimation on the switched IBFD radio architecture: 1) Time-domain non-linear polar polynomial (NLP) method is proposed to estimate the magnitude and phase of the non-linear SI signal separately providing more accurate estimation as compared to complex estimation. 2) Neural network based non-linear frequency-domain (NLF) estimation method is proposed for estimating the effects of non-linearity per each OFDM subcarrier. This solution utilizes a richer feature space than the time-domain method(s), providing highest SI cancellation.

- IBFD-SW radio architecture is implemented together with proposed time and frequency domain non-linear estimation methods and linear SI cancellation techniques on WARP v3 SDR set-up [6]. Prominent non-linear SI cancellation solutions from the literature are also implemented on the same set-up. Total SI suppression performance is observed in the laboratory environment and with a channel emulator modeling multi-path.
  - With the proposed IBFD-SW radio architecture and non-linear estimation algorithms, up to 13 dB enhancement on the total SI suppression performance is recorded over existing digital non-linear SI cancellation schemes. For most of the transmit power levels, the SI signal power is suppressed to the noise floor of the system promising range extension for the earlier versions of our IBFD radio in [3], [5].
  - The performance of all considered non-linear cancellation solutions are evaluated in a multi-path environment for the first time in the literature. The proposed solution is proven to be robust against changes in multi-path, since non-linear estimation is isolated from the SI channel and learned model parameters and coefficients can be re-used in all environments. Meanwhile, the performance of existing digital non-linear SI cancellation schemes degrade with changes in the (multi-path) channel, as they require re-optimization of model parameters and re-calculation of the non-linear coefficients.
- Estimation overhead and complexity of the proposed non-linear algorithms are derived. It is shown that our algorithms have almost no overhead as compared to state-of-the-art integrated digital SI cancellation methods, while computational complexity is significantly reduced, by four to six orders of magnitude for estimation and one to two orders of magnitude for reconstruction.

1.2 Thesis Organization

The organization for the rest of this thesis is as follows: In Chapter 2, background on IBFD radios is presented followed with linear and non-linear SI cancellation schemes. In Chapter 3, the CP noise problem is analyzed in detail and CPNR solution is presented. Chapter 4 presents our proposed switched IBFD radio solution along with proposed time and frequency domain non-linear SI estimation approaches. Chapter 5 presents the conclusions of this dissertation as well as discusses on directions for future work. In the end, Appendix A contains description of the FPGA implementation of linear DSIC with CPNR. Appendix B gives the optimization of non-linear model parameters for switched IBFD radio, and Appendix C provides validation of results for IBFD radio.

2. DIGITAL SELF-INTERFERENCE CANCELLATION IN IN-BAND FULL-DUPLEX (IBFD) WIRELESS COMMUNICATION

A typical system architecture of an IBFD radio providing SI suppression at different stages is depicted in Fig. 2.1. Here, the SI signal generated from the transmitter's baseband block is distorted in a non-linear manner by PA and LNA and in a linear manner by the SI channel, until it arrives at the receiver's baseband chain. The power of SI signal is lowered by employing antenna(s) and/or RF components such as circulators followed by an analog cancellation circuitry. At the baseband, digital non-linear and linear SI cancellation are applied for further eliminating the SI signal.

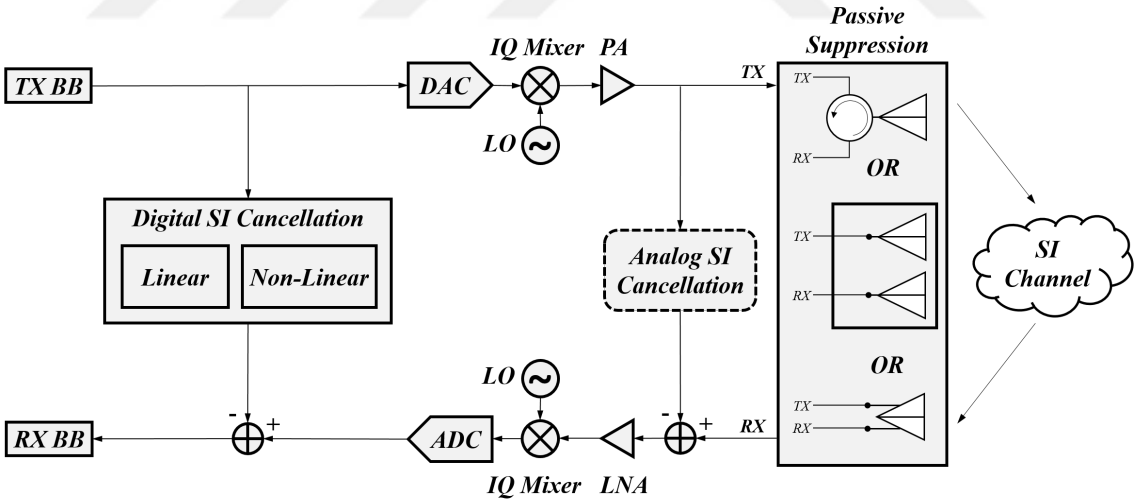

Figure 2.1 Stages in SI cancellation in IBFD radio

2.1 Self-Interference Cancellation in Full-Duplex Communication

In the first work on full-duplex communication at Sabanci University [1], a novel full-duplex, low-complexity radio design is presented which uses only a single patch antenna without a duplexer or circulator to passively suppress the self-interference and employs linear digital SI cancellation (DSIC) techniques at baseband to eliminate the remaining self-interference. The DSIC techniques used in the proposed full-duplex implementation are based on Least Squares (LS) time and frequency domain estimation (abbreviated as TE and FE, respectively) and time and frequency domain reconstruction approaches (abbreviated as TR and FR, respectively). The proposed full-duplex design has been tested for the IEEE 802.11g wireless standard using WARP v3 Software Defined Radio (SDR) as the implementation platform as shown in Fig. 2.2 and it is demonstrated that this design provides an overall suppression of 88 dB as depicted in Fig. 2.3.

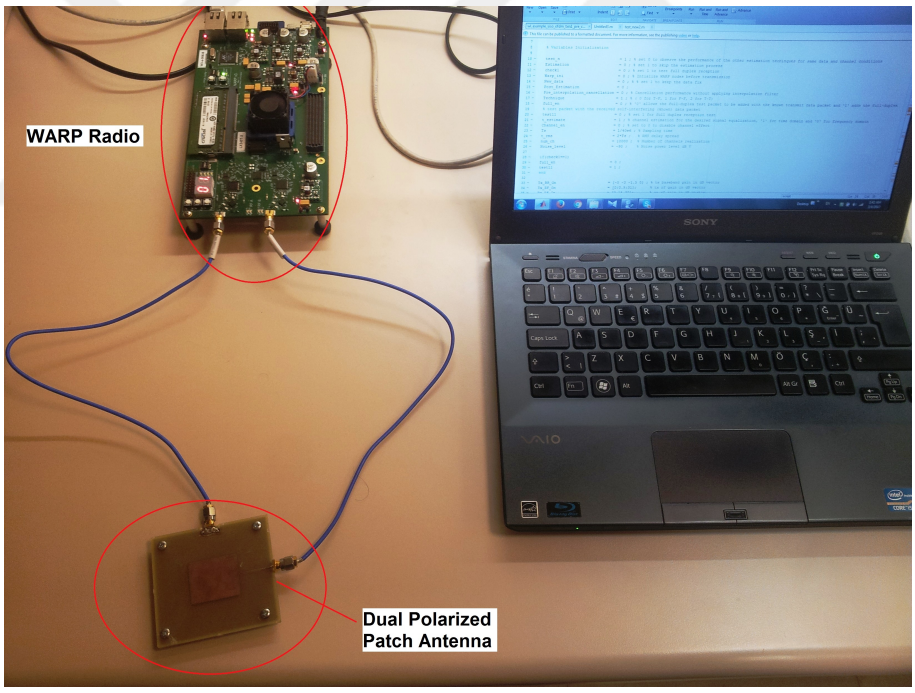

Figure 2.2 Experimental setup of full-duplex design in [1]

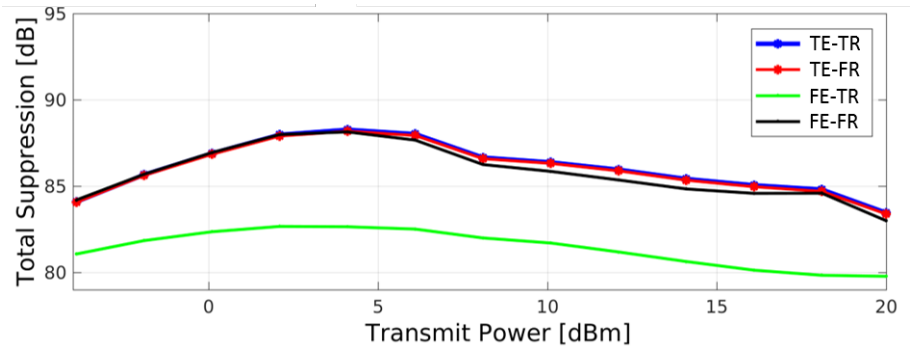

Figure 2.3 Performance of the proposed full-duplex design in [1] for different DSIC techniques

In our second work at Sabanci University [7], the performance of the low complex IBFD radio in [1] is enhanced by integrating the radio with two new antennas providing high passive suppression. Detailed laboratory tests are conducted to investigate the performance of the proposed IBFD radio architecture considering different indoor positions (in the open laboratory environment and in semi-absorbing system) and various orientations (horizontal, vertical, tilted) for each antenna as depicted in Fig. 2.4. In [7], it is shown that the monostatic IBFD architecture can achieve an overall total SI suppression of up to 99 dB in the semi-absorbing system, as it can be seen in Fig. 2.5.

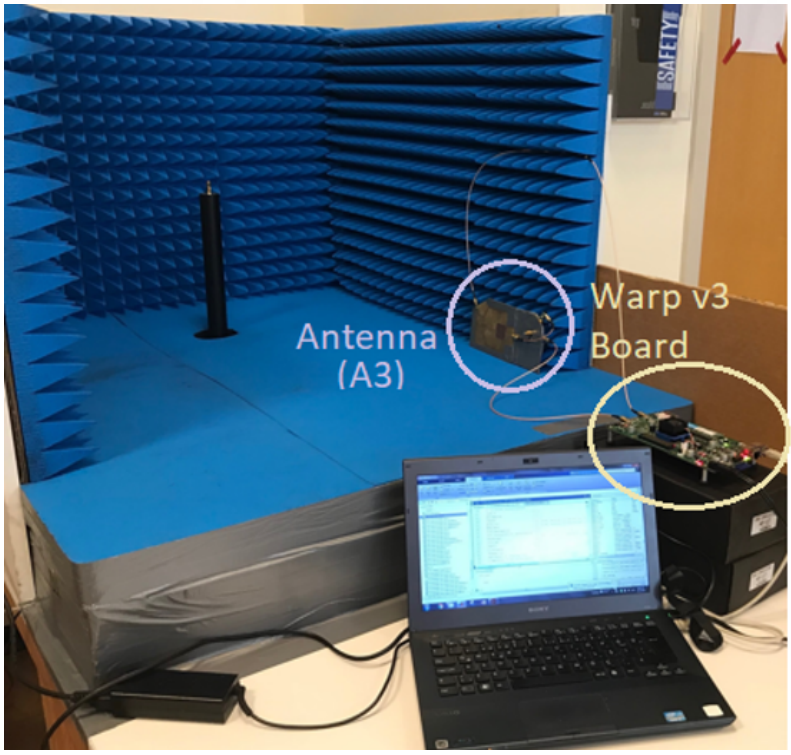

Figure 2.4 Test set-up in semi-absorbing system in [7]

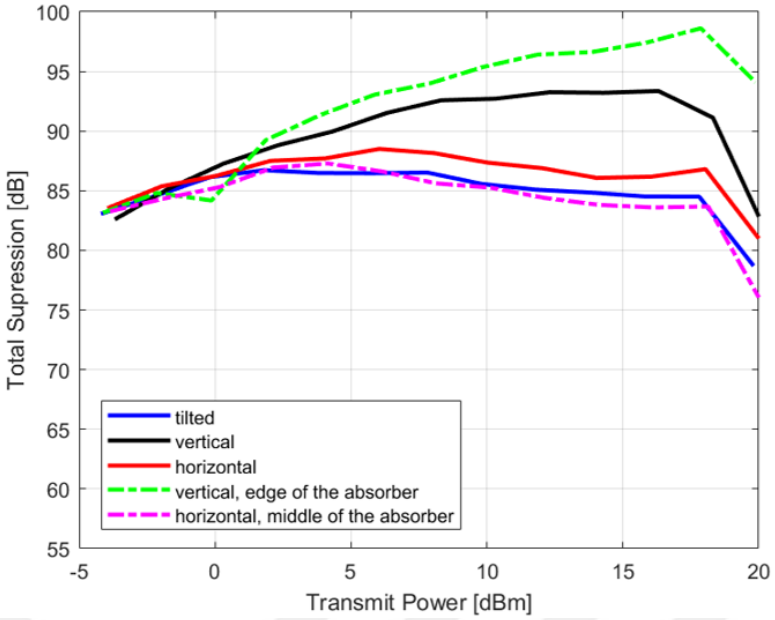

Figure 2.5 Performance of the IBFD radio for various antenna orientations in [7]

In [7], for realizing the bidirectional communication, we have established a test set-up as depicted in Fig. 2.6 (a), in which two WARP v3 boards are used as Node 1 and Node 2. To initiate the bidirectional communication, as seen in Fig. 2.6 (b), as a first step, Node 1 starts transmission for one preamble duration (T_p), while Node 2 stays silent. Then, Node 1 stops and waits for Node 2 to start the transmission. After completion of the preamble period of Node 2, the two nodes start sending the payload data at the same time for T_d duration to realize the FD communication. The mute periods are necessary for clean estimation of the SI channel at each node, so that there is no interference from the other node.

During FD communication, the received signal at the receiver of Node 1 is the sum of the SI signal from itself and the SoI arriving from Node 2, as it can be seen in the top plot in Fig. 3.12 (a). In the lower plot of Fig. 3.12 (a), the residual signal at Node 1 is depicted, where it can be observed that SI is cancelled perfectly for the training phase and the SoI arriving from Node 2 remains to be processed after performing the SI suppression. Symmetrically, the same operations take place in Node 2 to retrieve the data arriving from Node 1 [7].

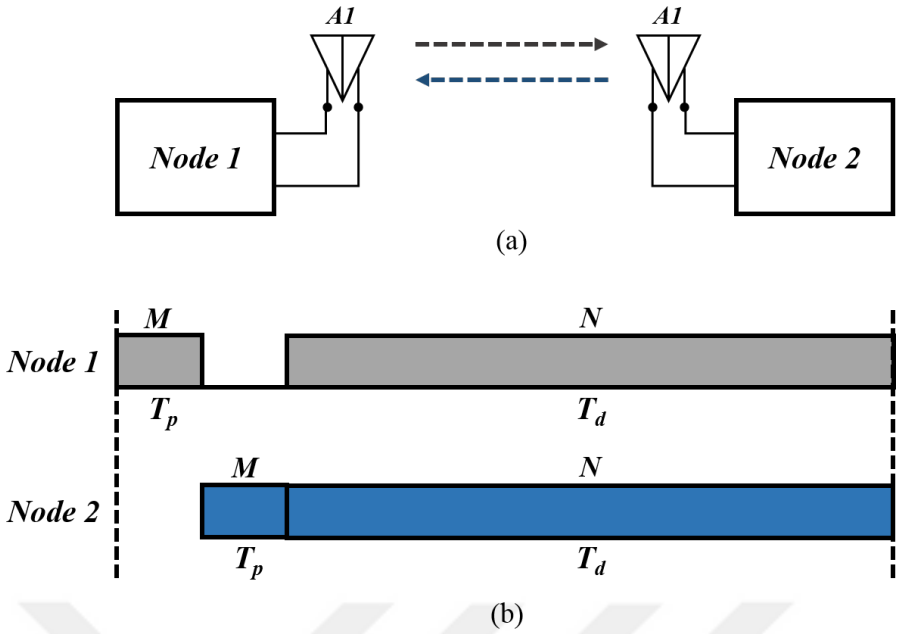

Figure 2.6 In [7] (a) Bidirectional FD communication (b) Timing of the transmit frames for Node 1 and Node 2

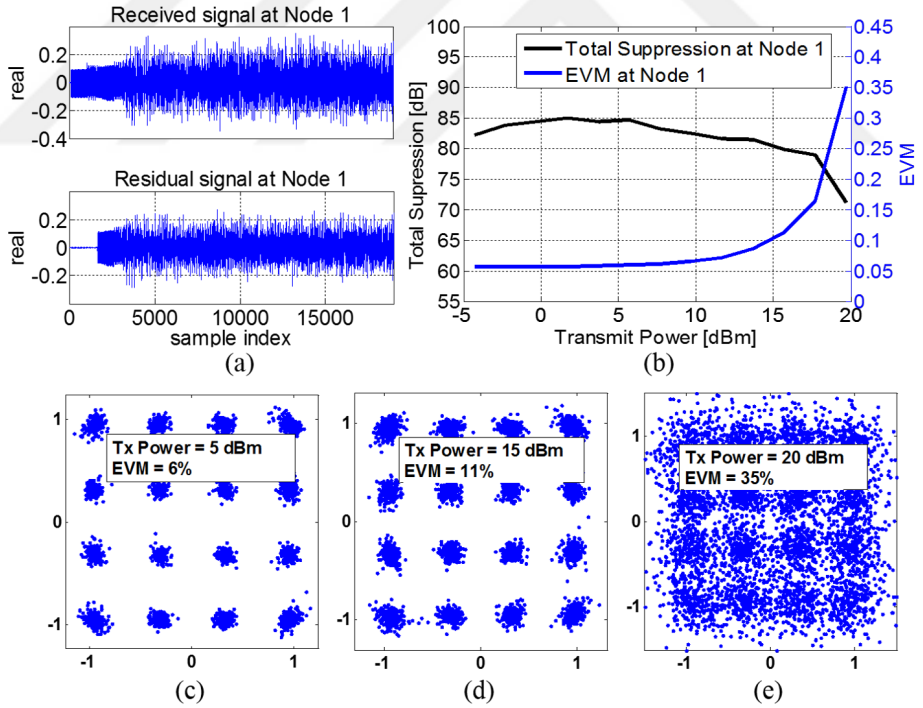

Figure 2.7 In [7] (a) Total received signal at Node 1 (top plot) and the residual signal at Node 1 after SI suppression (lower plot) (b) Total suppression at Node 1 along with the EVM values of SoI arriving from Node 2 (c) Constellation diagram of 16-QAM SoI at Node 1 for 5 dBm transmit power. EVM is 6% (d) Constellation diagram of 16-QAM SoI at Node 1 for 15 dBm transmit power. EVM is 11% (e) Constellation diagram of 16-QAM SoI at Node 1 for 20 dBm transmit power. EVM is 35%

In this experiment, we have measured the EVM of the received SoI for 16-QAM modulation with respect to increasing transmit power at Node 1, while the transmit power of Node 2 remains fixed. In Fig. 3.12 (b), the EVM values at Node 1 are provided along with the total SI suppression results. In the figure, it is observed that EVM is growing while the total suppression is degrading as transmit power is increased. This effect can also be noticed in the constellation diagrams in Fig. 3.12 (c), (d), and (e), where the transmit power is set to 5, 15, and 20 dBm and the measured EVM is 6, 11 and 35%, respectively [7].

In addition to observing the EVM, we have also calculated the throughput of FD communication, considering the scheme in Fig. 2.6 (b) and we compare it with the throughput of HD communication. Observing Fig. 2.6 (b), the total throughput of the bidirectional channel between Node 1 and Node 2, considering FD and HD communication can be found as:

$$R_{FD} = \frac{2N.k_d}{2T_p + T_d} bps, \tag{2.1}$$

$$R_{HD} = \frac{N.k_d}{T_p + T_d} bps. \tag{2.2}$$

Here, N is the number of data symbols, k_d is the modulation order. Nodes are assumed to share the time equally in HD communication. The throughput gain of FD over HD is calculated as:

$$G_T = \frac{R_{FD}}{R_{HD}} = \frac{2(T_p + T_d)}{2T_p + T_d}. \tag{2.3}$$

In our set-up, $N = 56000$, $T_p = 38.4$ μs, $T_d = 2800$ μs, and $k_d = 4$ for 16-QAM. Therefore, the throughput values become $R_{FD} = 155.73$ Mbps, and $R_{HD} = 78.91$ Mbps, and the throughput gain of FD over HD is $G_T = 1.973$ which is close to theoretical maximum of 2 [7].

In [1] and [7], we have noted cyclic prefix (CP) noise problem in the residual SI signal obtained after linear DSIC techniques and the problem of performance degradation due to non-linearity at high transmit powers. In this thesis, we propose solutions in order to alleviate both problems. In the rest of this chapter, for IBFD radios, first we review different linear DSIC techniques with time-domain estimation (TE) or frequency-domain estimation (FE) followed with time-domain reconstruction (TR) or frequency-domain reconstruction (FR). Then, we present the related work in the literature for non-linear SI cancellation.

2.2 Linear Digital Self-Interference Cancellation

DSIC involves estimation of the SI channel and reconstruction of the SI signal, both are performed in frequency or time-domain [1]. Fig. 2.8 depicts the baseband level block diagram of the OFDM based IBFD system. Here, the received signal $\mathbf{y}$ is:

$$\mathbf{y} \;=\; \mathbf{x} * \mathbf{h} + \mathbf{r} + \mathbf{w}, \tag{2.4}$$

where $\mathbf{h}$ is the impulse response of the SI channel over the (known) transmitted samples $\mathbf{x}$. $\mathbf{r}$ is the SoI, and $\mathbf{w}$ is additive white Gaussian noise (AWGN). Here, * is the convolution operator.

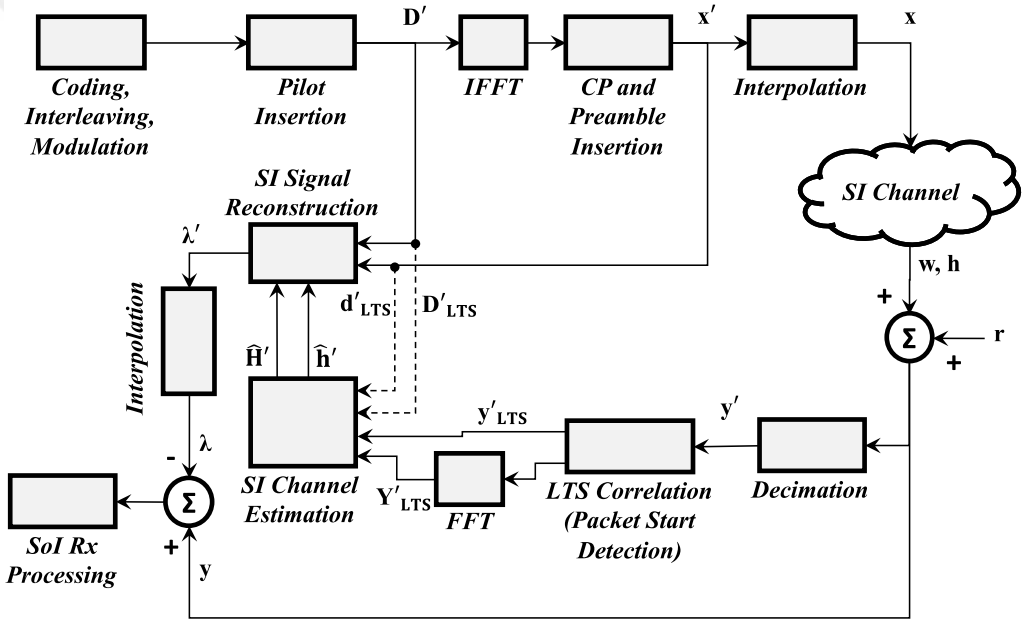

Figure 2.8 Baseband model of the OFDM based IBFD transceiver.

As shown in Fig. 2.8, first, the received signal is decimated and $\mathbf{y}'$ is obtained. Then, the starting point of the packet is determined by means of the long training sequence (LTS) correlation procedure. As soon as the packet start point is detected, the LTS symbols are extracted from the preamble part of $\mathbf{y}'$ and are averaged. The average of LTS symbols is utilized to estimate the SI channel as $\hat{\mathbf{H}}'$ in frequency-domain, or as $\mathbf{h}'$ in time-domain.

In [1], least squares (LS) algorithm is shown to provide best performance and lower complexity as compared to other alternatives for SI channel estimation. Therefore, in this thesis, we utilize the SI channel estimation algorithms based on the LS approach. In time-domain SI channel estimation (TE), the average of received LTS

symbols $\mathbf{y'_{LTS}}$ is represented by the convolution of transmitted known LTS symbol with the channel impulse response as in (2.4). It can be re-expressed as a matrix multiplication of $\mathbf{X'_{LTS}}$ with the SI channel impulse response $\mathbf{h'}$, formulated as follows [1]:

$$\mathbf{y'_{LTS}} \;=\; \mathbf{X'_{LTS}}.\mathbf{h'} + \mathbf{w'_{LTS}} \;,$$

$$\mathbf{X'_{LTS}} = \begin{bmatrix} d'_{LTS_{(1)}} & d'_{LTS_{(K)}} & d'_{LTS_{(K-1)}} & \cdots & d'_{LTS_{(K-K_{\mathrm{CP}}+2)}} \\ d'_{LTS_{(2)}} & d'_{LTS_{(1)}} & d'_{LTS_{(K)}} & \cdots & d'_{LTS_{(K-K_{\mathrm{CP}}+3)}} \\ \vdots & \vdots & \vdots & \ddots & \vdots \\ d'_{LTS_{(K-1)}} & d'_{LTS_{(K-2)}} & d'_{LTS_{(K-3)}} & \cdots & d'_{LTS_{(K-K_{\mathrm{CP}})}} \\ d'_{LTS_{(K)}} & d'_{LTS_{(K-1)}} & d'_{LTS_{(K-2)}} & \cdots & d'_{LTS_{(K-K_{\mathrm{CP}}+1)}} \end{bmatrix}, \quad \mathbf{h'} = \begin{bmatrix} h'_1 \\ h'_2 \\ \vdots \\ h'_{K_{\mathrm{CP}}-1} \\ h'_{K_{\mathrm{CP}}} \end{bmatrix}, \tag{2.5}$$

where $\mathbf{X'_{LTS}}$ is the KxK_{CP} Toeplitz matrix formed by the known transmitted LTS symbol $\mathbf{d'_{LTS}}$ which is circularly located in the rows and in the columns. Here, K is the size of fast Fourier transform (FFT) operation which is equal to the number of sub-carriers in the communication channel as well as the number of samples in time-domain in one OFDM symbol without CP. Hence, the size of $\mathbf{y'_{LTS}}$ and $\mathbf{w'_{LTS}}$ is Kx1. K_{CP} is the guard interval provided by the CP [29]. Therefore, the size of $\mathbf{h'}$ is K_{CP}x1. The time-domain SI channel estimate, $\mathbf{\hat{h}'_{TE}}$ (K_{CP}x1), is calculated by means of

$$\mathbf{\hat{h}'_{TE}} = \mathbf{X'^{\dagger}_{LTS}}.\mathbf{y'_{LTS}}. \tag{2.6}$$

Here, $\mathbf{X'^{\dagger}_{LTS}}$ is the Moore-Penrose inverse of $\mathbf{X'_{LTS}}$. Note that, the maximum length of the coefficients of the channel impulse response to be estimated in $\mathbf{\hat{h}'_{TE}}$ is restricted with the length of CP which is K_{CP}. The frequency-domain representation of $\mathbf{\hat{h}'_{TE}}$ in (2.6) is obtained from

$$\mathbf{\hat{H}'_{TE}} = \mathrm{FFT}\left\{\mathbf{\hat{h}'_{TE}}\right\}. \tag{2.7}$$

In frequency-domain SI channel estimation (FE), the average of received LTS symbols $\mathbf{y'_{LTS}}$ is converted into frequency-domain by applying FFT yielding $\mathbf{Y'_{LTS}}$ with the size of Kx1. Then, the SI channel estimate $\mathbf{\hat{H}'_{FE}}$ is computed by comparing $\mathbf{Y'_{LTS}}$ with the known transmitted LTS symbols $\mathbf{D'_{LTS}}$ assigned to K sub-carriers in frequency-domain [27]:

$$\hat{\mathbf{H}}'_{\mathbf{FE}} = \frac{\mathbf{Y}'_{\mathbf{LTS}}}{\mathbf{D}'_{\mathbf{LTS}}}, \tag{2.8}$$

where the size of $\hat{\mathbf{H}}'_{\mathbf{FE}}$ is Kx1. The time-domain representation of $\hat{\mathbf{H}}'_{\mathbf{FE}}$ in (2.8) is obtained by the inverse FFT (IFFT) operation:

$$\hat{\mathbf{h}}'_{\mathbf{FE}} = \mathrm{IFFT}\left\{\hat{\mathbf{H}}'_{\mathbf{FE}}\right\}. \tag{2.9}$$

Here, the size of $\hat{\mathbf{h}}'_{\mathbf{FE}}$ is again Kx1. Note that, with FE, the number of SI channel coefficients to be estimated is K. Since K_{CP} is less than K, the performance of FE surpasses the performance of TE in multi-path environments where the maximum excess delay is greater than K_{CP} as shown in performance results.

As it is seen in Fig. 2.8, the reconstruction stage employs the SI channel estimates and the known transmitted signals to realize a copy of the SI signal. In time-domain SI reconstruction (TR), the transmitted samples, $\mathbf{x}'$, are convolved with the channel impulse response estimates, $\hat{\mathbf{h}}'$, in order to obtain the reconstructed SI signal, $\boldsymbol{\lambda}'$, with the expression

$$\boldsymbol{\lambda}' = \hat{\mathbf{h}}' * \mathbf{x}'. \tag{2.10}$$

Either $\hat{\mathbf{h}}'_{\mathbf{TE}}$ in (2.6) or $\hat{\mathbf{h}}'_{\mathbf{FE}}$ in (2.9) can be used in (2.10) (in TR) as $\hat{\mathbf{h}}'$.

In frequency-domain SI reconstruction (FR), $\boldsymbol{\lambda}'$ is obtained by multiplying the channel estimate $\hat{\mathbf{H}}'$ in frequency-domain with the known symbols $\mathbf{D}'$ followed by the IFFT operation:

$$\boldsymbol{\lambda}' = \mathrm{IFFT}\{\mathbf{D}' \cdot \hat{\mathbf{H}}'\}. \tag{2.11}$$

$\hat{\mathbf{H}}'_{\mathbf{TE}}$ in (2.7) or $\hat{\mathbf{H}}'_{\mathbf{FE}}$ in (2.8) can be used in (2.11) (in FR) as $\hat{\mathbf{H}}'$. CP insertion and preamble attachment processes are applied after obtaining $\boldsymbol{\lambda}'$ [1].

Interpolation process is applied to $\boldsymbol{\lambda}'$ as the last step of reconstruction for obtaining $\boldsymbol{\lambda}$ to be subtracted from the received signal $\mathbf{y}$ as it is seen in Fig. 2.8. After performing subtraction, the remaining signal to be processed as SoI is:

$$\mathbf{y} - \boldsymbol{\lambda} = \mathbf{r} + \mathbf{w} + \mathbf{x}^{res}, \tag{2.12}$$

where, $\mathbf{x}^{res}$ represents the residual SI signal, which appears as additional noise on top of $\mathbf{r}$, which is subject to regular receive processing as in the IEEE 802.11g OFDM system [29]. In the rest of this section, $\mathbf{r}$ in (2.12) is set to zero for concentrating on DSIC.

In this thesis, we consider and we evaluate the four DSIC techniques obtained from the combinations of SI channel estimation and SI signal reconstruction algorithms, namely TE-TR, TE-FR, FE-TR, and FE-FR. In [1] and [7], on our SDR based IBFD set-ups, the residual signal x^{res} in (2.12) contains periodic signals at comparatively high levels in the transition regions from the end of an OFDM data symbol to the CP of the next symbol, especially when frequency-domain processing is involved after subtraction, as shown in Fig. 2.9. In this thesis, we name this problem as CP noise, and we investigate its origination at different SI channel estimation as well as SI signal reconstruction stages and how it affects IBFD communication, as presented in Chapter 3.

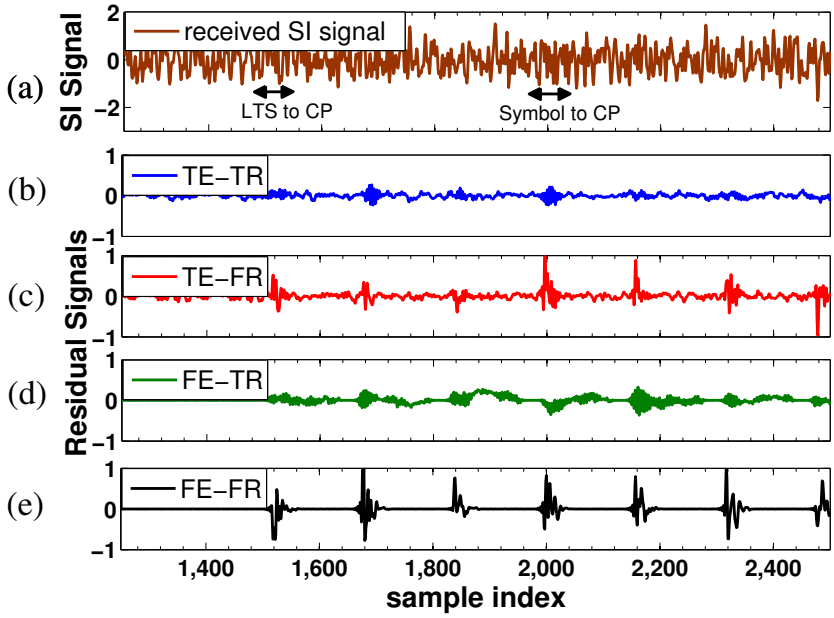

Figure 2.9 CP noise for different DSIC techniques observed from our simulations (in-phase) (a) Received SI signal (b) Residual signal for TE-TR (c) Residual signal for TE-FR (d) Residual signal for FE-TR (e) Residual signal for FE-FR

2.3 Non-Linear Self-Interference Cancellation

In the typical system architecture of an IBFD radio depicted in Fig. 2.1, the SI signal generated from the transmitter's baseband block is distorted in a non-linear manner by PA and LNA and in a linear manner by the SI channel, until it arrives at the receiver's baseband chain. Especially, at high transmit power levels, the amount of SI cancellation drops significantly due to the non-linear behavior of the power amplifiers (PA) on the transmit chain and low noise amplifiers (LNA) on the receive chain.

For non-linear SI signal modeling, memory polynomial (MP) model has been extensively used in the literature [36], [40], [41]. The MP model can be expressed in its conventional form as [42]:

$$x_{\text{NL}}[n] \;=\; \sum_{i=1,odd}^{P} \sum_{j=0}^{M} c_{i,j} x[n-j]\,|x[n-j]|^{i-1}\,, \tag{2.13}$$

where $c_{i,j}$ is the complex coefficient, $x[n]$ and $x_{\text{NL}}[n]$ are the complex, time-domain baseband equivalents of the RF input and output of the non-linear model, respectively at time instant n. P is the non-linearity order (i.e. degree of the polynomial) and M is the memory length. Since the even order terms generate distortion components outside the signal band, only the terms for odd orders are kept in (2.13) [4].

Considering the channel environment surrounding the radio, modeling the non-linear effects is not straightforward, since it requires the SI channel to be estimated beforehand. In the IBFD radio in [20], SI channel estimation and cancellation are performed at the RF level with a multi-tap analog canceller. Then, at the baseband level, SI cancellation is achieved by a non-linear digital SI canceller employing standard complex form of MP model. The system is integrated with a single passive antenna and a circulator shared by the transmitter and the receiver. In the OFDM based IBFD radio in [4], non-linear and linear effects are estimated together again with the MP model at the baseband level, but estimation is performed at eight times higher sampling rate (which requires significant hardware modification) to provide training via the Long Training Sequence (LTS) in the OFDM packet preamble. Furthermore, analog cancellation is also employed.

In [18], the authors have proposed an iterative technique in order to jointly estimate the linear SI channel and the non-linear coefficients via MP model. This work presents only simulation results still to be verified on a real environment. As the

system model, the authors consider a transmitter and a receiver separated with two antennas and analog circuitry for suppressing the SI signal. Also, in [37], orthogonalized least mean squares (OLMS) is proposed and in [38] recursive least squares is applied to reduce the computational complexity of the non-linear MP model, while providing similar performance. In both solutions, active analog cancellation is also employed.

Recently, neural networks (NN) have been considered for modelling non-linearity of wireless systems with reduced computational complexity [39], [43], [44], [45], [46]. In [43], a real-valued feed-forward NN (RV-FFNN) based SI canceller is proposed, and in [44], the hardware implementation of this canceler is presented. In [39], complex-valued FFNN (CV-FFNN) is proposed to perform the SI cancellation demonstrating that the CV-FFNN achieves the same cancellation as the RV-FFNN although it has lower computational cost. In [45], a digital cancellation method based on recurrent NN is employed to eliminate both linear and non-linear parts of the SI signal. Also, a model based NN solution is proposed in [46]. The NN based solutions reduce the complexity of the MP model, but they cannot exceed its performance. Furthermore, in [44] and [45], analog cancellation is again employed.

In contrast to the above IBFD radio designs that need extra hardware for analog cancellation or require hardware modification, in [5] integrated linear and non-linear SI cancellation framework has been proposed along with passive suppression (via a dual port patch microstrip antenna) as a digital solution, without a hardware change. In the nested and residual integrated approaches in this framework, MP and Support Vector Regression (SVR) are employed as batch techniques for non-linear estimation, in addition to a proposed residual online algorithm, named as Orthonormalized LMS (ONLMS). In the nested approach, linear SI channel effects are first removed by inverse filtering the received SI signal; then, the inverse filter output is utilized by non-linear estimation/cancellation. Meanwhile, in the residual approach, non-linear cancellation is performed over the residual signal after linear cancellation [5]. All proposed schemes in the integrated framework as well as existing linear and non-linear cancellation methods are implemented on an OFDM based IBFD radio set-up and it is shown that the highest total SI suppression is achieved by the integrated residual MP scheme at moderate power levels and the integrated nested scheme with SVR provides the highest suppression at high transmit power levels. The residual online ONLMS outperforms non-linear only OLMS [37], performing close to nested MP, which has the lowest computational complexity among integrated schemes [5].

The drawback of all abovementioned digital non-linear SI cancellation solutions is that non-linear estimation is executed on the SI signal that has passed through

the linear channel. At high transmit power levels, the estimation of the linear SI channel becomes faulty, which in turn affects and degrades non-linear SI cancellation. Furthermore, if there is a change in the multi-path environment, the non-linear model needs to be updated accordingly and the coefficients need to be re-estimated for the new channel. This can cause excessive estimation (training) overhead each time the radio changes its environment. Moreover, all are applied in time-domain. These problems can be overcome with the solution proposed in [2], which employs an extra (auxiliary) receive chain to provide a non-linear SI signal as a reference to linear cancellation. Our solution in this thesis aims to *estimate and generate* the reference non-linear SI signal for linear cancellation, without the cost of an extra receive chain, while providing close to highest SI cancellation.

3. CYCLIC PREFIX NOISE REDUCTION FOR DIGITAL SELF-INTERFERENCE CANCELLATION IN OFDM BASED IBFD SYSTEMS

Orthogonal frequency division multiplexing (OFDM) is the pertinent waveform for current and next generation wireless systems, whose spectral efficiency can be potentially doubled by in-band full-duplex (IBFD) communication. However, in OFDM based IBFD systems, digital self-interference cancellation (DSIC) employed at baseband does not provide sufficient cancellation in the cyclic prefix (CP) region. When the propagation delay between two communicating radios is non-zero, the CP noise affects the data region of the desired signal. In this chapter, we propose CP noise reduction (CPNR) technique for OFDM based IBFD radios. We have evaluated CPNR with time and frequency domain DSIC schemes via both simulations and MATLAB and FPGA implementations on our Software Defined Radio based IBFD radio. In the laboratory tests, the total suppression of the IBFD radio is improved by 6 dB by employing CPNR in frequency-domain DSIC and EVM for bidirectional communication is improved by up to 5%, allowing realistic propagation delays. In addition to improving the total suppression and EVM performance, CPNR is also shown to enhance the multi-path resiliency of DSIC techniques.

3.1 Cyclic Prefix Noise in IBFD Systems

In this section, we present how the CP noise is originated from SI channel estimation and from SI signal reconstruction and how it affects IBFD communication.

3.1.1 Issues in SI Channel Estimation

In OFDM systems, an OFDM symbol comprises of a large number of closely spaced continuous wave tones (sub-carriers) in the frequency-domain. In the considered system in this thesis, basic windowing is applied to each symbol in the form of square wave (rectangular pulse), which produces a frequency spectrum represented by a sinc function convolved with the sub-carriers. The duration of the window determines the position of the zero crossings in frequency-domain. The sub-carrier spacing is arranged such that the zero crossings in the spectrum of one sub-carrier corresponds to the peaks of the adjacent sub-carriers in order to establish orthogonality [30].

In order to explore the problem in SI channel estimation in DSIC for IBFD communication, we consider the physical layer packet structure of the considered OFDM system [29], as depicted in Fig. 3.1 (a). The OFDM packet structure starts with a preamble including repeated LTS symbols in time-domain. After the preamble, data symbols take place in the OFDM packet with their CP parts copied from the end of each data symbol and appended to the beginning. Before conversion to time-domain (i.e., IFFT operation), both data and LTS symbols are prepared in frequency-domain, allocated to the reserved sub-carriers, as depicted in Fig. 3.1 (b). Considering the window duration for data and LTS symbols as T seconds as shown in Fig. 3.1 (a), the zero-crossings for the sinc function, $\text{sinc}(\pi T f)$, are located at intervals of $1/T$ Hertz in frequency-domain, as depicted in Fig. 3.1 (b), ensuring the orthogonality. When CP is appended at the beginning of each data symbol, the duration of the data symbol is increased to a total duration of $T_{\text{tot}}{=}T{+}T_{\text{CP}}$ seconds, and the orthogonality of the sub-carriers is disturbed in the new sinc function, $\text{sinc}(\pi T_{\text{tot}} f)$, with zero-crossings at $1/T_{\text{tot}}$ Hertz, as depicted in Fig. 3.1 (c). The orthogonal and non-orthogonal sinc functions shown in Fig. 3.1 (b) and (c), respectively, can be expressed as:

$$\begin{aligned} \text{sinc}^{(k)}(f) &= \text{sinc}[\pi T(f - f_k)] \ , \\ \text{sinc}^{(k)}_{\text{tot}}(f) &= \text{sinc}[\pi T_{\text{tot}}(f - f_k)] \ , \end{aligned} \tag{3.1}$$

where f is the continuous frequency and f_k is the $(k)th$ sub-carrier ($k \in [1,\ K]$). Let us assume that the message symbol allocated on each sub-carrier is m_k ($k \in [1,\ K]$), which is a random complex number at the output of the modulator and it is zero ($m_k{=}0$) for K_{gsc} guard sub-carriers among total K sub-carriers and for DC sub-carrier. In the illustration in Fig. 3.1 (b) and (c), m_k is set as 1 for data sub-carriers. As seen in Fig. 3.1 (b), the frequency-domain representation of the transmitted data symbol without CP, $\mathbf{D'^t}$, is expressed as

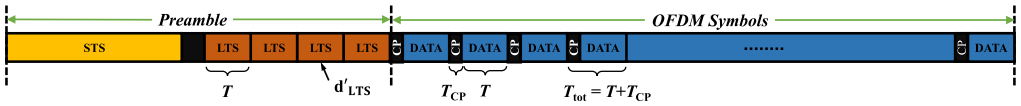

(a)

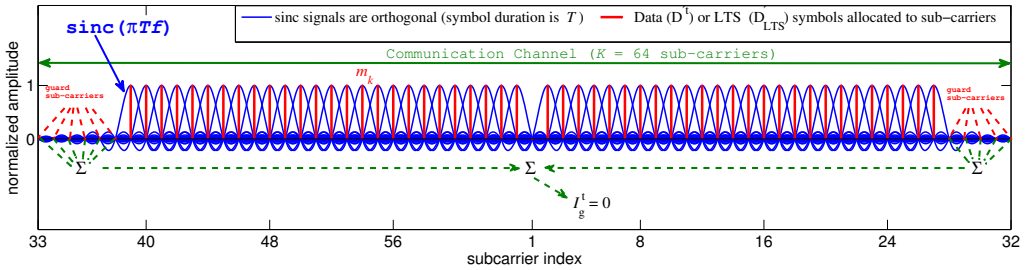

(b)

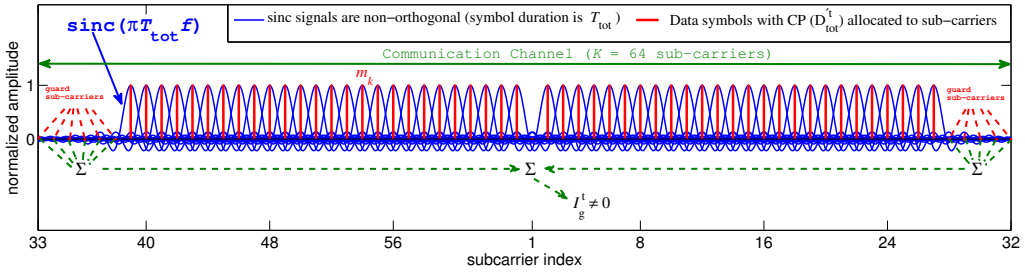

(c)

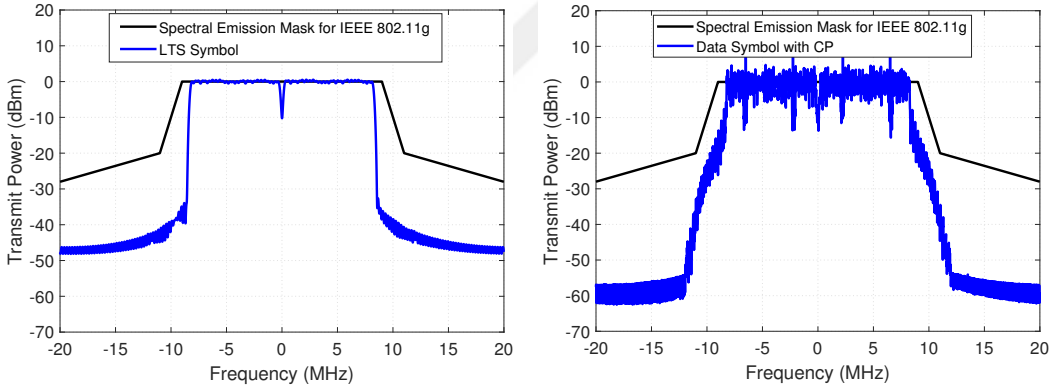

(d) (e)

Figure 3.1 (a) IEEE 802.11g physical layer OFDM packet structure (b) Orthogonalized sub-carriers in OFDM packet (c) Deterioration of orthogonality due to CP insertion resulting in non-zero values on the guard sub-carriers (d) Power spectral density of LTS symbol (e) Power spectral density of data symbol with CP

$$\mathbf{D'^t} = \sum_{i=1}^{K}\sum_{j=1}^{K} m_j.\mathrm{sinc}^{(j)}(f_i) = \sum_{i=1}^{K-K_{\mathrm{gsc}}} m_i + \underbrace{\sum_{i=K-K_{\mathrm{gsc}}+1}^{K_{\mathrm{gsc}}} m_i}_{I_{\mathrm{g}}^{\mathrm{t}}=0}, \tag{3.2}$$

where the second summation term, $I_{\mathrm{g}}^{\mathrm{t}}$ corresponds to the total amount of contribu-

tion from the guard sub-carriers. Since in $\mathbf{D'^t}$ sinc signals are orthogonal, m_i's are zero on the guard sub-carriers, hence $I_{\mathrm{g}}^{\mathrm{t}}$ is zero. This also holds true for LTS, and the power spectral density of the LTS symbol is as shown in Fig. 3.1 (d). Hence, the frequency-domain representation of LTS, $\mathbf{D'_{LTS}}$ can be expressed as:

$$\mathbf{D'_{LTS}} = \sum_{i=1}^{K}\sum_{j=1}^{K} m_j^{\mathrm{LTS}}.\mathrm{sinc}^{(j)}(f_i) = \sum_{i=1}^{K-K_{\mathrm{gsc}}} m_i^{\mathrm{LTS}} + \underbrace{\sum_{i=K-K_{\mathrm{gsc}}+1}^{K_{\mathrm{gsc}}} m_i^{\mathrm{LTS}}}_{I_{\mathrm{g}}^{\mathrm{t}}=0} . \tag{3.3}$$

However, $\mathbf{D'^t_{tot}}$, the frequency-domain representation of data symbol with CP is expressed as:

$$\mathbf{D'^t_{tot}} = \sum_{i=1}^{K}\sum_{j=1}^{K} m_j.\mathrm{sinc}_{\mathrm{tot}}^{(j)}(f_i) = \sum_{i=1}^{K-K_{\mathrm{gsc}}}\sum_{j=1}^{K} m_j.\mathrm{sinc}_{\mathrm{tot}}^{(j)}(f_i) + \underbrace{\sum_{i=K-K_{\mathrm{gsc}}+1}^{K_{\mathrm{gsc}}}\sum_{j=1}^{K} m_j.\mathrm{sinc}_{\mathrm{tot}}^{(j)}(f_i)}_{I_{\mathrm{g}}^{\mathrm{t}}\neq 0} , \tag{3.4}$$

where $I_{\mathrm{g}}^{\mathrm{t}}$ is not equal to zero as sinc signals are no longer orthogonal, as depicted in Fig. 3.1 (c). This results in growing side lobes in the spectrum of the transmitted data symbol with CP, as shown in Fig. 3.1 (e). After passing through the SI channel, the received data symbol in frequency-domain, $\mathbf{D'^r_{tot}}$, is represented as

$$\mathbf{D'^r_{tot}} = \sum_{i=1}^{K} c_i \sum_{j=1}^{K} m_j.\mathrm{sinc}_{\mathrm{tot}}^{(j)}(f_i) = \sum_{i=1}^{K-K_{\mathrm{gsc}}} c_i \sum_{j=1}^{K} m_j.\mathrm{sinc}_{\mathrm{tot}}^{(j)}(f_i) + \underbrace{\sum_{i=K-K_{\mathrm{gsc}}+1}^{K_{\mathrm{gsc}}} c_i \sum_{j=1}^{K} m_j.\mathrm{sinc}_{\mathrm{tot}}^{(j)}(f_i)}_{I_{\mathrm{g}}^{\mathrm{r}}\neq 0} , \tag{3.5}$$

where c_i is the SI channel coefficient for each sub-carrier, i. The term, $I_{\mathrm{g}}^{\mathrm{r}}$ involves the high side lobes due to interference from the neighbor sub-carriers as well as the SI channel effects. For DSIC for IBFD communication, c_i's in $I_{\mathrm{g}}^{\mathrm{r}}$ should be estimated for accurate reconstruction of the SI signal. However, when $\mathbf{D'_{LTS}}$ in

(3.3) is utilized for SI channel estimation in frequency-domain estimation (FE), the channel coefficients inside the side lobes cannot be estimated (since $I_{\mathrm{g}}^{\mathrm{t}} = 0$ in (3.3)); hence they cannot be represented in the reconstructed SI signal. In time-domain estimation (TE), the time-domain version of $\mathbf{D}'_{\mathbf{LTS}}$ in (3.3) is utilized in order to estimate the SI channel impulse response, and hence the effect of the side lobes are again not reflected. In both cases, the reconstructed SI signal does not include the effect of the high side lobes in the frequency-domain, resulting in CP noise, which is spread on the entire residual SI signal in time-domain.[1]

3.1.2 Issues in SI Signal Reconstruction

In OFDM systems, due to multi-path channel, inter-symbol interference (ISI) occurs on a given data symbol, resulting in leakage from the previous symbol. In order to avoid ISI, sufficient amount of guard interval is applied between the data symbols via the CP field. In time-domain reconstruction (TR), the known transmitted CP appended data symbols are convolved[2] with the SI channel impulse response in order to reconstruct the SI signal. This way, ISI (i.e. leakage) between OFDM symbols is reconstructed properly in TE-TR and FE-TR techniques.

On the other hand, in frequency-domain reconstruction (FR), the SI signal is reconstructed by multiplying the channel coefficients with the known transmitted symbols in frequency-domain. This is followed by conversion into time-domain and appending of the end of the symbol to the beginning as CP, as proposed in [1], and shown in Fig. 3.2 (b). The obtained CP appended data symbols are combined to form the reconstructed SI signal, $\boldsymbol{\lambda}$, without representing the ISI (leakage) between the (OFDM) symbols. As a result, the reconstructed SI signal $\boldsymbol{\lambda}$, differs from the received SI signal in the CP region by $L_{\mathrm{FR}}^{\mathrm{err}}$. Therefore, CP noise (due to incomplete estimation as explained above) is further increased with $L_{\mathrm{FR}}^{\mathrm{err}}$ in the CP regions, when FR is applied, as shown in the residual SI signal in Fig. 3.2 (c).

[1] Growing of side lobes in the transmitted data symbol with CP (due to non-zero $I_{\mathrm{g}}^{\mathrm{t}}$) does not actually cause a problem in half-duplex communication. In a half-duplex receiver, the CP is removed from the data symbol; hence, orthogonality of the data sub-carriers is regained and the spectrum of data without CP is similar to the spectrum of LTS shown in Fig. 3.1 (d). Therefore, utilizing the c_i's obtained from LTS is sufficient for equalization of the data sub-carriers.

[2] Here, for convolution, combined FFT and overlap-and-add methods are applied, for faster operation with lower complexity as compared to direct convolution, as shown in [27], [1].

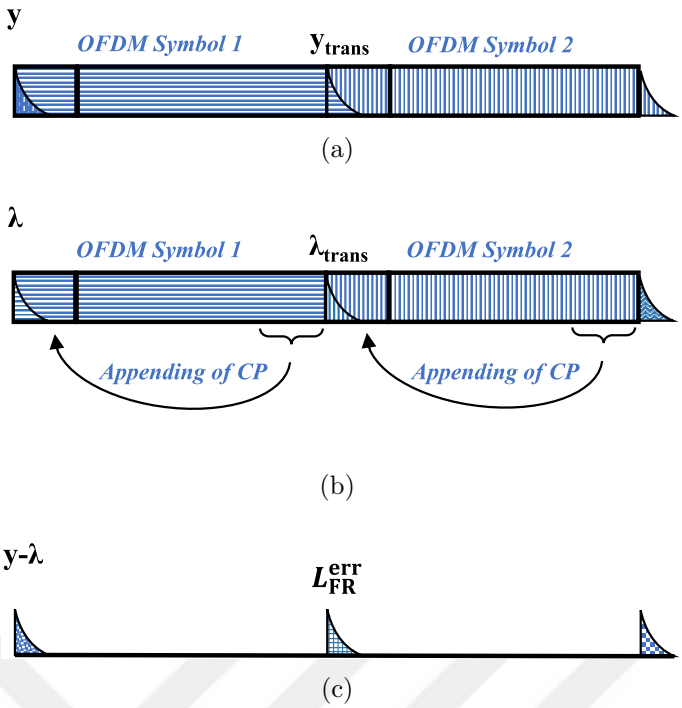

Figure 3.2 Illustration of the reconstruction issue in FR technique in [1] (a) received SI signal (b) reconstructed SI signal (c) residual SI signal

Fig. 2.9 illustrates the CP noise on the residual signal, as observed in our simulations for four DSIC techniques, TE-TR, TE-FR, FE-TR and FE-FR. Due to incomplete SI channel estimation, which ignores high side lobes in the spectrum of the transmitted (and SI) signal, CP noise is observed for both estimation techniques followed with TR, and it is spread on the entire residual SI signal, as depicted in Fig. 2.9 (b) and (d). CP noise is further increased due to $L_{\text{FR}}^{\text{err}}$ in the CP regions, when FR is employed after SI channel estimation, as shown in Fig. 2.9 (c) and (e).

3.1.3 Issues in Full-Duplex Communication

Now let us consider how CP noise can affect full duplex communication, by closely looking into a bidirectional IBFD communication scenario as shown in Fig. 3.3 (a). We assume the physical layer access scheme proposed in [7], depicted in Fig. 3.3 (b), where first, each node alone sends a packet preamble for estimating their own SI channel, while the other node estimates the communication channel for SoI. After the preambles, full duplex communication takes place, so that each node transmits its data, while receiving the other node's data (SoI) in the presence of residual SI from its own transmission. When SoI and the SI signals are perfectly synchronized

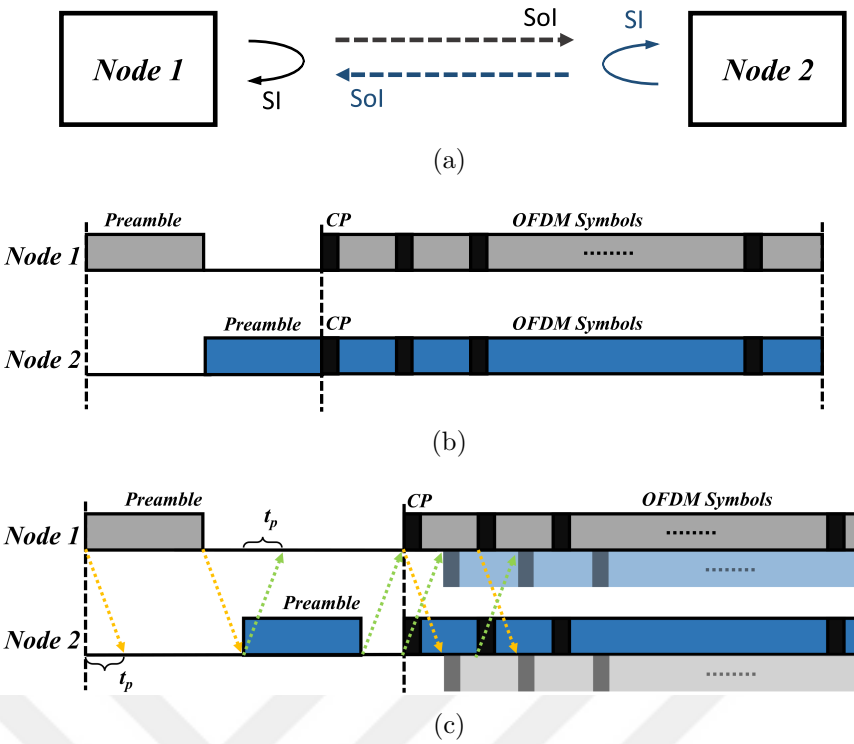

Figure 3.3 (a) Bidirectional IBFD communication scheme (b) Packets at Node 1 and Node 2 are synchronized (c) Packets at Node 1 and Node 2 are misaligned due to propagation delay (t_{p}).

as shown in Fig. 3.3 (b), the CP regions and data regions of SoI and SI signals overlap, so that the CP noise on the SI signal coincides with the CP region of the SoI. As the data region of the SoI observes small residual SI and CP region is to be discarded, decoding of SoI is not affected by CP noise. On the other hand, when the SoI and the SI signals are not synchronized as depicted in Fig. 3.3 (c), which can happen naturally due to propagation delay (t_{p}) between the nodes, the CP noise on the residual SI signal appears as additional significant amount of noise on data region of the SoI, degrading the reception quality.

3.2 Cyclic Prefix Noise Reduction (CPNR) Solution

Our proposed CP noise reduction (CPNR) solution is composed of two steps: 1) Tone insertion and filtering during LTS duration on the transmit chain for enhanced SI channel estimation and 2) enhanced SI signal reconstruction on the receive chain, as described next [3], [47].

3.2.1 Enhanced SI Channel Estimation

In this section, for improved SI channel estimation, in LTS, we propose to make m_i^{LTS} non-zero corresponding to $I_{\mathrm{g}}^{\mathrm{t}}$ in (3.3) in order to imitate the interference as it is observed in the case of data symbols with CPs seen in (3.4). We call this method as tone insertion method. This way, in the FE technique, c_i's inside $I_{\mathrm{g}}^{\mathrm{r}}$ in (3.5) will be also covered in the SI channel estimate $\hat{\mathbf{H}}'_{\mathbf{FE}}$. Similarly, in the TE technique, $\mathbf{X}'_{\mathbf{LTS}}$ will contain high frequency effects; hence SI channel impulse response estimate $\mathbf{h}'$ obtained from $\mathbf{X}'_{\mathbf{LTS}}$ will cover $I_{\mathrm{g}}^{\mathrm{r}}$ in time-domain.

As an illustration, we can consider the LTS symbol used in IEEE 802.11g [29] standard depicted in Fig. 3.4 (a). There are 64 sub-carriers throughout the communication channel (K=64) including guard sub-carriers. In this figure, for the LTS symbol, 11 sub-carriers at the both sides of the channel are kept idle as guard sub-carriers. Furthermore, an interpolation filter is applied for image rejection created by up-sampling. This entire scheme is also utilized as it is for the data symbols. Fig. 3.4 (b) is an illustration for the employment of the aforementioned tone insertion approach on the guard sub-carriers of the existing LTS symbol.

Note that, there is a limit for inserting additional training tones to the guard sub-carriers, due to their images created by up-sampling appearing inside the existing interpolation filter. Furthermore, the interpolation filter must be flat over the added tones. Therefore, when we insert training tones to all the guard sub-carriers sub-carriers, an ideal sharp filter is required for suppressing the out-band image tones, which is hard to implement practically. Consequently, we only insert the tones to 8 guard sub-carriers out of 11 guard sub-carriers and as a second phase, we enhance the filter such that it becomes flat over inserted tones to have a proper coefficient estimation for these tones, but suppresses the image created by up-sampling and sharp enough not to exceed the bandwidth, as shown in Figure 3.4 (b). Note that, tone insertion takes place during only the LTS symbol period and within K=64 sub-carriers (within T duration and within communication channel bandwidth); so, it influences neither the bandwidth nor the throughput of the IBFD communication as it can be seen in Fig. 3.4 (c).

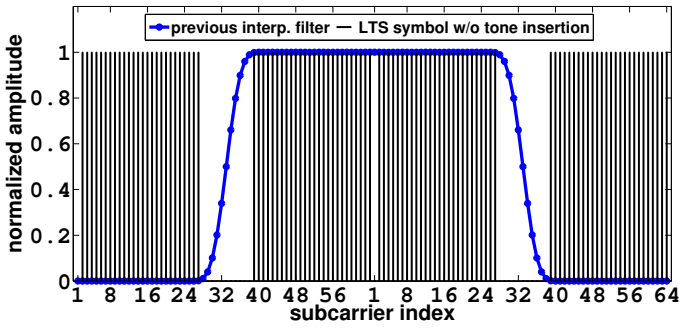

(a)

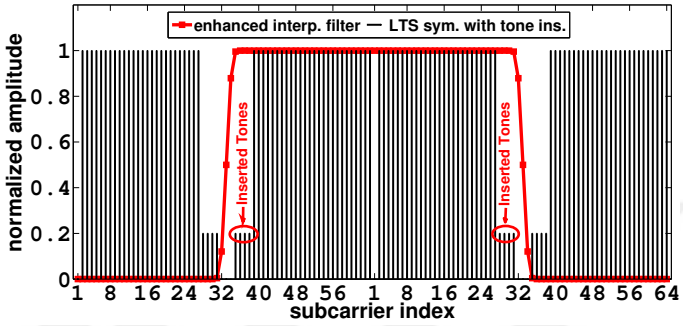

(b)

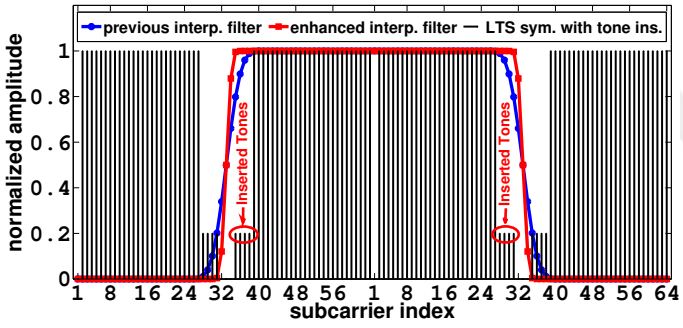

(c)

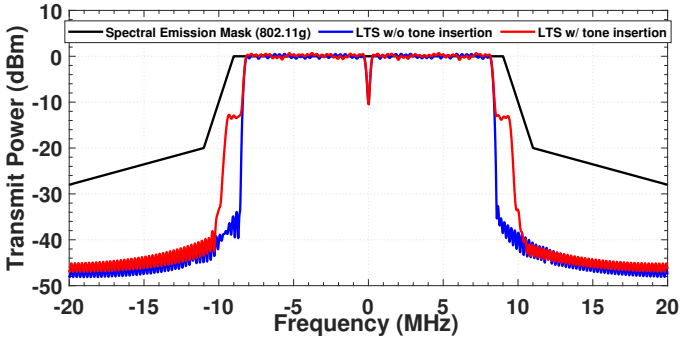

(d)

Figure 3.4 Frequency-domain representation of (a) LTS symbol up-sampled by 2 with the previously existing interpolation filter (b) the proposed tone inserted LTS symbol with the enhanced sharper interpolation filter (c) the proposed tone inserted LTS symbol along with previously existing and enhanced sharper interpolation filters. (d) Power spectral density of LTS w/ and w/o tone insertion along with the spectral mask of IEEE 802.11g.

In Fig. 3.4 (d), we compare the transmit power of the tone inserted LTS symbol with the spectral emission mask of IEEE 802.11g and we see that the emitted power is below the limits defined by the mask. Therefore, we conclude that LTS with tone insertion safely satisfies the spectral emission mask. Also the proposed filter still prevents the inter-symbol interference (ISI) in time-domain. Increasing the band-limited factor (β) of the filter which defines the broadening of the Nyquist frequency over an ideal filter yields the flatness over the inserted tones and provides suppression of the images. The aforementioned enhancements are labeled and implemented as CPNR-1 in the IBFD radio architecture as shown in Fig. 3.8.

3.2.2 Enhanced Frequency-Domain SI Signal Reconstruction

In order to represent the leakage induced by multi-path effect, we propose reconstructing the CP region of the given data symbol together with the previous OFDM symbol as shown in Fig. 3.5, rather than directly extracting and appending it in the current data symbol as in Fig. 3.2 (b) [1]. For reconstruction, we propose to apply the following steps: First, we extract the CP and the previous symbol from the known transmit signal, $\mathbf{x}'$, as follows:

$$\mathbf{x}'_{\mathbf{trans},i} \;=\; \bigsqcup_{n=PS-(K-K_{\mathrm{CP}})+(i-1)K_{\mathrm{SYM}}}^{PS+K_{\mathrm{CP}}+(i-1)K_{\mathrm{SYM}}} \mathbf{x}'(n)\;, \tag{3.6}$$

where $\mathbf{x}'_{\mathbf{trans},i}$ contains the *(i)th* CP of the *(i)th* OFDM symbol at the end along with the last part of the *(i-1)th* OFDM symbol at the beginning. PS is the packet start index indicating the starting point of the payload part. K_{CP} is the number of CP samples extracted from the last part of the OFDM symbol. K_{SYM} is the number of samples in the total OFDM symbol, $K_{\mathrm{SYM}} = K + K_{\mathrm{CP}}$. The disjoint union (concatenation) of the samples is obtained by $\bigsqcup$ operator to construct a vector.

The frequency-domain representation of the transition region, $\mathbf{X}'_{\mathbf{trans},i}$ is obtained by taking the K-point FFT of $\mathbf{x}'_{\mathbf{trans},i}$. Then, FR is employed to reconstruct the transition region ($\boldsymbol{\lambda}'_{\mathbf{trans},i}$):

$$\boldsymbol{\lambda}'_{\mathbf{trans},i} \;=\; \mathrm{IFFT}\{\boldsymbol{\Lambda}'_{\mathbf{trans},i} = \mathbf{X}'_{\mathbf{trans},i} \cdot \hat{\mathbf{H}}\}\;. \tag{3.7}$$

As the next step, the reconstructed CP samples, $\boldsymbol{\lambda}'_{\mathbf{CP},i}$, are extracted from the last

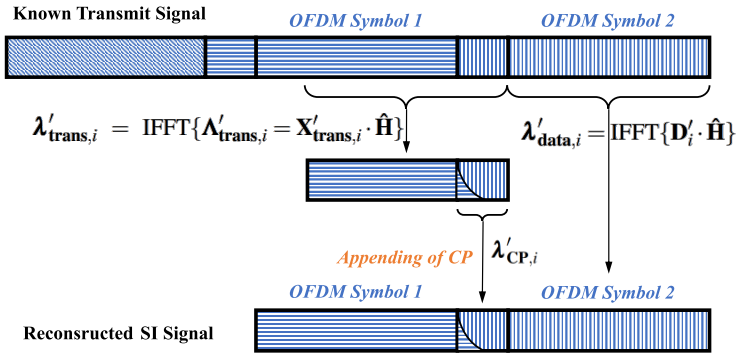

Figure 3.5 Reconstruction of CP region together with the previous OFDM symbol

K_{CP} samples of $\boldsymbol{\lambda}'_{\mathbf{trans},i}$ obtained from (3.7). The reconstruction of the payload symbol, $\boldsymbol{\lambda}'_{\mathbf{data}}$, is obtained from FR by utilizing the known payload symbol $\mathbf{D}'$. Then, the reconstructed CP and the reconstructed payload are concatenated back to back to obtain $\boldsymbol{\lambda}'_i$:

$$\boldsymbol{\lambda}'_{\mathbf{CP},i} = \bigsqcup_{n=K-K_{\text{CP}}+1}^{K} \boldsymbol{\lambda}'_{\mathbf{trans},i}(n) \ , \quad \boldsymbol{\lambda}'_{\mathbf{data},i} = \text{IFFT}\{\mathbf{D}'_i \cdot \hat{\mathbf{H}}\} \ , \tag{3.8}$$

$$\boldsymbol{\lambda}'_i \ = \ \boldsymbol{\lambda}'_{\mathbf{CP},i} \ +\!\!+ \ \boldsymbol{\lambda}'_{\mathbf{data},i} \ . \tag{3.9}$$

Here, $+\!\!+$ operator concatenates two vectors. Finally, whole reconstructed OFDM packet is:

$$\boldsymbol{\lambda}' = \bigsqcup_{i=1}^{N_{\text{STS}}} \boldsymbol{\lambda}'_{\mathbf{STS},i} +\!\!+ \boldsymbol{\lambda}'_{\mathbf{LCP}} +\!\!+ \bigsqcup_{i=1}^{N_{\text{LTS}}} \boldsymbol{\lambda}'_{\mathbf{LTS},i} +\!\!+ \bigsqcup_{i=1}^{N} \boldsymbol{\lambda}'_i . \tag{3.10}$$

In (3.10), the short training symbols (STS) to CP of LTS transition are corrected once following the same steps as in (3.6), (3.7), and (3.8), successively, and hence $\boldsymbol{\lambda}'_{\mathbf{LCP}}$ is obtained. N_{STS} is the number of STS symbols, N_{LTS} is the number of LTS symbols, and N is the number of payload symbols. Then $\boldsymbol{\lambda}'$ is interpolated and $\boldsymbol{\lambda}$ is obtained to be subtracted from the received signal.

3.3 Performance Simulations

In order to evaluate the performance of the proposed CPNR solution, we have first performed detailed simulations to observe digital cancellation in MATLAB environment, implementing CPNR with different DSIC techniques in comparison to the results of DSIC techniques without CPNR, considering AWGN, multi-path and time varying channel models for the SI channel.

3.3.1 Channel Model

The multi-path channel can be characterized as a tapped-delay-line (TDL) channel model presented in [48]. Assuming that the delay, τ_p, and the number of discrete multi-paths, $P_{\max}$, are time-invariant, the simplified low pass impulse response of the multi-path channel in TDL model is expressed as:

$$h(t) = \sum_{p=0}^{P_{\max}-1} \alpha_p(t)\delta(t-\tau_p), \tag{3.11}$$

where $\alpha_p(t)$ is the complex channel coefficients including both amplitude and phase effects.

To model the SI channel, the TDL model in (3.11) is used in conjunction with the IEEE 802.11 indoor channel model in [49] for generating the power delay profile (PDP) for $\alpha_p(t)$. The channel power decreases exponentially with delayed taps as $A(p) = \frac{1}{\sigma_\tau}\exp^{-pT_{\rm s}/\sigma_\tau},\ p = 0,1,2,...,P_{\max}$, where σ_τ is the rms delay spread, and $T_{\rm s}$ is the sampling time. The maximum excess delay is set to 10 times the rms delay spread in [49], so the maximum number of paths is calculated by σ_τ and $T_{\rm s}$ as $P_{\max} = [10\sigma_\tau/T_{\rm s}]$. With the assumption that the power of the $(p)th$ channel tap for $\alpha_p(t)$ has a zero mean and a variance of $\sigma_p^2/2$ proposed in [49], it is also necessary to reflect the Doppler power spectrum over $\alpha_p(t)$ to model the time varying environment. The Doppler power spectrum for the fading characteristics of the indoor wireless channel is used as in [48]:

$$S(f) = \frac{1}{1+9\left(\frac{f}{f_{\rm d}}\right)^2},\ \rightarrow\ f_{\rm d} = \frac{\nu_0}{\lambda}\ ,\ \lambda = \frac{\rm c}{f_{\rm c}}. \tag{3.12}$$

In (3.12), f_c is the carrier frequency, f_d is the Doppler spread, ν_0 is the environmental speed, λ is the wavelength, and c is the speed of light.

3.3.2 Results

Simulations are performed on the system model based on IEEE 802.11g shown in Fig. 2.8 [29]. The parameters for the simulations are listed in Table 3.1. The presented performance results are the average of 100 simulation runs. For AWGN, the SI SNR value is varied from 0 dB to 60 dB. The baseband signal has 20 MHz bandwidth and it is up-sampled by 2 to obtain 40 MHz signal with a sampling period of $T_s = 25$ ns. σ_τ is varied between 0 and 150 ns. In the indoor environment the environmental speed ν_0 is around 1.2 km/h, corresponding to Doppler spread f_d of approximately 3 Hz [48]. However, in the simulations, f_d is varied from 0 Hz to 300 Hz.

Table 3.1 Simulation parameters

Number of OFDM symbols (N)	100
Number of LTS symbols (N_{LTS})	4
Number of STS symbols (N_{STS})	30
Number of sub-carriers (K)	64
Number of CP samples (K_{CP})	16
Number of OFDM samples (K_{SYM})	80
Sampling time (T_s)	25 ns
Roll-off factor (β)	0.93
Number of payload (or LTS) sub-carriers	48
Number of pilot sub-carriers	4
Number of guard sub-carriers	11
Number of DC sub-carrier	1
Number of inserted sub-carrier for CPNR	8
Modulation	16-QAM

In all the results presented in this section, the amount of digital cancellation is calculated as the ratio of the received SI signal power to the residual SI signal power, given in log scale. In Fig. 3.6, digital cancellation performance of all schemes is depicted as a function of SNR for a delay spread of $\sigma_\tau = 75$ ns. In these plots, we provide the performance of DSIC techniques, TE-TR, TE-FR, FE-TR and FE-FR with CPNR (indicated as proposed) and without CPNR for two cases: When digital cancellation is measured over the entire packet (indicated as actual) and when DSIC is measured only over the data region, excluding the CP region (indicated as ideal), as in [1]. In the ideal case considered in [1], CP region, hence CP noise, is totally

discarded, assuming perfect synchronization between nodes. However, in real life scenarios with non-zero propagation delay (t_p), nodes are not synchronized, so CP noise will appear in the data region of SoI as residual SI, corresponding to the actual case. For all DSIC schemes in Fig. 3.6, we can observe how much the CPNR solution can improve each technique without CPNR in the actual case and how much the performance of DSIC with CPNR solution can approach the performance of the earlier, ideal case, where the CP noise is discarded.

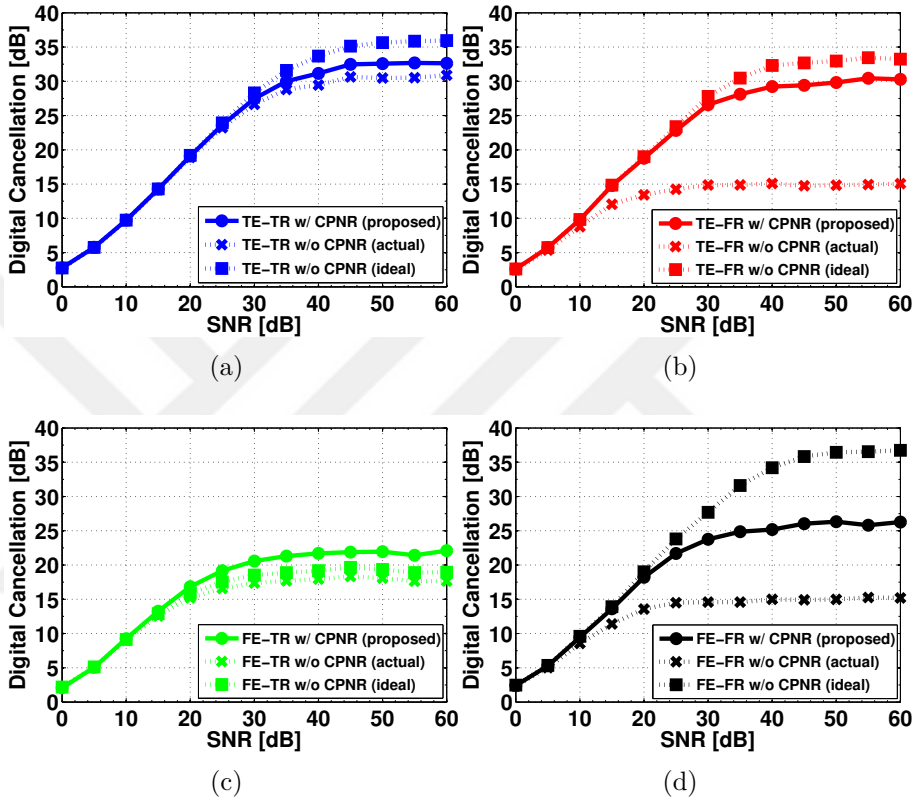

Figure 3.6 Digital cancellation performance after applying CPNR on DSIC techniques for IEEE 802.11 indoor channel with $\sigma_\tau = 75$ ns (a) TE-TR (b) TE-FR (c) FE-TR (d) FE-FR

Looking closely at Fig. 3.6 (a), it can be observed that CPNR can improve TE-TR without CPNR actual performance by only 0.5 dB at a selected SNR level of 25 dB and by up to 2-3 dB for high SNR levels, performing 3 dB below the ideal case. Fig. 3.6 (b) shows that CPNR can improve TE-FR actual performance by 8 dB at 25 dB, and by up to 15 dB at higher SNR levels, again performing about 3 dB below the ideal case. As shown in Fig. 3.6 (d), at 25 dB SNR, CPNR brings 7 dB higher cancellation to FE-FR in the actual case, promising up to 10 dB enhancement for high SNR, which is 10 dB below the ideal case. CPNR improves FE-TR actual case by 2.5 dB at 25 dB SNR and by up to 4 dB at higher SNR levels, while outperforming the ideal case. Note that, TE-TR and FE-TR techniques employ

only enhanced SI channel estimation via tone insertion, resulting in cancelling the remaining $I_{\mathrm{g}}^{\mathrm{r}}$ term. Meanwhile, the improvement by CPNR in TE-FR and FE-FR is obtained by applying both tone insertion and enhanced FR reconstruction steps on these DSIC techniques, so that $I_{\mathrm{g}}^{\mathrm{r}}$ and $L_{\mathrm{FR}}^{\mathrm{err}}$ are both eliminated. For FE-TR, enhanced SI cancellation via tone insertion also enhances the SI cancellation in the data region, resulting in higher digital cancellation than the ideal case.

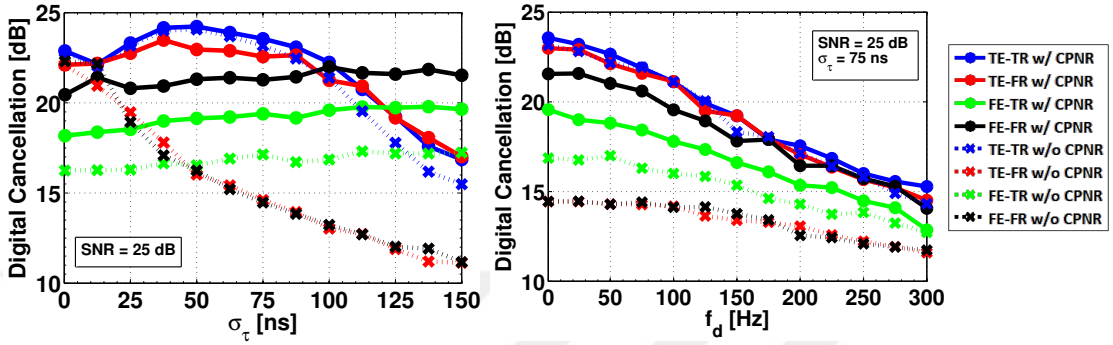

(a) (b)

Figure 3.7 Digital cancellation performance after applying CPNR on DSIC techniques for IEEE 802.11 indoor channel (a) varying delay spread (σ_τ), SNR = 25 dB (b) varying Doppler spread (f_d), SNR = 25 dB, σ_τ = 75 ns.

In Fig. 3.7 (a), SNR value is fixed as 25 dB and σ_τ is varied between 0 and 150 ns. Here, we observe that with CPNR, the cancellation performance is preserved for FE-FR and FE-TR techniques despite the delay spread is increased, while it degrades for TE-FR and TE-TR with CPNR after 100 ns. This is because, the number of coefficients in the SI channel impulse response, $\mathbf{h}'$ in (2.5) is restricted to the CP length (K_{CP}) in order to minimize the size of the Toeplitz matrix, $\mathbf{X}'_{\mathbf{LTS}}$, and hence to minimize the computational complexity. When the maximum excess delay of the channel becomes greater than K_{CP}, the performance of TE degrades. The number of coefficients of $\mathbf{h}'$ can be increased to enhance TE to reach the performance of FE, at the expense of increased complexity due to larger $\mathbf{X}'_{\mathbf{LTS}}$. Consequently, at σ_τ = 150 ns, it is observed that the performance of FE involved DSIC techniques with CPNR is around 6 dB over the performance of DSIC techniques with CPNR utilizing TE. Lastly, we have observed the behavior of DSIC techniques with and without CPNR, for a time varying channel, considering the channel model for a range of f_{d} values. Fig. 3.7 (b) depicts the degradation of DSIC performance for all the techniques, when Doppler spread (f_{d}) is increased. This degradation can be avoided if channel estimation can be renewed in accordance with f_{d}, which can be achieved by adjusting the packet size accordingly.

Note that, in the above simulation results, considering the digital cancellation perfor-

mance achieved by all DSIC techniques with CPNR, especially at high SNR levels, some degradation from TE-TR is observed in TE-FR, FE-FR and FE-TR techniques, as estimation and/or reconstruction domains are altered. This is because, during FFT/IFFT operations, the size of FFT/IFFT is taken as the length of the known transmit symbol (K=64) for lower complexity, as proposed in [27][3]. For high SNR values, the SI signal becomes much dominant over noise and the difference due to (smaller than ideal size) FFT conversion becomes noticeable. For low and moderate SNR levels, all DSIC schemes with CPNR perform closely, which is also the case in the SDR-based set-up, as shown in the test results next.

3.4 Performance Tests on SDR Based IBFD Radio

In the following, MATLAB and FPGA implementations of the CPNR solution in our IBFD radio on SDR platform are described and the experimental results are presented. We have considered WARP v3 SDR board, which supports IEEE 802.11g standard. WARPLab7 framework enables rapid physical layer prototyping by utilizing the WARP v3 hardware and MATLAB [50].

Fig. 3.8 shows the SDR implementation of our IBFD radio architecture, where two stages of SI suppression are employed. Passive suppression is achieved via the dual port slot coupled antenna [7]. As the second stage, DSIC techniques with CPNR (marked as the yellow colored blocks) are implemented on the WARP v3 board first via MATLAB and then on the FPGA.

[3]In [27], for TE-TR, for lowering complexity, convolution is applied via circular convolution with FFT processing and overlap-and-add operations, where the known transmit symbol (of size K=64) and SI channel impulse response (of size K_{CP}=16) are zero-padded in the end to reach the total FFT size (of K=80), producing the same result as direct convolution. Meanwhile, for all other techniques (TE-FR, FE-TR and FE-FR), FFT is taken at the size of the known transmit symbol (i.e., K=64) for lowering not only computational but also implementation complexity, so that the FFT units in the OFDM receiver can be re-used.

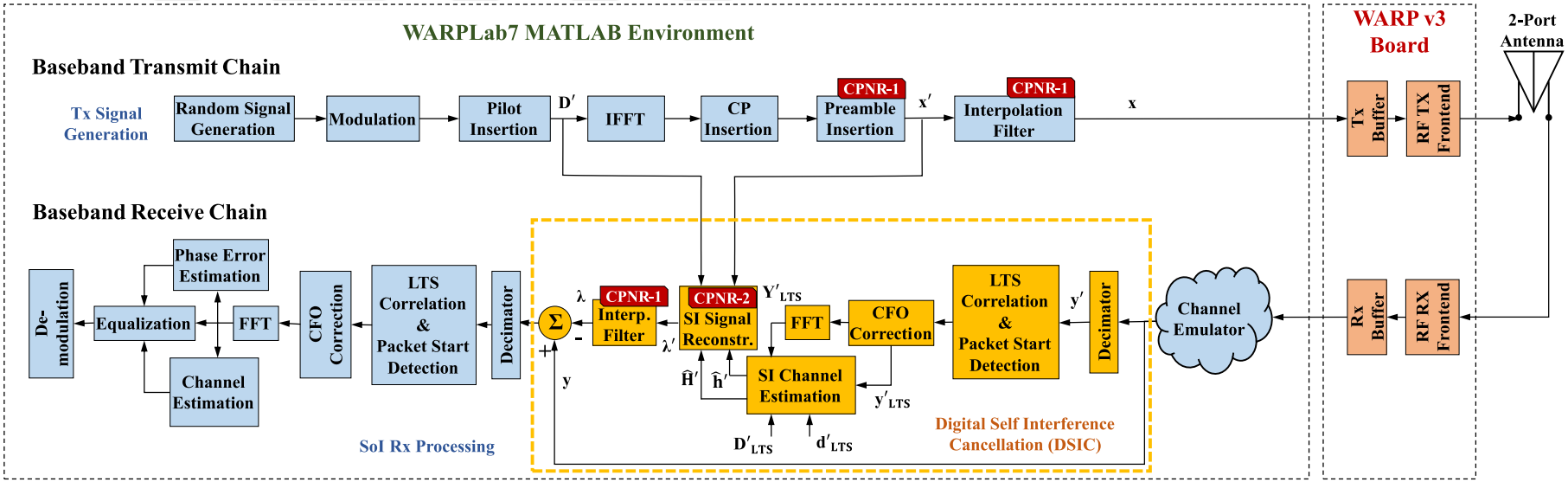

Figure 3.8 System model for DSIC with CPNR and the SDR based implementation for IBFD radio.

3.4.1 MATLAB Implementation and Tests

For MATLAB implementation, WARPLab7 framework enables an interface between the MATLAB environment running on a PC and WARP v3 hardware. This way, the transmit and receive waveforms are transferred between MATLAB environment and SDR board via Ethernet. For evaluating the performance of the techniques in the multi-path and time varying channel, we have utilized the model in Section 3.3.1 as the channel emulator applied on the baseband samples received from the WARP radio's receiving chain buffers as seen in Fig. 3.8.

We have pursued two sets of experiments in this section: In the first experiment we have considered a single IBFD radio and we have investigated the total SI suppression capability, considering DSIC techniques with and without CPNR, when SoI is absent. In the second set of experimments, we have evaluated bidirectional IBFD communication between two IBFD radios and we have investigated the reception performance, in terms of EVM of the SoI, considering synchronous and asynchronous scenarios for IBFD nodes. The parameters for all the experiments are the same as listed in Table 3.1. The test results for total SI suppression and EVM are discussed considering four DSIC techniques (TE-TR, TE-FR, FE-TR, FE-FR) with and without CPNR. All the test results are obtained by taking the average of 100 transmissions.

3.4.1.1 Total SI Suppression

In order to observe the total SI suppression performance on our single IBFD radio, tests are performed in the open laboratory environment, considering different transmit power levels. By employing the channel emulator, we have also observed the effects of rms delay spread and Doppler spread over the total SI suppression performance. On our IBFD radio setup, the noise floor is around -86 dBm and 67 dB of antenna (passive) suppression is measured. The rms delay spread of our open laboratory environment is measured as 75 ns.

In Fig. 3.9 (a), where the channel emulator rms delay spread value, σ_τ is set to 0 ns (corresponding to open laboratory environment), it can be observed that applying CPNR does not change the performance of TE-TR in the laboratory conditions, but CPNR brings the performance of TE-FR, FE-TR and FE-FR DSIC techniques to the same level as TE-TR for all power levels. At 8 dBm transmit power level,

which corresponds to around 25 dB SNR level in the simulations and where peak total suppression is observed, the improvement by CPNR is measured as 5 dB for FE-TR, and 6 dB for TE-FR and FE-FR techniques. When the rms delay spread is increased to 150 ns, in Fig. 3.9 (b), it can be seen that total suppression performance of TE-TR and TE-FR with CPNR has dropped, while FE-TR and FE-FR with CPNR preserve their performance for all power levels.

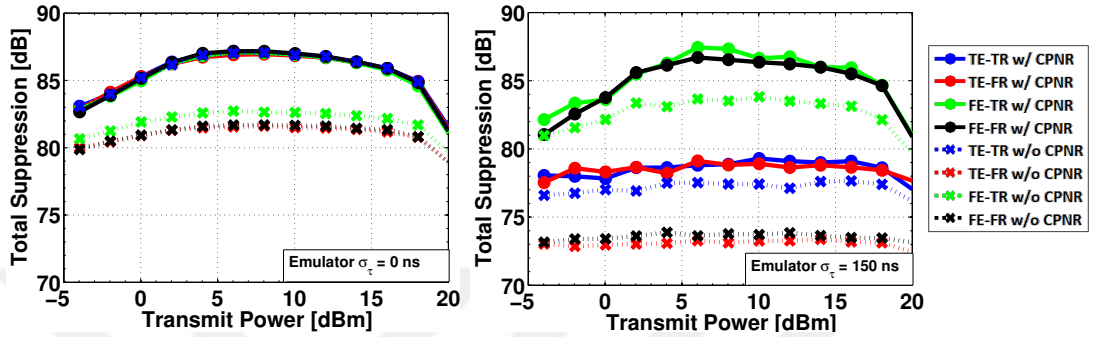

(a) (b)

Figure 3.9 Comparisons of total SI suppression performance measured on the SDR environment integrated with dual port slot coupled antenna for different values of σ_τ in the channel emulator (a) $\sigma_\tau = 0$ ns (b) $\sigma_\tau = 150$ ns.

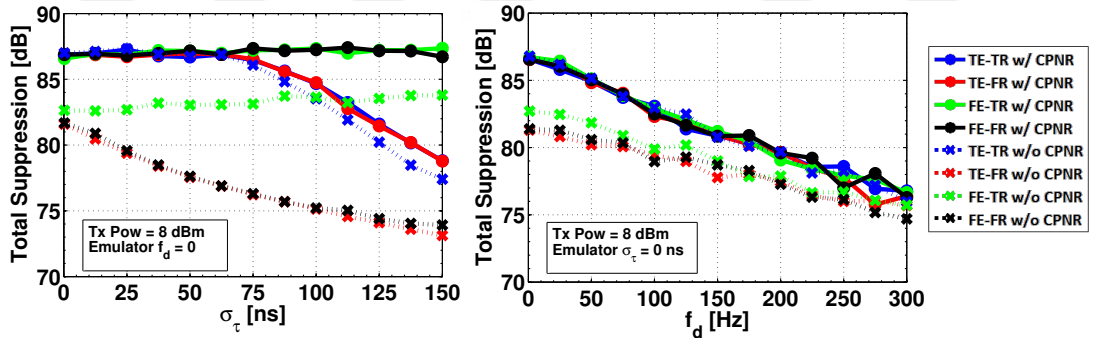

(a) (b)

Figure 3.10 Total SI suppression performance by using channel emulator at 8 dBm transmit power (a) for the increased σ_τ values while $f_d = 0$ Hz (b) for the increased f_d values while $\sigma_\tau = 0$ ns.

In the next test, for 8 dBm transmit power level, we have obtained the total cancellation results for increasing σ_τ and f_d values by employing the channel emulator, as shown in Fig. 3.10 (a) and (b), respectively. Fig. 3.10 (a) depicts that as σ_τ is increased, the total SI suppression performance of FE-FR and FE-TR with CPNR are preserved, while the performance of TE-TR and TE-FR with CPNR degrades starting from 75 ns. The amount of improvement due to CPNR varies among DSIC

techniques and according to the multi-path situation. At $\sigma_\tau = 150$ ns, highest CPNR enhancement is observed for FE-FR by 13 dB, and FE-FR and FE-TR with CPNR outperform TE-TR and TE-FR with CPNR by 9 dB. Fig. 3.10 (b) illustrates the overall total performance degradation for all the techniques when Doppler spread (f_d) is increased, which indicates the packet size should be decreased for updating SI channel estimation. Our observations for the relative behaviour of the DSIC techniques in the tests are consistent with our observations for the simulations.

3.4.1.2 Bidirectional IBFD Communication

In practice, during IBFD communication the reception of the SoI and the total SI suppression are realized at the same time [51]. Therefore, in the second experiment, in order to evaluate the impact of IBFD communication over the SoI, we have established the simple physical layer access scheme depicted in Fig. 3.3 (a) to enable bidirectional IBFD communication between two nodes [7]. For realizing the bidirectional IBFD communication explained in Section 3.1.3, two WARP v3 boards are used as Node 1 and Node 2 integrated with the same dual port slot coupled antenna (Fig. 3.11).

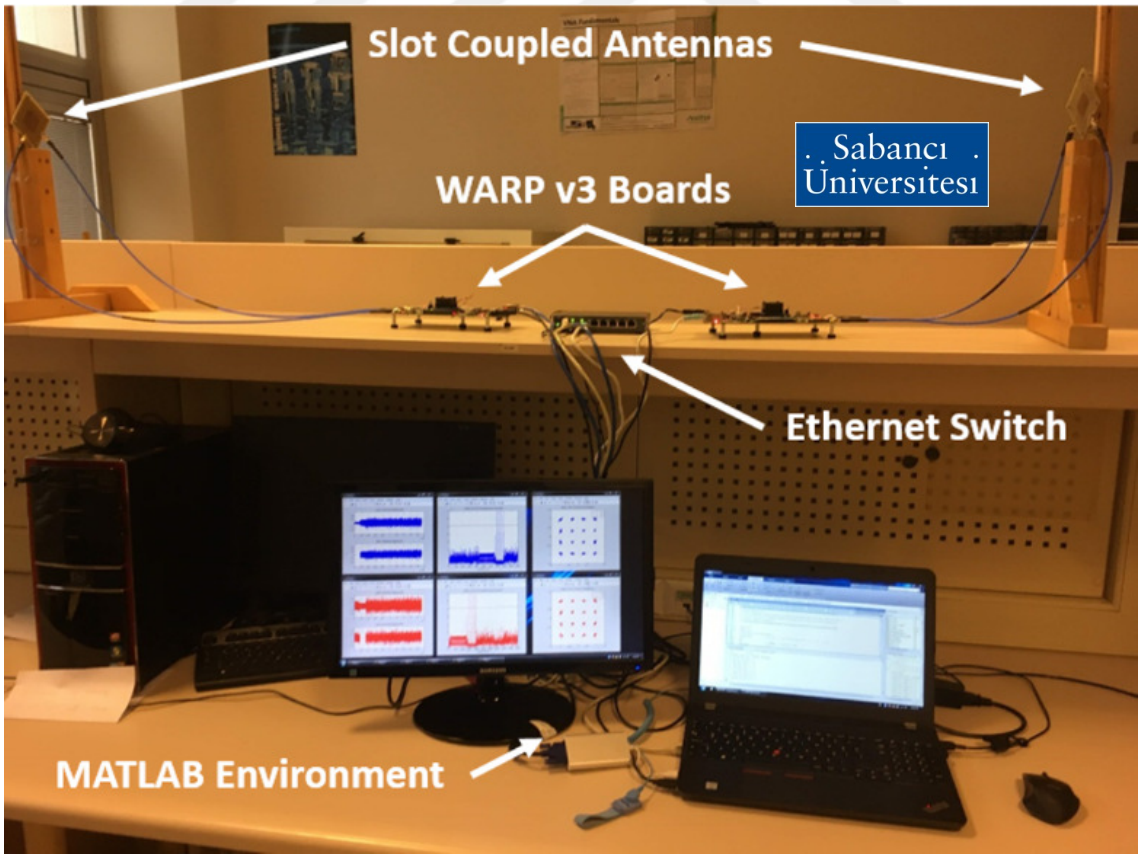

Figure 3.11 Bidirectional IBFD communication set-up

In this set of experiments, we have measured the EVM of the received SoI at the input of the demodulation block seen in Fig. 3.8 with respect to increasing transmit power at Node 1, while the transmit power of Node 2 remains fixed at 8 dBm. EVM is expressed as:

$$EVM = \sqrt{\frac{\frac{1}{L}\sum_{k=1}^{L}\left|\hat{S}_k - S_k\right|^2}{\frac{1}{L}\sum_{k=1}^{L}|S_k|^2}}, \tag{3.13}$$

where L is the symbol length for averaging, $\hat{S}_k$ and S_k are the received symbols and the ideal symbols, respectively [51].

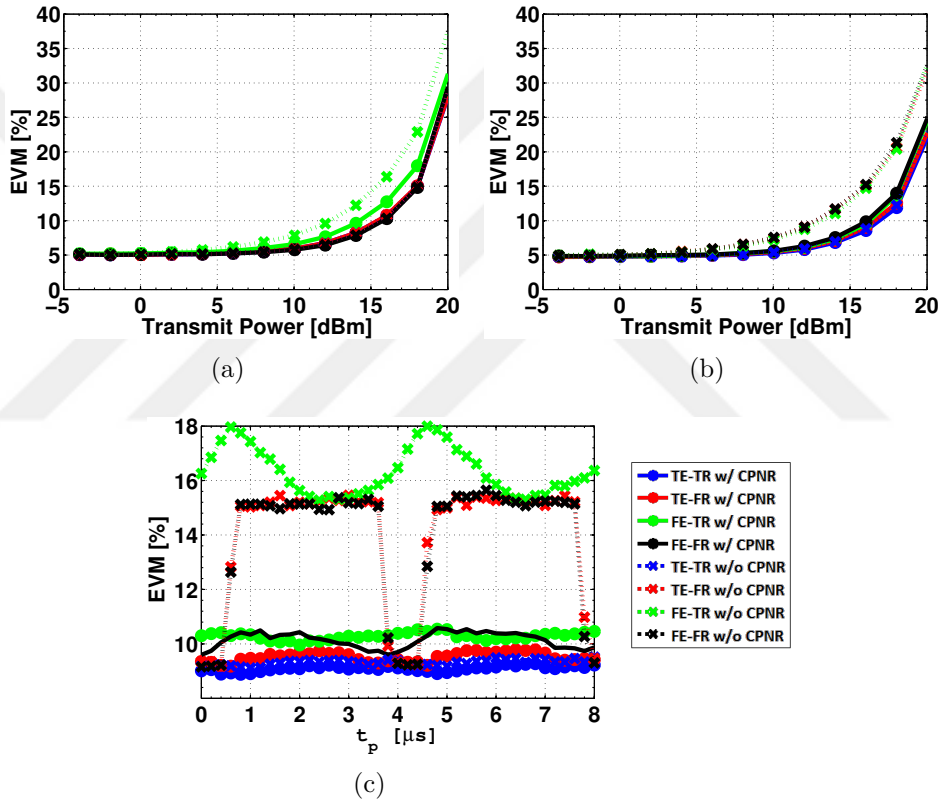

Figure 3.12 EVM performance for bidirectional IBFD communication (a) synchronous case (t_p = 0 ns) (b) asynchronous case (t_p = 2.4 μs) (c) varying propagation delay (t_p) at 15 dBm transmit power.

The EVM values at Node 1 are provided in Fig. 3.12 (a) and (b), considering synchronous and asynchronous cases, respectively. Fig. 3.12 (a) depicts the EVM performance when the two radios are synchronized. This means, the propagation delay (t_p) is negligible, so that the packets of SoI and SI are well aligned at each node. Therefore, while decoding the OFDM symbols of the SoI, the CP noise does not contaminate the SoI, since it does not appear inside the data window. For TE-

TR, applying CPNR changes neither the total SI suppression (as seen in Fig. 3.9 (a)) nor the EVM performance. For the TE-FR and FE-FR techniques, although the total SI performance gets better with CPNR (as seen in Fig. 3.9 (a)), the magnitudes of EVM measures do not change, since the packets are synchronized. Meanwhile, for FE-TR, both the total SI suppression and the EVM performance is improved with CPNR even when packets are synchronized. This is because applying CPNR not only eliminates the CP noise, but also enhances the cancellation performance in the data region.

We have also investigated the effect of CP noise in the asynchronous scenario, considering 2.4[4] μs of propagation delay between two IBFD radios, which represents the case when the CP noise appears in the middle of the data region (See Fig. 3.3 (c)). As depicted in Fig. 3.12 (b), when the CP noise is negligible, no difference is observed on the EVM performance for TE-TR after applying CPNR. For TE-FR, FE-TR, and FE-FR, it is observed that the EVM performance degrades in case of high propagation delay due to CP noise and applying CPNR enhances their performance. Next, we repeat the test for a fixed power level and varying t_{p} values (from 0 μs to 8 μs) covering a duration of two OFDM symbols. The transmit power is set as 15 dB, which is the power level the largest EVM improvement is observed in Fig. 3.12 (b). As shown in Fig. 3.12 (c), when the propagation delay is such that the CP noise appears within the data region of the SoI, EVM values of TE-FR, FE-TR and FE-FR increase to 15 percent level. Applying CPNR brings their levels back to 10 percent. For FE-TR without CPNR, the EVM is highest for all propagation delays, since the entire residual SI signal has ripples inside the data window; whereas, for TE-TR, EVM is low even without CPNR, due to negligible CP noise.

3.4.2 FPGA Implementation and Tests

For FPGA implementation, we have chosen FE-TR with CPNR to be realized on the Virtex-6 LS240T FPGA of the WARP v3 SDR board. For the implementation, all the functional blocks within DSIC in Fig. 3.8 (i.e., the blocks in yellow with/without red for CPNR) are realized [5]. All computations related to DSIC are performed by the FPGA, while the baseband TX chain and SoI RX processing (i.e., blue boxes in

[4] In one OFDM symbol, CP and data have 32 and 128 samples, respectively, and the sampling time is 25 ns. Therefore, the propagation delay (t_{p}) of 2.4 μs corresponds to the middle of the data region.

[5] The implementation is first modeled in System Generator tool [52], which enables the use of model based MATLAB Simulink for FPGA design [53]. Then, it is synthesized by following the Xilinx® design flow and imported into the FPGA on the WARPLab7 framework [50].

Fig. 3.8) are realized in WARPLab7 MATLAB environment. The design consists of six main sub-modules. The number of bits used in the sub-modules are listed in Table 3.2.

Table 3.2 The number of bits used in different sub-modules

Signal Name	Width (I/Q)	Integer Part	Fractional Part
Decimator:			
- Received signal	16 bits	1 bit	15 bits
- Decimator output	16 bits	1 bit	15 bits
LTS Correlator:			
- LTS corr. output	16 bits	1 bit	15 bits
SI Channel Estimator:			
- FFT input	24 bits	1 bit	23 bits
- FFT output	24 bits	3 bits	21 bits
- IFFT output	24 bits	3 bits	21 bits
- SI channel imp. resp.	16 bits	1 bit	15 bits
Time Domain Reconstructor:			
- Convolution output	17 bits	2 bits	15 bits
- Interpolation output	24 bits	4 bits	20 bits
- Reconstructed SI sig.	16 bits	1 bit	15 bits
Transmit Buffer:			
- Transmit signal	16 bits	1 bit	15 bits
Subtractor:			
- Residual signal	16 bits	1 bit	15 bits

Having received the SI signal from the on-board analog-to-digital converter (ADC) into the FPGA with 40 MHz sampling rate, the decimator sub-module filters the samples with the interpolation filter and it downsamples them by 2. Therefore, the signal bandwidth is reduced to 20 MHz and it is stored in a buffer for further processing. The internal processing clock frequency of the FPGA is 160 MHz. After the decimator, the samples are cross-correlated with the known LTS samples stored in a read only memory (ROM) to find the beginning point of the received packet. When the start of packet is detected, the read address of the receiver buffer is set to the beginning of the LTS samples. Here, the received LTS samples are extracted from the buffer and processed by the SI channel estimator sub-module. First, 64-sized FFT operation is performed to convert the signal from time-domain to frequency-domain, then received and known LTS samples are compared to estimate the channel coefficients. Then, the estimated SI channel coefficients are translated into time-domain by the 64-sized IFFT block. Hereby, the impulse response of the SI channel becomes available in a register to be used in the time-domain SI reconstruction stage. In the meantime, all the known transmit symbols are stored in the transmit buffer. As soon as the SI channel impulse response is ready, the SI time-domain reconstructor sub-module reads it from the register and convolves it with the known transmit signal retrieved from the transmit buffer. The reconstructed signal is passed through

the interpolation filter and finally the output is fed into the subtractor sub-module, to be subtracted from the received signal, which is read from the receiver buffer. Hence, the residual signal is prepared to be read by WARPLab7 MATLAB. The details of our FPGA implementation are provided in Appendix A. The experiments performed in Section 3.4.1 are repeated and the performance results are obtained by measuring the residual signal retrieved from the implementation. As it is shown in Fig. 3.13, the Total SI suppression and EVM results obtained from MATLAB and FPGA implementations are overlap perfectly, with negligibly small deviations due to quantization errors.

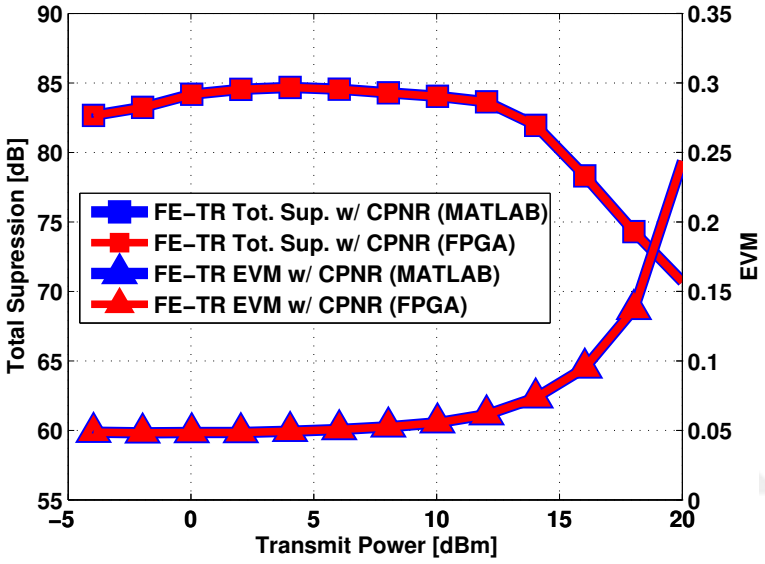

Figure 3.13 Comparison of total SI suppression and EVM performances obtained from bidirectional communication experiment ($t_{\mathrm{p}} = 2.4\ \mu$s) for MATLAB and FPGA implementations.

3.5 Complexity Analysis

In order to assess the computational complexity of DSIC techniques with CPNR, we consider the number of floating point operations (flops) including all operations in terms of additions and multiplications, similar to [27] and [1]. In Table 3.3, complexity of DSIC techniques with and without CPNR are presented. As it is shown in Table 3.3, when CPNR is employed, tone insertion step does not affect the complexity of the estimation algorithms since the additional tones are within the size of K. Only, the complexity of FR is increased by a factor of two, due to enhanced reconstruction of CP region.

Table 3.3 Complexity of DSIC Techniques with and without CPNR

		Complexity			
		Estimation		Reconstruction	
		Multiplications	Additions	Multiplications	Additions
w/ CPNR	TE-TR	$4(K.K_{\mathrm{CP}})$	$4(K.K_{\mathrm{CP}})$	$(6K\log_2(K)-17K+36)N$	$(9K\log_2(K)-7K+12)N$
	TE-FR	$4(K.K_{\mathrm{CP}})+2K\log_2(K)-7K+12$	$4(K.K_{\mathrm{CP}})+3K\log_2(K)-3K+4$	$2(2K\log_2(K)-3K+12)N$	$2(3K\log_2(K)-K+4)N$
	FE-TR	$4K\log_2(K)-14K+24$	$6K\log_2(K)-6K+8$	$(6K\log_2(K)-17K+36)N$	$(9K\log_2(K)-7K+12)N$
	FE-FR	$2K\log_2(K)-7K+12$	$3K\log_2(K)-3K+4$	$2(2K\log_2(K)-3K+12)N$	$2(3K\log_2(K)-K+4)N$
w/o CPNR	TE-TR	$4(K.K_{\mathrm{CP}})$	$4(K.K_{\mathrm{CP}})$	$(6K\log_2(K)-17K+36)N$	$(9K\log_2(K)-7K+12)N$
	TE-FR	$4(K.K_{\mathrm{CP}})+2K\log_2(K)-7K+12$	$4(K.K_{\mathrm{CP}})+3K\log_2(K)-3K+4$	$(2K\log_2(K)-3K+12)N$	$(3K\log_2(K)-K+4)N$
	FE-TR	$4K\log_2(K)-14K+24$	$6K\log_2(K)-6K+8$	$(6K\log_2(K)-17K+36)N$	$(9K\log_2(K)-7K+12)N$
	FE-FR	$2K\log_2(K)-7K+12$	$3K\log_2(K)-3K+4$	$(2K\log_2(K)-3K+12)N$	$(3K\log_2(K)-K+4)N$

Table 3.4 demonstrates a summary of the results for total SI suppression and EVM performance of different DSIC techniques with and without CPNR, along with their computational complexity considering the parameters listed in Table 3.1. The total SI suppression values are given for different σ_τ values at 8 dBm transmit power level; the EVM values are listed for $t_{\mathrm{p}} = 2.4$ μs and for $\sigma_\tau = 0$ ns at 8 dBm and at 15 dBm transmit power levels. As it is seen in Table 3.4, despite the fact that applying CPNR doubles the complexity of TE-FR and FE-FR techniques, their complexity is still 20 percent below the complexity of TE-TR and FE-TR. Moreover, FE-FR and FE-TR with CPNR preserve their performance under large delay spreads, while TE-TR and TE-FR are demonstrating performance degradation, showing the robustness of frequency-domain estimation against time-domain estimation. As an example, at $\sigma_\tau = 150$ ns, FE-FR with CPNR (having 86.53 dB total SI suppression) outperforms approximately 9 dB over TE-TR without CPNR (having 77.42 dB total SI suppression), and it is 20 percent less expensive in terms of computational complexity. On the other hand, it can be observed that the EVM performances for each DSIC technique are recovered to the same level by utilizing CPNR.

Table 3.4 Summary of Complexity and Performance

			Total SI Suppression (dB) at Tx. Pow. = 8 dBm				EVM (%) at $t_{\mathrm{p}} = 2.4$ μs, $\sigma_\tau = 0$ ns	
		Flop Count	$\sigma_\tau = 0$ ns	$\sigma_\tau = 50$ ns	$\sigma_\tau = 100$ ns	$\sigma_\tau = 150$ ns	Tx. Pow. = 8 dBm	Tx. Pow. = 15 dBm
w/ CPNR	TE-TR	$435392 \rightarrow \sim 1.0$x	87.11	87.15	84.44	78.88	5.06	9.12
	TE-FR	$345488 \rightarrow \sim 0.8$x	86.95	87.32	84.46	78.82	5.16	9.74
	FE-TR	$429792 \rightarrow \sim 1.0$x	87.05	87.71	87.35	87.33	5.26	10.10
	FE-FR	$337296 \rightarrow \sim 0.8$x	87.17	87.47	87.32	86.53	5.28	10.18
w/o CPNR	TE-TR	$435392 \rightarrow \sim 1.0$x	87.07	87.41	83.53	77.42	5.06	9.34
	TE-FR	$177488 \rightarrow \sim 0.4$x	81.61	77.63	75.06	73.11	6.55	15.22
	FE-TR	$429792 \rightarrow \sim 1.0$x	82.64	82.72	83.27	83.52	6.33	15.28
	FE-FR	$169296 \rightarrow \sim 0.4$x	81.69	77.6	75.48	73.77	6.55	14.94

4. NON-LINEAR SELF-INTERFERENCE CANCELLATION FOR IN-BAND FULL-DUPLEX RADIOS

In this chapter, we consider the non-linearity problem at high transmit power levels in In-Band Full-Duplex (IBFD) radios, and we propose a new, switched radio architecture along with new time-domain estimation and neural network based frequency-domain estimation algorithms for non-linear self-interference (SI) cancellation. In this architecture, non-linear and linear SI cancellation are decoupled, so that non-linear estimation can be performed separately from and prior to linear cancellation, and the non-linear SI signal estimated by the proposed algorithms is provided as a reference to linear cancellation. Our experimental results obtained on an orthogonal frequency division multiplexing (OFDM) based IBFD software defined radio set-up demonstrate that the amount of total SI suppression is improved by up to 13 dB over existing schemes. Moreover, proposed non-linear SI cancellation solution is immune to changes in the multi-path environment; unlike existing schemes, which require re-optimization of model parameters and calculation of coefficients for each setting. Last but not least, with the proposed non-linear algorithms, estimation overhead is alleviated, and computational complexity is reduced by four to six orders of magnitude.

4.1 Switched IBFD Radio Architecture

In this section, we propose a swithed IBFD radio (IBFD-SW) architecture, where non-linear and linear effects are handled separately, as depicted in Fig. 4.1. In this architecture, non-linear SI signal can be approximated, reconstructed and provided to linear SI cancellation as a realistic reference with high accuracy, which represents non-linear effects of the transmitter PA and receiver LNA.

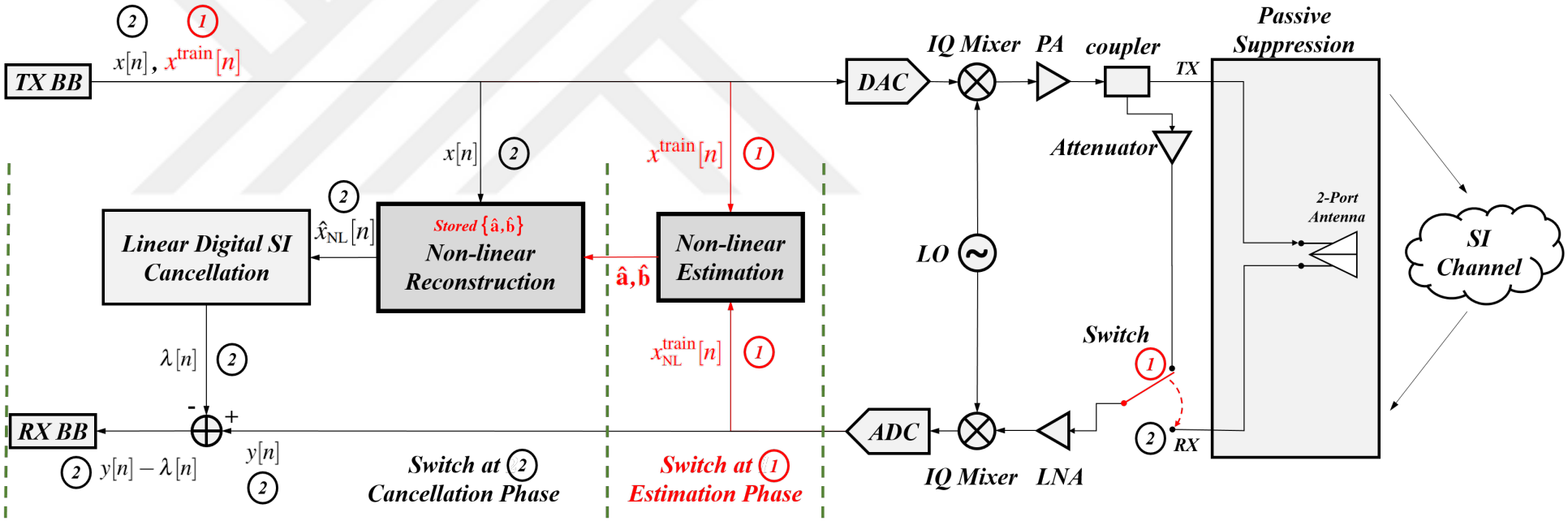

Figure 4.1 Proposed and implemented switched IBFD radio architecture (IBFD-SW)

The proposed IBFD-SW architecture has two modes for estimation and cancellation phases. During the estimation (training) phase, i.e. when the switch is at position 1 as shown in Fig. 4.1, a loop-back is formed from the transmitter to the receiver, and the analog-to-digital converter (ADC) output is provided as the SI signal to non-linear estimation block along with the known baseband transmit signal. The coefficients of the non-linear model are obtained based on the loop-backed SI signal which involves only the non-linear effects, but none of the linear effects of the SI channel. The learned non-linear coefficients are stored at the non-linear reconstruction block, as they can be re-used in the subsequent transmissions during reconstruction phase.

During the reconstruction phase, when the switch is moved to position 2 as shown in Fig. 4.1, the learned and stored non-linear coefficients are used with the baseband transmit signal to generate the non-linear reference SI signal. Linear SI cancellation utilizes the non-linear reference SI signal along with received baseband SI signal to estimate the SI channel and reconstruct the SI signal. Linear SI channel estimation is performed on the LTS field in the preamble of the received OFDM packet and then SI channel estimate is applied to the data part of the OFDM packet in order to reconstruct the SI signal. Finally, SI cancellation is achieved by subtracting the reconstructed SI signal from the received signal [3]. For digital linear SI cancellation, time-domain estimation (TE) or frequency- domain estimation (FE) plus time-domain reconstruction (TR) or frequency- domain reconstruction (FR) are employed. Hence, four linear cancellation methods, namely, TE-TR, TE-FR, FE-TR, FE-FR, are considered together with non-linear cancellation (estimation) for the first time in this thesis.

4.2 Non-Linear SI Estimation Algorithms for Switched IBFD Radio

4.2.1 Time-Domain Non-Linear SI Estimation

Implementing the MP model in (2.13) and training it on our proposed IBFD-SW test set-up (details of the set-up can be found in the beginning of Section 4.3), we have optimized its parameters, degree P and memory M, as provided in Appendix B, and we have shown that highest SI cancellation is achieved when $M = 0$ and $P = 5$. For our IBFD radio, with $M = 0$, we can re-write $x_{\text{NL}}[n]$ in (2.13) as:

$$x_{\text{NL}}[n] \;=\; \sum_{i=1,odd}^{P} c_i x[n]\,|x[n]|^{i-1}. \tag{4.1}$$

Considering $x[n]$ in complex form, the coefficients, c_i can be directly obtained in complex form by employing Least Squares (LS) method. We name this solution as non-linear complex estimation (NLC).

Next, we consider the samples of known transmit signal, $x[n]$, in (4.1) in polar form as $x[n] = r[n]\text{exp}\Big(j\varphi[n]\Big)$, where $r[n]$ and $\phi[n]$ are the magnitude and phase components. This way, $x_{\text{NL}}[n]$ is expressed as:

$$x_{\text{NL}}[n] \;=\; r_{\text{NL}}\Big(r[n]\Big)\text{exp}\Big(j\varphi[n] + j\varphi_{\text{NL}}\Big(r[n]\Big)\Big) \;=\; r_{\text{NL}}[n]\text{exp}\Big(j\varphi[n] + j\varphi_{\text{NL}}[n]\Big). \tag{4.2}$$

where $r_{\text{NL}}[n]$ and $(\phi[n] + \varphi_{\text{NL}}[n])$ are the magnitude and the phase of $x_{\text{NL}}[n]$ [54]. Note that, $\phi[n]$ remains the same as it is generated from the transmit chain, whereas we propose to estimate $r_{\text{NL}}[n]$ and $\varphi_{\text{NL}}[n]$ via the polynomial model:

$$\begin{aligned} r_{\text{NL}}[n] &= \sum_{i=1,odd}^{P} a_i r^i[n], \\ \varphi_{\text{NL}}[n] &= \sum_{i=0}^{P} b_i r^i[n]. \end{aligned} \tag{4.3}$$

Here, P is the polynomial order, and a_i and b_i are the respective coefficients of the ith order terms of the magnitude and phase models, respectively. We name this solution as non-linear polar estimation method (NLP) where, again, the even ordered terms are not included in the magnitude model in (4.3) as they generate intermodulation components outside the signal band. Meanwhile, all odd and even ordered terms are included in the phase model due to phase wrapping. This way, in the proposed NLP method, non-linear SI is estimated not only more accurately, but also with lower complexity (due to real operations), as compared to the NLC method.

The coefficients a_i and b_i can be predicted via linear optimization techniques, here we employ LS estimation, considering a sequence of data samples for training. The training (estimation) phase is enabled by setting the switch to position 1 in the switched IBFD radio in Fig. 4.1 (b) and the training data samples, $x^{\text{train}}[n]$ (in polar representation, $x^{\text{train}}[n] \;=\; r^{\text{train}}[n]\text{exp}\Big(j\varphi^{\text{train}}[n]\Big)$) are transmitted. After loop-back, without the SI channel effects, we obtain the non-linearly distorted version of each training sample at the output of the ADC as:

$$x_{\text{NL}}^{\text{train}}[n] \;=\; r_{\text{NL}}^{\text{train}}[n]\exp\Big(j\varphi^{\text{train}}[n]+j\varphi_{\text{NL}}^{\text{train}}[n]\Big), \tag{4.4}$$

where $r_{\text{NL}}^{\text{train}}[n]$ is the distorted version of the magnitude $r^{\text{train}}[n]$ and $\varphi_{\text{NL}}^{\text{train}}[n]$ is the additional phase due to non-linearity.

For a training length of L-samples, the vector notations of the observed magnitude distortion, $r_{\text{NL}}^{\text{train}}[n]$, and phase distortion, $\varphi_{\text{NL}}^{\text{train}}[n]$, in (4.4) are approximated by using (4.3) as $\mathbf{r}_{\mathbf{NL}}^{\text{train}} = \mathbf{U}_{\text{r}}\mathbf{a}$, $\varphi_{\mathbf{NL}}^{\text{train}} = \mathbf{U}_{\varphi}\mathbf{b}$, where $\mathbf{r}_{\mathbf{NL}}^{\text{train}} = \Big[r_{\text{NL}}^{\text{train}}[1] \;\; r_{\text{NL}}^{\text{train}}[2] \;\cdots\; r_{\text{NL}}^{\text{train}}[n] \;\cdots\; r_{\text{NL}}^{\text{train}}[L]\Big]^T$ and $\varphi_{\mathbf{NL}}^{\text{train}} = \Big[\varphi_{\text{NL}}^{\text{train}}[1] \;\; \varphi_{\text{NL}}^{\text{train}}[2] \;\cdots\; \varphi_{\text{NL}}^{\text{train}}[n] \;\cdots\; \varphi_{\text{NL}}^{\text{train}}[L]\Big]^T$ are $L\times 1$ vectors constructed from L observation samples, and $\mathbf{a}=[a_1 \; a_3 \; \cdots \; a_i \; \cdots \; a_P]^T$ and $\mathbf{b}=[b_1 \; b_2 \; \cdots \; b_i \; \cdots \; b_P]^T$ are the coefficient vectors of length $(P+1)/2$ and $(P+1)$ respectively. The matrices $\mathbf{U}_{\text{r}}$ and $\mathbf{U}_{\varphi}$ are obtained from the magnitude of the L-transmitted training samples as follows:

$$\mathbf{U}_{\text{r}} = \begin{bmatrix} r^{\text{train}}[1] & (r^{\text{train}}[1])^3 & (r^{\text{train}}[1])^5 & \cdots & (r^{\text{train}}[1])^P \\ \vdots & \vdots & \vdots & \ddots & \vdots \\ r^{\text{train}}[L] & (r^{\text{train}}[L])^3 & (r^{\text{train}}[L])^5 & \cdots & (r^{\text{train}}[L])^P \end{bmatrix}_{L\times\frac{(P+1)}{2}},$$

$$\mathbf{U}_{\varphi} = \begin{bmatrix} 1 & r^{\text{train}}[1] & (r^{\text{train}}[1])^2 & \cdots & (r^{\text{train}}[1])^P \\ \vdots & \vdots & \vdots & \ddots & \vdots \\ 1 & r^{\text{train}}[L] & (r^{\text{train}}[L])^2 & \cdots & (r^{\text{train}}[L])^P \end{bmatrix}_{L\times(P+1)}.$$

The LS estimator minimizes the squared distance between the observed data and the estimated data by optimizing the unknown model coefficients for $\mathbf{a}$ and $\mathbf{b}$. For $\mathbf{a}$ and $\mathbf{b}$ the LS estimators $\hat{\mathbf{a}}$ and $\hat{\mathbf{b}}$ are expressed as:

$$\hat{\mathbf{a}} \;=\; \Big(\mathbf{U}_{\text{r}}^{\text{T}}\mathbf{U}_{\text{r}}\Big)^{-1}\mathbf{U}_{\text{r}}^{\text{T}}\mathbf{r}_{\mathbf{NL}}^{\text{train}},\; \hat{\mathbf{b}} \;=\; \Big(\mathbf{U}_{\varphi}^{\text{T}}\mathbf{U}_{\varphi}\Big)^{-1}\mathbf{U}_{\varphi}^{\text{T}}\varphi_{\mathbf{NL}}^{\text{train}}. \tag{4.5}$$

The elements of $\hat{\mathbf{a}}$ and $\hat{\mathbf{b}}$ estimated as in (4.5) and they are applied in (4.3). Then, the magnitude and phase approximations are substituted in (4.2) together with transmitted data samples $x[n]$, in the non-linear SI signal reconstruction phase during the cancellation phase of the proposed architecture, with the switch at position 2 in Fig. 4.1. Eventually, the following non-linear reference SI signal, $\hat{x}_{\text{NL}}[n]$ is constructed and passed to the linear SI cancellation stage:

$$\hat{r}_{\text{NL}}[n] = \sum_{i=1,odd}^{P} \hat{a}_i r^i[n],$$

$$\hat{\varphi}_{\text{NL}}[n] = \sum_{i=0}^{P} \hat{b}_i r^i[n], \tag{4.6}$$

$$\hat{x}_{\text{NL}}[n] \;=\; \hat{r}_{\text{NL}}[n]\exp\Big(\varphi[n] + \hat{\varphi}_{\text{NL}}[n]\Big).$$

4.2.2 Frequency-Domain Non-Linear SI Estimation

Considering our IBFD-SW radio architecture during the non-linear estimation phase, and representing the OFDM signal in frequency domain, the non-linear SI signal obtained via loop-back (isolated from SI channel effects) is depicted in Fig. 4.2 (a). We propose to estimate the non-linear SI signal in frequency-domain by first estimating the non-linearity per each sub-carrier via a neural network based solution (Fig. 4.2 (b), (c)) and then reconstructing the OFDM signal from the reconstructed subcarriers as in Fig. 4.2 (d). We name this method as, Non-Linear Frequency-domain estimation (NLF), details of which are derived, as explained next.

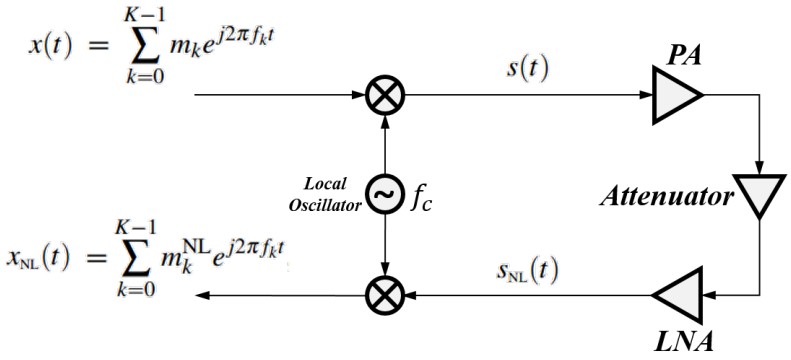

(a)

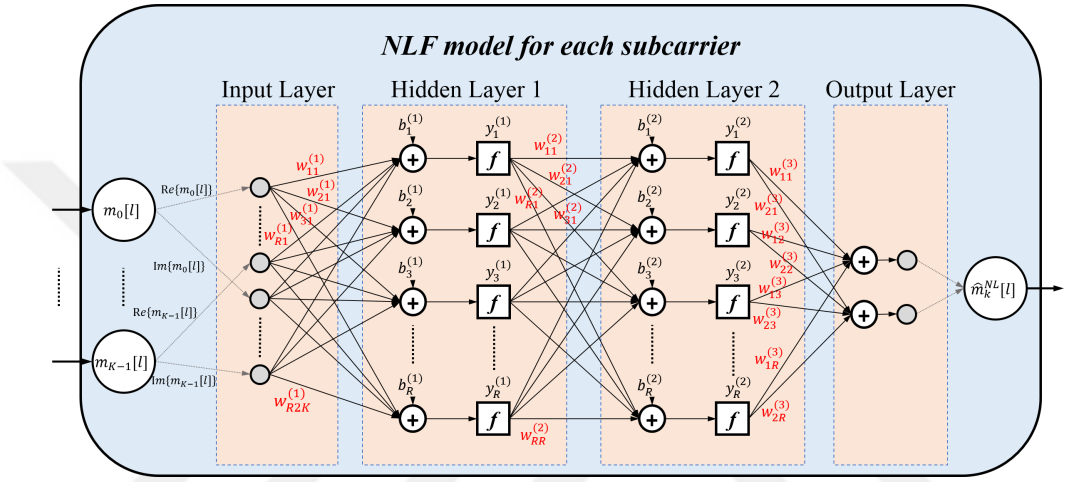

(b)

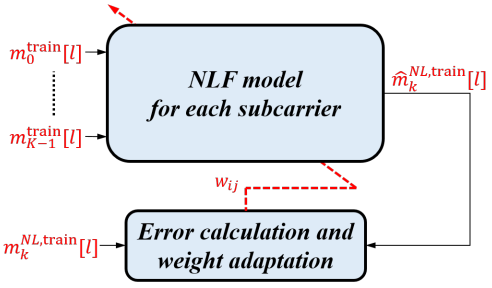

(c)

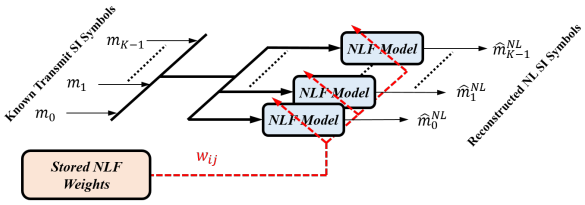

(d)

Figure 4.2 (a) IBFD-SW radio during non-linear estimation phase (when switch in Fig. 4.1 is at 1) (b) Neural network based non-linear frequncy domain estimation (NLF) per subcarrier (c) NLF model weight adaptation per subcarrier (d) Non-linear reconstruction during cancellation phase

Basically, the transmit SI signal $x(t)$ in Fig. 4.2 (a), is an OFDM signal composed of K orthogonal subcarriers f_k where each subcarrier is modulated by an M-QAM complex information symbol m_k. $x(t)$ is expressed as:

$$x(t) \;=\; \sum_{k=0}^{K-1} m_k e^{j2\pi f_k t},\; 0 \le t < T, \tag{4.7}$$

where T is the OFDM signal duration, and $f_k = k/T$ is the k_{th} subcarrier (indexed with $k = 0, 1, 2, ..., K-1$) carrying the m_k information symbol. When $x(t)$ is up-converted to RF level with a carrier frequency f_c, the passband equivalent of $x(t)$ can be expressed as:

$$s(t) = \mathrm{Re}\Big\{x(t)e^{j2\pi f_c t}\Big\} = \mathrm{Re}\left\{\sum_{k=0}^{K-1} m_k e^{j2\pi(f_c+f_k)t}\right\} = \tfrac{1}{2}\left(\sum_{k=0}^{K-1} m_k e^{j2\pi f'_k t} + \sum_{k=0}^{K-1} m_k e^{-j2\pi f'_k t}\right) \tag{4.8}$$

where $f'_k = f_c + f_k$ is the frequency of the k^{th} subcarrier at RF level. When $s(t)$ is provided to the PA at the transmitter, the received SI signal, $s_{\text{NL}}(t)$ obtained at the output of the LNA from loop-back can be expressed as follows:

$$s_{\text{NL}}(t) \;=\; \sum_{i=1}^{P} \gamma_i s^i(t), \tag{4.9}$$

where γ_i's are the polynomial coefficients and P is the polynomial order, provided as $P = 5$ from Appendix B. $s_{\text{NL}}(t)$ contains $s(t)$ and its harmonics, as well as the intermodulation products. By substituting (4.8) into (4.9), $s_{\text{NL}}(t)$ can be re-expressed as follows:

$$s_{\text{NL}}(t) \;=\; \sum_{i=1}^{P} \gamma_i s^i(t) \;=\; \sum_{i=1}^{P} \gamma_i \left(\tfrac{1}{2}\right)^i \left(\sum_{k=0}^{K-1} m_k e^{j2\pi f'_k t} + \sum_{k=0}^{K-1} m_k e^{-j2\pi f'_k t}\right)^i$$

$$s_{\text{NL}}(t) \;=\; \sum_{i=1}^{P} \gamma_i \left(\tfrac{1}{2}\right)^i \left(\sum_{\substack{i_0=-i \\ |i_0|+\cdots+|i_{K-1}|=i}}^{i} \sum_{i_1=-i}^{i} \cdots \sum_{i_{K-1}=-i}^{i} \binom{i}{|i_0|,\cdots,|i_{K-1}|} \prod_{n=0}^{K-1} m_n^{|i_n|} e^{j2\pi \sum_{n=0}^{K-1} i_n f'_n t}\right), \tag{4.10}$$

where $\binom{i}{|i_0|,\cdots,|i_{K-1}|} = \frac{i!}{|i_0|!\ldots|i_{K-1}|!}$ is the multinomial coefficient. (4.10) demonstrates that, at the output of the non-linear system, the intermodulation components are the

results of the linear combinations of subcarrier frequencies each formed as $\sum_{n=0}^{K-1} i_n f'_n$ where the i_n coefficients are integer values between $-i$ and i. Moreover, in (4.10), the sum of the absolute values of the coefficients $|i_0|+|i_1|+\cdots+|i_{K-1}|$ should be equal to i, where i represents the order for the given intermodulation. The amplitude of the corresponding intermodulation component is proportional to the product of the powers of the symbols m_k's carried by the subcarriers, where the powers are determined by the absolute values of the coefficients i_n. Odd-order intermodualtion components are more important, as they fall in band. Rest of the harmonics and intermodulation components which are obtained from even-orders can be suppressed by utilizing filters [55].

At this point, we explain (4.10) with an example with two subcarriers, as depicted in Fig. 4.3. By providing an input signal shown in Fig. 4.3 (a) with subcarriers f'_4 and f'_5 enabled for carrying information symbols, m_4 and m_5, respectively, the harmonics and intermodulation components expressed in (4.10) at the output can be observed in Fig. 4.3 (b), where the parameters are set as $K=10$ and $P=9$. The output signal for the example is expressed as:

$$s_{\text{NL}}^{example}(t) = \sum_{k=0}^{K-1=9} \left(\sum_{i=1,odd}^{P=9} \gamma_i \left(\tfrac{1}{2}\right)^i \sum_{\substack{i_4=-i \\ |i_4|+|i_5|=i \\ i_4 f'_4 + i_5 f'_5 = \pm f'_k}}^{i} \sum_{i_5=-i}^{i} \binom{i}{|i_4|,|i_5|} m_4^{|i_4|} m_5^{|i_5|} \right) e^{\pm j2\pi \overbrace{(i_4 f'_4 + i_5 f'_5)}^{f'_k} t}, \tag{4.11}$$

By excluding the out-band components with the selection of odd-ordered terms in (4.10) and considering in-band subcarriers formed by $\sum_{n=0}^{K-1} i_n f'_n = \pm f'_k$, i.e. by generalizing (4.11), (4.10) can be re-written as:

$$s_{\text{NL}}(t) = \sum_{k=0}^{K-1} \left(\sum_{i=1,odd}^{P} \gamma_i \left(\tfrac{1}{2}\right)^i \sum_{\substack{i_0=-i \\ |i_0|+\cdots+|i_{K-1}|=i \\ i_0 f'_0 + \cdots + i_{K-1} f'_{K-1} = \pm f'_k}}^{i} \sum_{i_1=-i}^{i} \cdots \sum_{i_{K-1}=-i}^{i} \binom{i}{|i_0|,\cdots,|i_{K-1}|} \prod_{n=0}^{K-1} m_n^{|i_n|} \right) e^{\pm j2\pi f'_k t}, \tag{4.12}$$

Down-conversion of (4.12) from RF level to the baseband yields the baseband $x_{\text{NL}}(t)$ signal as:

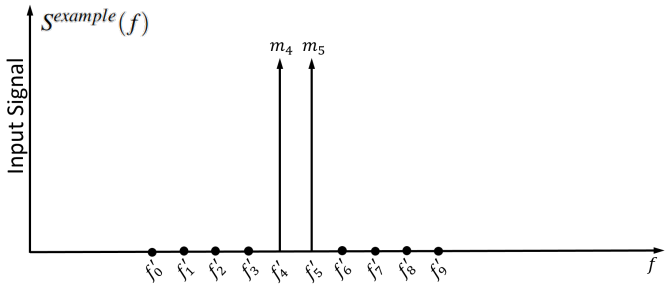

(a)

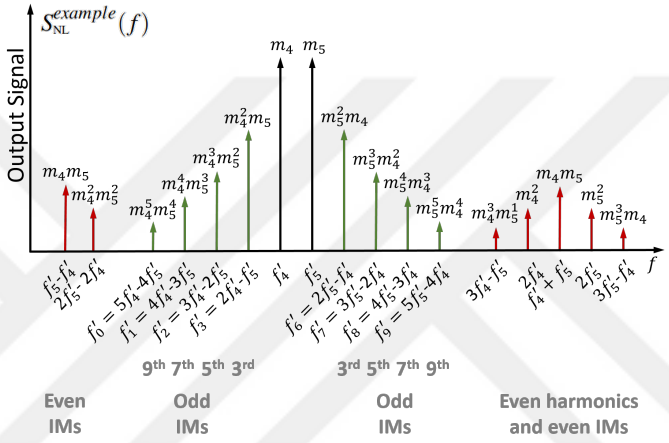

(b)

Figure 4.3 Harmonics and intermodualtions created by two subcarriers in a non-linear RF system (a) frequency-domain representation of the input signal ($S^{example}(f)$) (b) frequency-domain representation of the output signal ($S_{\mathrm{NL}}^{example}(f)$)

$$x_{\mathrm{NL}}(t) = \sum_{k=0}^{K-1} \underbrace{\left(\sum_{i=1,odd}^{P} 2\gamma_i \left(\frac{1}{2}\right)^i \sum_{\substack{i_0=-i \\ |i_0|+\cdots+|i_{K-1}|=i \\ i_0 f'_0+\cdots+i_{K-1}f'_{K-1}=\pm f'_k}}^{i} \sum_{i_1=-i}^{i} \cdots \sum_{i_{K-1}=-i}^{i} \binom{i}{|i_0|,\cdots,|i_{K-1}|} \prod_{n=0}^{K-1} m_n^{|i_n|} \right)}_{m_k^{\mathrm{NL}}} e^{j2\pi f_k t} = \sum_{k=0}^{K-1} m_k^{\mathrm{NL}} e^{j2\pi f_k t}, \tag{4.13}$$

where m_k^{NL} is the received information symbol carried by the k^{th} subcarrier which is a non-linearly function of all the transmitted information symbols $(m_0, ..., m_{K-1})$:

$$m_k^{\mathrm{NL}} = \sum_{i=1,odd}^{P} 2\gamma_i \left(\tfrac{1}{2}\right)^i \sum_{\substack{i_0=-i \\ |i_0|+\cdots+|i_{K-1}|=i \\ i_0 f'_0+\cdots+i_{K-1}f'_{K-1}=\pm f'_k}}^{i} \sum_{i_1=-i}^{i} \cdots \sum_{i_{K-1}=-i}^{i} \binom{i}{|i_0|,\cdots,|i_{K-1}|} \prod_{n=0}^{K-1} m_n^{|i_n|}. \tag{4.14}$$

However, the number of multinomial coefficients in (4.14) is very high which will result in high computational cost. Moreover, we still need to estimate γ_i in (4.14).

At this point, we apply a real-valued neural network based solution in NLF, for modeling of m_k^{NL} in (4.14) per subcarrier k. Each neural network based NLF model is composed of input, hidden and output layers, as depicted in Fig. 4.2 (b). In this model, the relationship between $\hat{m}^{\mathrm{NL}}$ (approximation of m_k^{NL}) and m_k's is obtained as follows:

$$\begin{aligned}
y_r^{(1)} &= f\left(\sum_{k=0}^{K-1} w_{r(k+1)}^{(1)} \mathrm{Re}\{m_k\} + \sum_{k=0}^{K-1} w_{r(K+k+1)}^{(1)} \mathrm{Im}\{m_k\} + b_r^{(1)}\right),\ r \in [1,2,...,R], \\
y_r^{(2)} &= f\left(\sum_{i=1}^{R} w_{ri}^{(2)} y_i^{(1)} + b_r^{(2)}\right),\ r \in [1,2,...,R], \\
\mathrm{Re}\{\hat{m}_k^{\mathrm{NL}}\} &= \sum_{i=1}^{R} w_{1i}^{(3)} y_i^{(2)}, \\
\mathrm{Im}\{\hat{m}_k^{\mathrm{NL}}\} &= \sum_{i=1}^{R} w_{2i}^{(3)} y_i^{(2)}, \\
\hat{m}_k^{\mathrm{NL}} &= \mathrm{Re}\{\hat{m}_k^{\mathrm{NL}}\} + j\mathrm{Im}\{\hat{m}_k^{\mathrm{NL}}\}.
\end{aligned} \tag{4.15}$$

In (4.15), $y_r^{(1)}$ and $y_r^{(2)}$ are the outputs of r^{th} neurons of hidden layer 1 and 2, respectively. R denotes the total number of neurons in each hidden layer. $b_r^{(1)}$ and $b_r^{(2)}$ indicate the bias of r^{th} neurons of hidden layer 1 and 2, respectively. $w_{ij}^{(v)}$ represent the synaptic weights connecting neurons at layer v ($v \in [1,2,3]$) as depicted in Fig. 4.2 (b) and f represents the non-linear activation function.

The weights in (4.15) are estimated by means of a training data set in order to minimize the cost function as depicted in Fig. 4.2 (c). Here, for the cost function, total mean square error (MSE), Ψ, is calculated between the desired output $m_k^{\mathrm{NL,train}}[l]$ and the estimated output $\hat{m}_k^{\mathrm{NL,train}}[l]$ for the l^{th} training instant as follows:

$$\Psi = \frac{1}{2L} \sum_{l=1}^{L} \left[\left(\mathrm{Re}\{m_k^{\mathrm{NL,train}}[l]\} - \mathrm{Re}\{\hat{m}_k^{\mathrm{NL,train}}[l]\} \right)^2 + \left(\mathrm{Im}\{m_k^{\mathrm{NL,train}}[l]\} - \mathrm{Im}\{\hat{m}_k^{\mathrm{NL,train}}[l]\} \right)^2 \right], \tag{4.16}$$

where L is the total number of training samples in the training data set. The weights connected to layer v are updated as follows:

$$w_{ij}^{(v)}[l+1] = w_{ij}^{(v)}[l] + \Delta w_{ij}^{(v)}[l], \tag{4.17}$$

$w_{ij}^{(v)}[l]$ is the weight for l^{th} training data and the amount of adjustment $\Delta w_{ij}^{(v)}[l]$ is computed by Levenberg-Marquardt algorithm [56], in which the cost function (4.16) is iteratively minimized until the preset target performance is achieved. Initial weights are chosen randomly and converges iteratively towards their optimum values as MSE is minimized. Once all weights, $w_{ij}^{(v)}[l]$, are obtained during estimation phase, they are stored to be utilized in reconstruction of the non-linear SI signal.

During the cancellation phase, non-linear SI symbols $\hat{m}_k^{\mathrm{NL}}$ at each subcarrier are reconstructed by utilizing $w_{ij}^{(v)}[l]$ and $m_0, ..., m_{K-1}$ as illustrated in Fig. 4.2 (d). Eventually, the reconstructed non-linear reference SI symbols $\hat{m}_0^{\mathrm{NL}}, ..., \hat{m}_{K-1}^{\mathrm{NL}}$ are passed to the linear SI cancellation stage in frequency-domain. They can be also provided in time-domain as $\hat{x}_{\mathrm{NL}}[n]$ after applying IFFT and CP and preamble insertion operations. The implementation of proposed NLF estimation in IBFD-SW radio architecture is depicted in Fig. 4.4.

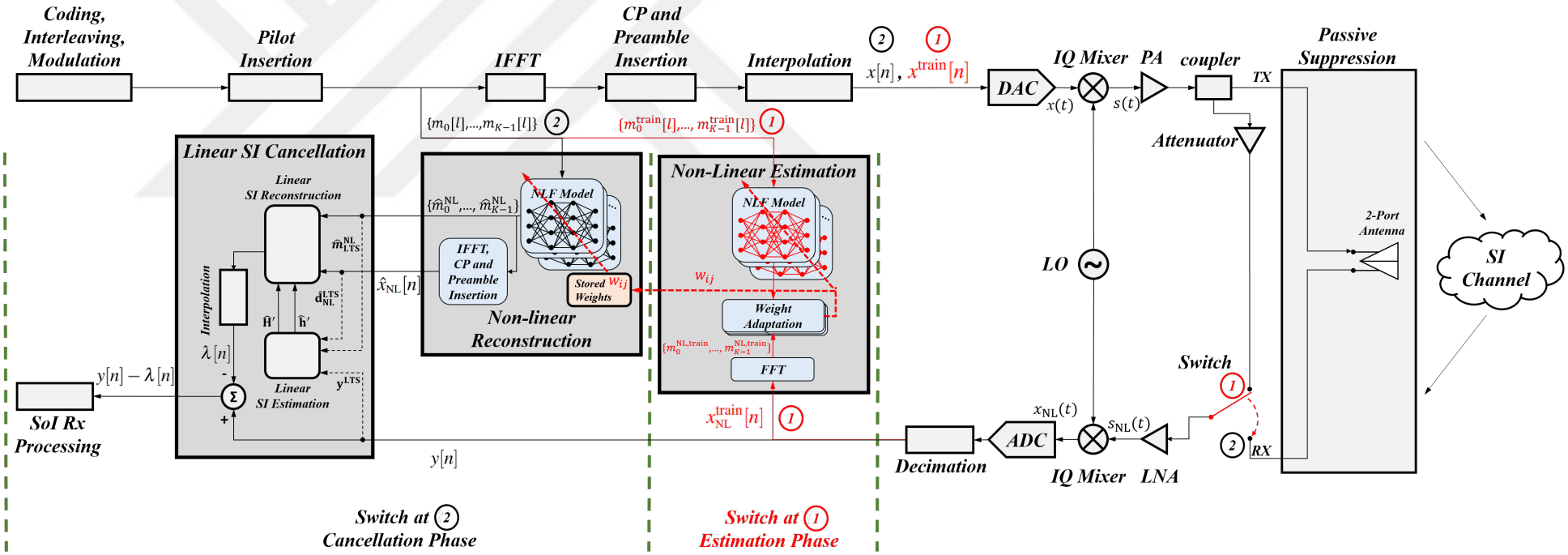

Figure 4.4 Implementation of proposed NLF estimation in IBFD-SW radio arcitecture

4.3 Performance Tests

In this section, the total SI suppression performance of the proposed non-linear SI cancellation and existing non-linear methods are investigated on the same SDR set-up for varying transmit power levels (within the limits of the SDR in the set-up) and under varying multi-path spread (for the first time in literature). The amount of total SI suppression is calculated as the ratio of the received SI signal power to the power of the residual SI signal and it is presented in dB scale. We evaluate and compare the total SI suppression performance of: 1) Proposed IBFD-SW radio with NLF estimation and four linear SI cancellation techniques (TE-TR, TE-FR, FE-TR, FE-FR [3]) 2) Proposed IBFD-SW radio with NLP estimation and four linear SI cancellation techniques 3) Proposed IBFD-SW radio with NLC estimation and all linear techniques 4) IBFD-AUX radio [2] with all linear techniques 5) IBFD radio with integrated nested MP and TE-TR [5] 6) IBFD radio with integrated residual MP and TE-TR [5] 7) IBFD radio with non-linear only MP [4] 8) IBFD radio with linear only SI cancellation employing one of the four techniques [3]. In all presented results for the algorithms, we have applied the optimal values of the model parameters at each transmit power level, which are determined as explained in Appendix B and [5].

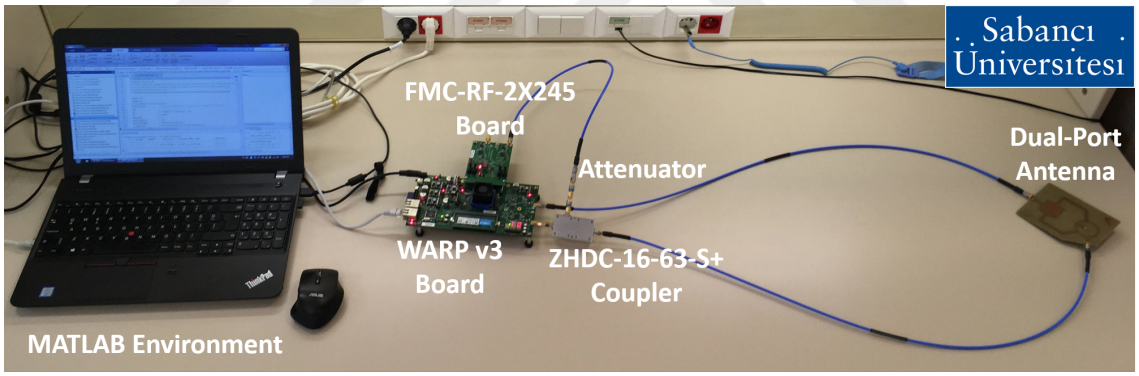

Figure 4.5 IBFD radio set-up

Our OFDM based IBFD radio set-up with a dual port antenna [57] and WARP v3 SDR [6] supporting IEEE 802.11a/g physical layer standard is depicted in Fig. 4.5, where the non-linear SI estimation/reconstruction and linear SI cancellation algorithms are implemented in MATLAB on the laptop computer. A list of key parameters for the set-up is presented in Table 4.1. For the IBFD-SW radio architecture, for realizing the loop back, WARP v3 SDR is integrated with the FMC-RF-2X245 transceiver board [58] together with Minicircuits ZHDC-16-63-S+ directional coupler [59] and a 55 dB attenuator. The non-linear SI estimation (NLF, NLP, NLC) and linear SI cancellation (TE-TR, TE-FR, FE-TR, FE-FR [3]) algorithms are implemented in MATLAB environment on the computer as follows: The transmit

Table 4.1 Parameters For NN Model and For IBFD-SW SDR Set-Up Based on IEEE 802.11g

Number of Hidden Layers	2
Number of Neurons in Each Hidden Layer	5
Hidden Layer Activation Function	*tansig*
Training Algorithm	Levenberg-Marquardt
Performance Measure	Mean Square Error (MSE)
Communication Bandwidth	20 MHz
Center Frequency	2.412 GHz
Sampling Rate	40 MHz
Passive Suppression	73 dB
Coupler Performance	16 dB
Attenuator	55 dB
Noise Floor	-85 dBm
Power Amplifier Gain	30 dB
Transmit Power Range	-7 dBm to 21 dBm
Number of sub-carriers	64
Number of CP samples	16
Number of payload (or LTS) sub-carriers	48
Number of pilot sub-carriers	4
Number of guard sub-carriers	11
Number of inserted sub-carrier for CPNR	8
Roll-off factor	0.93
Modulation	16-QAM

waveform generated in the MATLAB environment is delivered to the SDR board via the Ethernet connection, it is transmitted to the air by means of the antenna and it is delivered to the the FMC-RF-2X245[1] receiver board through the coupler. In the reverse direction, via the Ethernet connection, the receive waveform arriving to the receiver chains are transferred to the MATLAB environment on the computer. The non-linear SI estimation phase of the IBFD-SW radio is employed in MATLAB on the samples received from the FMC-RF-2X245 receiver board and the cancellation phase is performed over the signal arriving from the ordinary receive chain on the WARP v3 board. Switching between estimation and cancellation phases is also implemented in MATLAB.

IBFD radio with auxiliary receive chain (IBFD-AUX) in [2] is realized on our WARP v3 SDR board by employing the FMC-RF-2X245 receiver board. Integrated nested MP and residual MP [5] schemes, and non-linear only MP [4] are implemented along with linear cancellation, TE-TR, all in MATLAB, on the WARP v3 SDR set-up without the FMC-RF-2X245 receiver board, where the estimation and reconstruction are performed over the signal arriving from the ordinary receive chain. Note that, in all experiments, we consider a single radio, as we measure total SI cancellation capability; hence there is no SoI from another radio. The provided re-

[1]Note that, on WARP v3 set-up used in the experiments, the same local oscillator (LO) clock signal is shared between the RF transceiver chains and FMC-RF-2X245 boards.

sults are obtained as the average of 100 experiments, in each experiment an OFDM packet includes 700 OFDM symbols resulting 56000 samples.

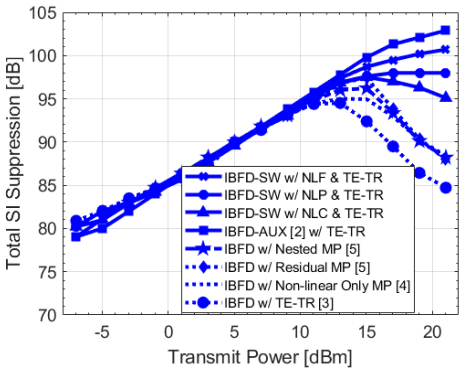

(a) Linear cancellation using TE-TR

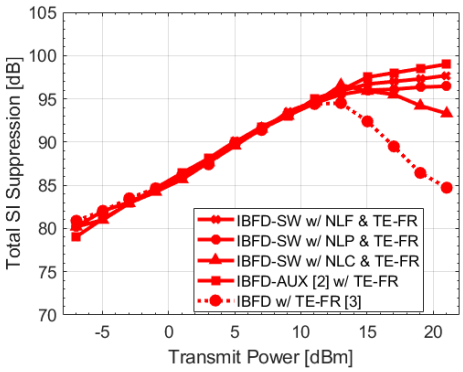

(b) Linear cancellation using TE-FR

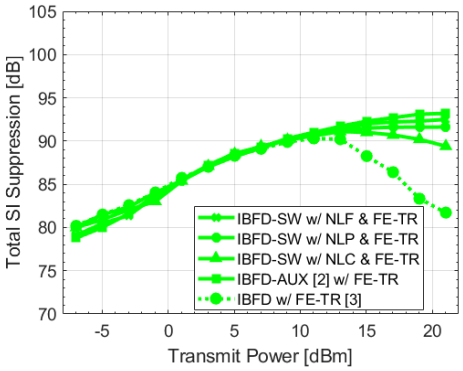

(c) Linear cancellation using FE-TR

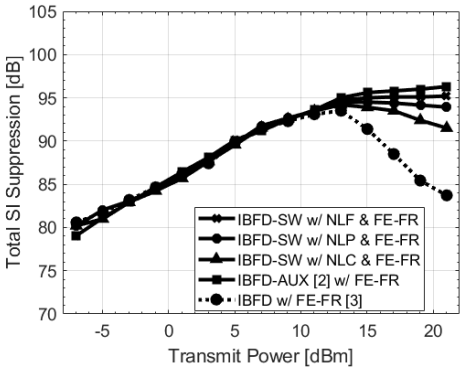

(d) Linear cancellation using FE-FR

Figure 4.6 Total SI suppression performance of proposed, IBFD-SW radio w/ NLF, NLP, NLC and linear cancellation algorithms versus existing solutions, IBFD-AUX [2] w/ linear cancellation and IBFD radio w/ linear [3], non-linear only [4] and integrated linear and non-linear cancellation [5]

In the laboratory experiments, in Fig. 4.6 (a), our IBFD-SW architecture with NLF and TE-TR outperforms IBFD with TE-TR (linear only scheme) by up to 16 dB and improves IBFD with existing digital non-linear cancellation schemes, IBFD with nested MP [5], residual MP [5] and non-linear only MP [4], by up to 13 dB. It can be seen that, for the simplest IBFD radio, with TE-TR (linear only cancellation) maximum total SI suppression is measured as 94 dB, which degrades for power levels above 13 dBm due to non-linearity. Although, nested MP, residual MP and non-linear only MP provide 3-4 dB improvement over linear only scheme, their performance degrades for higher power levels since non-linear and linear cancellation schemes are integrated. However, in our proposed IBFD-SW radio architecture, since the non-linear and linear effects are perfectly decoupled, the performance of cancellation is improved.

As shown in Fig. 4.6 (a), total SI suppression reaches 103 dB for the IBFD-AUX architecture with TE-TR, where the SI signal is suppressed to the noise level at all transmit power levels, as verified in Appendix C. The maximum total SI suppression for IBFD-SW with NLF and TE-TR is obtained as 101 dB at 21 dBm transmit power level which is the highest transmit power level of the WARP v3 board in our set-up. The small difference between IBFD-AUX and IBFD-SW with NLF is due to the fact that, in IBFD-SW with NLF, the non-linear reference SI signal is estimated digitally, while an anolog reference SI is provided by the extra chain (causing hardware cost) in IBFD-AUX solution. Moreover, IBFD-SW with NLF and TE-TR outperforms IBFD-SW with NLP and TE-TR by up to 3 dB due to frequency-domain non-linear estimation employed on a subcarrier basis. NLP with TE-TR is 3 dB superior to NLC with TE-TR, which is still up to 7 dB higher than existing non-linear cancellation algoritms, IBFD with nested MP [5], residual MP [5] and non-linear only MP [4]. The difference between NLP and NLC algorithms is due to the fact that, NLP results in more accurate non-linear estimation: Separate phase estimation in NLP considers all (odd and even) ordered terms, while complex estimation in NLC considers only odd ordered terms.

In Fig. 4.6 (b), (c), and (d), the total SI suppression is measured for the three alternative linear SI cancellation schemes, TE-FR, FE-TR and FE-FR, on the same radio in part (a), excluding IBFD with nested MP, residual MP and non-linear only MP, which can only work with TE-TR. All linear SI cancellation techniques with the proposed non-linear estimation algorithms employed on IBFD-SW radio are shown to perform closely to IBFD-AUX radio, outperforming IBFD radio with linear only techniques by (up to) 12 dB. At high transmit power levels, some degradation is observed in respective radios when linear cancellation employs TE-FR, FE-TR and FE-FR as compared to the results with TE-TR in Fig. 4.6 (a). This is because, estimation and reconstruction domains are changed via FFT/IFFT operations in those schemes, where the sizes of FFT/IFFT are taken as the length of the transmit symbol (K=64) for lower complexity [27], rather than applying circular convolution with larger FFT/IFFT sizes, as earlier addressed in [3]. Linear SI cancellation techniques involving FE provide higher multi-path resiliency as compared to the ones employing TE [3].

Next, we observe the effect of multi-path on the IBFD radios and non-linear cancellation solutions by applying a multi-path SI channel emulator on the received baseband samples in our set-up. The emulated multi-path SI channel can be characterized as a tapped-delay-line (TDL) model with the low-pass impulse response, $h(t) = \sum_{q=0}^{Q_{\max}\text{-}1} \alpha_q(t)\delta(t-\tau_q)$, where τ_q is the tap delay, $Q_{\max}$ is the maximum number

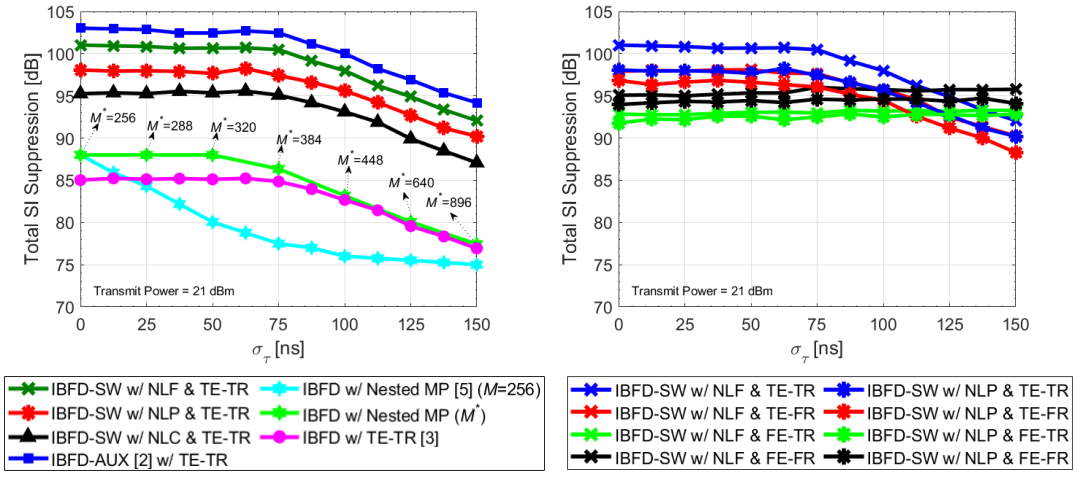

(a) (b)

Figure 4.7 Comparison of total SI suppression performance at 21 dBm transmit power (a) for time-domain linear cancellation technique (TE-TR) by employing different IBFD radios and non-linear models (b) for different linear cancellation techniques (TE-TR, TE-FR, FE-TR, FE-FR) on the proposed IBFD-SW radio with various non-linear models

of paths, α_q is the complex channel coefficient of path q [60]. The TDL model is used with the IEEE 802.11 indoor channel model [49] for generating the power delay profile (PDP) for $\alpha_q(t)$. The channel power decreases exponentially with delayed taps as $A(q) = \frac{1}{\sigma_\tau} \exp^{-qT_s/\sigma_\tau}$, $q = 0, 1, 2, ..., Q_{max}$, where σ_τ is the rms delay spread, and T_s is the sampling time. The maximum excess delay is set to 10 times the rms delay spread in [49], so the maximum number of paths is calculated by means of σ_τ and T_s as $Q_{max} = [10\sigma_\tau/T_s]$.

In Fig. 4.7 (a), we compare the total SI suppression performance of the considered IBFD radios with different non-linear solutions and TE-TR at 21 dBm transmit power level and varying σ_τ employed through the multi-path SI channel emulator defined by the TDL model. As σ_τ is increased above 75 ns, the performance of the IBFD-SW and IBFD-AUX radios as well as IBFD radio with TE-TR (linear only) is degraded, in a similar (parallel) manner. This is because, in IBFD-AUX and IBFD-SW, non-linear SI cancellation is completely isolated from the SI channel, hence the performance under multi-path is determined by linear cancellation alone. On the other hand, the performance of IBFD with nested MP utilizing the model parameters optimized for the laboratory environment ($L = 10000$, $M = 256$, $P = 5$) degrades immediately as σ_τ is increased. This degradation is due to the close adherence between non-linear and linear SI cancellation stages, and the fact that the memory of non-linear SI model should be increased with increasing multi-path delay. For a fair evaluation of the IBFD with nested MP, we have re-optimized the MP model parameters considering the multi-path channel at each σ_τ value and we

have observed that the optimum memory length (M^*) grows with σ_τ. With the updated optimized memory, the total SI suppression performance of IBFD nested MP, follows a similar behavior as IBFD-SW, IBFD-AUX and IBFD with TE-TR, performing only 3 dB above the performance of IBFD with TE-TR for σ_τ values less than 75 ns. For larger σ_τ values, IBFD with nested MP cannot provide any improvement over the linear only scheme in IBFD TE-TR. We observe that IBFD-SW and IBFD-AUX radios provide significant improvements over both linear only and nested MP (with optimized memory settings): Under severe multi-path, IBFD-SW with NLF outperforms both schemes by up to 15 dB, while improvement by IBFD-AUX is up to 17 dB.

In the tests depicted in Fig. 4.7 (b), we observe the behaviour of IBFD-SW with linear SI cancellation algorithms, TE-TR, TE-FR, FR-TR, and FE-FR, under multi-path channel environment by employing the same emulator. It can be seen that for IBFD-SW with NLF and with NLP, the total SI suppression performance is not affected for FE-FR and FE-TR techniques, while it degrades for TE-FR and TE-TR after 75 ns. As an example, as depicted in Fig. 4.7 (b), for $\sigma_\tau = 150$ ns, the performance of IBFD-SW with NLF and with NLP using FE is around 3-5 dB above that of the same techniques utilizing TE. This is because of better linear channel estimation in FE as compared to TE, as discussed earlier in [3].

The findings that we noted above for the experiment results under multi-path SI channel conditions are valid for all high transmit power levels from 13 dBm to 21 dBm as depicted in Fig. 4.8. In Fig. 4.8 (a), we compare the total SI suppression performance of the considered IBFD radio architectures with different non-linear solutions and TE-TR as the linear SI cancellation, for high transmit power levels from 13 dBm to 21 dBm and varying σ_τ from 0 ns to 150 ns. For σ_τ values smaller than 75 ns, the IBFD radio with TE-TR (linear only) as well as IBFD-AUX and IBFD-SW architectures are not affected from multi-path for the given transmit power levels. As σ_τ is increased above 75 ns, the performance of all architectures is degraded as the performance of TE degrades. On the other hand, the performance of IBFD with nested MP without updated model parameters degrades immediately as σ_τ is increased for the given transmit power levels. When the memory parameter of IBFD with nested MP is updated for each σ_τ, the total SI suppression performance of IBFD with nested MP follows a similar behavior as IBFD-AUX, IBFD-SW and IBFD with TE-TR. As it is shown in Fig. 4.8 (b), for IBFD-SW with NLF, the total SI suppression performance is not affected for FE-FR and FE-TR techniques for high transmit power levels from 13 dBm to 21 dBm as σ_τ is increased, while it degrades for TE-FR and TE-TR after $\sigma_\tau = 75$ ns. This is due to the fact that, in FE, better linear channel estimation is obtained as compared to TE.

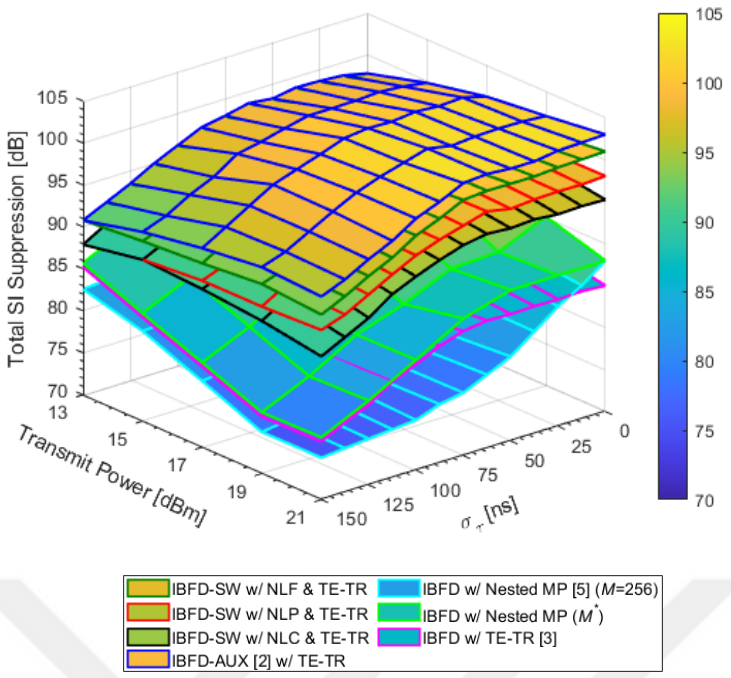

(a)

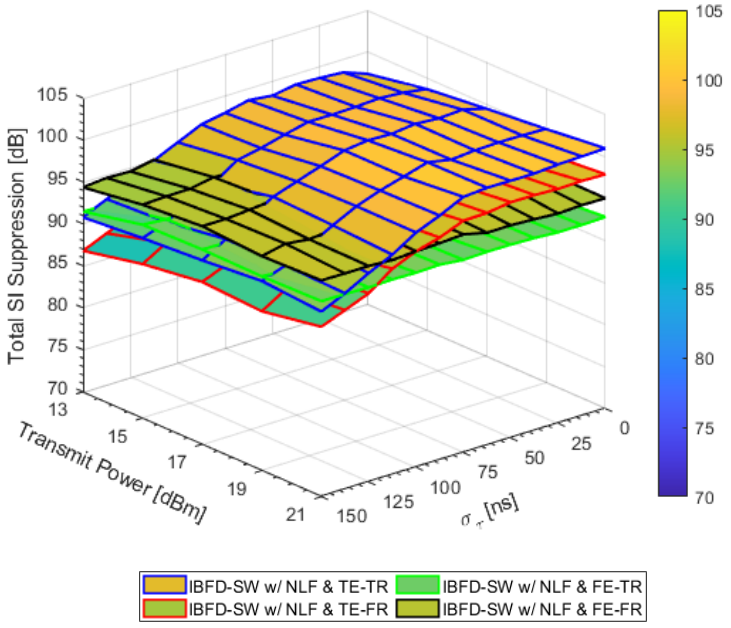

(b)

Figure 4.8 Comparison of total SI suppression performance with respect to high transmit power levels and *rms* delay spread (a) for time-domain linear cancellation technique (TE-TR) by employing different IBFD radios and non-linear models (b) for different linear cancellation techniques (TE-TR, TE-FR, FE-TR, FE-FR) on the proposed IBFD-SW radio with NLF model

4.4 Overhead and Complexity Analysis

4.4.1 Estimation Overhead

The estimation (training) overhead corresponds to the number of samples transmitted in half-duplex mode for the estimation phase of non-linear and linear SI cancellation. Full-duplex operation is enabled after the completion of estimation phase to perform the SI cancellation. Since linear estimation is conducted on the LTS for TE-TR, TE-FR, FE-TR and FE-FR, the training overhead of the linear SI cancellation stage is confined to the preamble length [1]. For non-linear cancellation the estimation (or training) overhead depends on the employed solution.

For the proposed IBFD-SW radio, the optimal estimation (training) length for NLF is found as 2400 samples, and it is 1600 samples for NLP and NLC as shown in Appendix B. Thanks to the isolation of non-linear and linear effects in our IBFD-SW radio architecture, training of the non-linear model needs to be done only once, at power-up, and the learned coefficients can be stored and re-used for subsequent transmissions, irrespective of the changes in multi-path as shown in the performance section. Our experiments with continuous transmission for 30 hours proves that non-linear model is not likely to change much, as shown in Appendix B. Therefore, the estimation (training) overhead for the proposed algorithms employed on our IBFD-SW radio architecture is almost zero.

The estimation overhead for nested MP, residual MP and non-linear only MP have been found as 10000 samples in [5], all obtained and optimized on the same set-up. It is worthwhile to note that, the nested MP scheme is highly sensitive to changes in the multi-path environment, as it can be seen in Fig. 4.7. The memory length of the MP model must be adjusted according to the channel's multi-path spread, and the training needs to be repeated for the non-linear model with the new channel; hence, the estimation is to be repeated each time the radio changes its environment, increasing the overhead.

4.4.2 Computational Complexity

In this section, we analyze the asymptotic computational complexity of the proposed non-linear/linear SI cancellation algorithms in terms of required run-time multiply-and-accumulate (MAC) operations and compare with the existing schemes. For all algorithms, we consider a total of N samples. L and $Q = N - L$ are the number of samples used in the non-linear estimation and reconstruction phases, respectively. K is the number of LTS samples used for linear SI channel estimation and K_{CP} is the number of samples in CP. R is the number of neurons in each hidden layer employed in NLF. Also, M is the memory length in nested MP, and finally, P is the polynomial order in the non-linear models.

For NLF, the computational complexity for non-linear estimation is $O(K((L - (L/(K + K_{CP}))K_{CP})\ (K \log K + 4(R^2 + R))))$ including frequency-domain conversion, weight adaptation and matrix multiplications, and for reconstruction, $O(K((Q - (Q/(K + K_{CP}))K_{CP})(K \log K + 2(R^2 + R))))$ computation is required. For NLP, the total computational complexity of the estimation phase is obtained as $O(3L(P+1)+(L+1)(3P^2+6P+2)/2+(3P^3+9P^2+9P+3)/2+160L)$, accounting for transposing, cross-correlation, inversion and multiplication of matrices as well as the calculation of magnitude and phase of each complex sample. Similarly, the complexity of reconstruction phase in NLP is around $O(3Q(P+1)/2+160Q)$. Meanwhile, for the estimation phase of NLC, the computational complexity is around $O(P^3+P^2L)$, representing the matrix inversion and matrix multiplications; whereas matrix multiplication of the coefficients for linear SI reconstruction requires $O(PQ)$ computations. For nested MP, residual MP and non-linear only MP, the computational complexity for estimation and reconstruction phases has been obtained as $O((MP)^3 + (MP)^2L)$ and $O(MPQ)$, respectively in [5].

Regarding the linear SI cancellation techniques, the computational complexity of the TE-TR technique is calculated as $O(K^2)$, accounting for multiplication operation for estimating the linear SI channel and $O(Q \log Q)$ for reconstruction via convolution operation. In TE-FR, the term for linear SI channel estimation becomes $O(K^2 + K \log K)$, where FFT operation for domain conversion is added, and reconstruction requires $O(2((Q - (Q/(K + K_{CP}))K_{CP})/K)(K \log K))$ computations. Meanwhile, FE-TR consumes $O(K + 2K \log K)$ and $O(Q \log Q)$ computations in the estimation and reconstruction phases, respectively. On the other hand, in FE-FR, while $O(K + K \log K)$ computations are required for estimation phase, $O(2((Q-(Q/(K+K_{CP}))K_{CP})/K)(K \log K + K))$ operations are used in the reconstruction phase.

In Table 4.2, we provide simplified complexities by considering only the dominating terms in the obtained complexity expressions, along with numerical values for the non-simplified complexities, considering all non-linear and linear schemes. As shown in Table 4.2, in addition to superior performance, for the estimation phase, NLF has four orders of magnitude smaller complexity as compared to nested MP scheme; whereas, for the reconstruction phase, the difference is an order of magnitude. Although, NLP and NLC have an order of magnitude lower complexity as compared to NLF, their performance is at least 3 dB below the performance of NLF. NLC has the lowest estimation complexity among all considered solutions which is six orders of magnitude lower than that of nested MP scheme. For linear SI estimation, FE techniques have two orders of magnitude smaller complexity as compared to the TE techniques.

Table 4.2 Computational Complexity of the Non-linear/Linear SI Cancellation Schemes

Technique		**Simplified Complexity**			**Numerical Values***			
		Estimation		**Reconstruction**	**Non-linear Estimation**	**Estimation**		**Reconstruction**
Non-linear	**Linear**	**Non-linear**	**Linear**	**Non-linear+Linear**	**Overhead** (L)	**Non-linear**	**Linear**	**Non-linear+Linear**
NLF	TE-TR	$O(L(K^2\log K+KR^2))$	$O(K^2)$	$O(QKR^2+Q\log Q)$	2400**	2.81×10^6	1.23×10^4	3.47×10^7
NLF	TE-FR	$O(L(K^2\log K+KR^2))$	$O(K^2)$	$O(QKR^2+Q\log K)$	2400**	2.81×10^6	1.26×10^4	3.46×10^7
NLF	FE-TR	$O(L(K^2\log K+KR^2))$	$O(K\log K)$	$O(QKR^2+Q\log Q)$	2400**	2.81×10^6	8.86×10^2	3.47×10^7
NLF	FE-FR	$O(L(K^2\log K+KR^2))$	$O(K\log K)$	$O(QKR^2+Q\log K)$	2400**	2.81×10^6	5.39×10^2	3.46×10^7
NLP	TE-TR	$O(L)$	$O(K^2)$	$O(Q\log Q)$	1600**	3.57×10^5	1.23×10^4	9.97×10^6
NLP	TE-FR	$O(L)$	$O(K^2)$	$O(Q\log K)$	1600**	3.57×10^5	1.26×10^4	9.93×10^6
NLP	FE-TR	$O(L)$	$O(K\log K)$	$O(Q\log Q)$	1600**	3.57×10^5	8.86×10^2	9.97×10^6
NLP	FE-FR	$O(L)$	$O(K\log K)$	$O(Q\log K)$	1600**	3.57×10^5	5.39×10^2	9.93×10^6
NLC	TE-TR	$O(P^3+P^2L)$	$O(K^2)$	$O(PQ+Q\log Q)$	1600**	4.33×10^4	1.23×10^4	1.26×10^6
NLC	TE-FR	$O(P^3+P^2L)$	$O(K^2)$	$O(PQ+Q\log K)$	1600**	4.33×10^4	1.26×10^4	1.22×10^6
NLC	FE-TR	$O(P^3+P^2L)$	$O(K\log K)$	$O(PQ+Q\log Q)$	1600**	4.33×10^4	8.86×10^2	1.26×10^6
NLC	FE-FR	$O(P^3+P^2L)$	$O(K\log K)$	$O(PQ+Q\log K)$	1600**	4.33×10^4	5.39×10^2	1.22×10^6
Nested MP [5]	TE-TR	$O((MP)^3+(MP)^2L)$	$O(K^2)$	$O(MPQ)$	10000	1.90×10^{10}	1.23×10^4	1.10×10^8
Residual MP [5]	TE-TR	$O((MP)^3+(MP)^2L)$	$O(K^2)$	$O(MPQ)$	10000	1.50×10^{11}	1.23×10^4	4.20×10^8
Non-linear MP [4]	TE-TR	$O((MP)^3+(MP)^2L)$	$O(K^2)$	$O(MPQ)$	10000	1.50×10^{11}	1.23×10^4	4.20×10^8

* These numerical values are based on non-simplified complexities. The total number of samples used in the calculations is $N=56000$. L samples are used for non-linear estimation and $Q=N-L$ samples are used for non-linear reconstruction. $P=5$ is the polynomial order in the non-linear models and $M=256$ is the memory length. For NLF, $R=5$ is the number of neurons in each hidden layer. For linear cancellation, $K=64$ LTS samples are used for linear SI channel estimation. All of these parameters have been found as optimal values for each scheme on our IBFD/IBFD-SW set-up. All numerical values are represented in terms of the number of real MAC operations to ensure fair comparisons. Note that, multiplying two complex numbers involves three real multiplications.

** This overhead is to be accounted for only once, at power-up.

5. CONCLUSIONS

In this thesis, we study linear digital self-interference (SI) cancellation (DSIC) techniques and non-linearity problem induced by the hardware components on the In-Band Full-Duplex (IBFD) radios employing Orthogonal Frequency Division Multiplexing (OFDM).

In the first part of this thesis, we have proposed a solution named Cyclic Prefix (CP) Noise Reduction (CPNR) for improving DSIC in OFDM based IBFD radios, to eliminate the CP noise on the residual SI signal. In order to evaluate the performance of DSIC with CPNR, we have performed detailed baseband simulations as well as labortory tests on our IBFD radio SDR platform, considering multi-path and time-varying effects on the SI channel through a channel emulator.

We have observed that the performance improvement obtained by CPNR depends on employed DSIC scheme, channel Signal-to-Noise Ratio (SNR) and multi-path conditions: In the open laboratory environment, under low multi-path, by applying CPNR, the total SI cancellation performance of our OFDM based IBFD radio is improved by up to 6 dB for frequency-domain DSIC, approaching the performance of time-domain DSIC. Also, for frequency-domain DSIC, Error Vector Magnitude (EVM) performance for bidirectional communication is improved by 5%. The performance of time-domain DSIC degrades as multi-path becomes severe, while the performance of frequency-domain DSIC is preserved. For instance, for $\sigma_\tau = 150$ ns, highest CPNR enhancement of 13 dB is observed for frequency-domain DSIC. Having implemented frequency-domain DSIC with CPNR on the Field Programmable Logic Array (FPGA) of the Software Defined Radio (SDR) board, we demonstrate that the test results for total SI suppression and EVM with the FPGA implementation are inline with the test results on the SDR based IBFD radio set up. We conclude that CPNR is crucial for not only providing significant improvements in total cancellation performance of the IBFD radio, but also for allowing IBFD communication in practical, realistic, asynchronous scenarios.

In the second part of this thesis, a new switched IBFD radio architecture (IBFD-SW) decoupling the non-linear and linear SI cancellation is proposed along with time-

domain polar non-linear (NLP) estimation and non-linear frequency-domain (NLF) estimation algorithms. The proposed solutions are evaluated on the WARP v3 SDR set-up measuring total SI suppression performance in the laboratory environment as well as with a multi-path SI channel emulator. It is shown that the IBFD-SW radio with NLF outperforms existing digital non-linear SI cancellation techniques by up to 13 dB. The IBFD-SW radio implemented on our SDR set-up along with the non-linear estimation algorithms is capable of suppressing the SI signal to the noise floor of the WARP v3 board; hence, the maximum achievable performance limits are obtained for most transmit power levels. Moreover, the proposed solutions are shown to be robust against changes in multi-path, while the performance of existing solutions degrades with changing multi-path, as the model parameters should be updated according to the channel delay.

Estimation (training) overhead and complexity analysis for the proposed non-linear estimation algorithms are also provided in this thesis. The estimation (training) overhead of the proposed non-linear algorithms is almost zero unlike existing schemes. The computational complexity is reduced further, with estimation complexity decreased by four to six orders of magnitude, and reconstruction complexity reduced by one to two orders of magnitude.

In this thesis, the non-linear SI problem in IBFD radio is alleviated by only a small hardware modification for the switched architecture and by very low complexity algorithms for non-linear estimation. Our solution can be adapted to be applied in OFDM based 4G, 5G systems, as well as emerging 5G+ and 6G technologies, which are envisioned with applications, such as FD backhaul relaying, simultaneous transmission and sensing, and cognitive radio. Our work can also be extended to employ FD in Multiple-Input Multiple-Output (MIMO) and Non-Orthogonal Multiple Access (NOMA) systems.

Bibliography

[1] M. S. Amjad, H. Nawaz, K. Ozsoy, O. Gurbuz, and I. Tekin, "A Low-Complexity Full-Duplex Radio Implementation with a Single Antenna," *IEEE Transactions on Vehicular Technology*, vol. 67, no. 3, pp. 2206–2218, 2018.

[2] M. S. Sim, M. Chung, D. K. Kim, J. Chung, D. K. Kim, and C. B. Chae, "Nonlinear Self-Interference Cancellation for Full-Duplex Radios: From Link-Level and System-Level Performance Perspectives," *IEEE Communications Magazine*, vol. 55, pp. 158–167, jun 2017.

[3] H. Ayar and O. Gurbuz, "Cyclic prefix noise reduction for digital self interference cancellation in ofdm-based in-band full-duplex wireless systems," *IEEE Transactions on Wireless Communications*, vol. 20, no. 9, pp. 6224–6238, 2021.

[4] D. Bharadia, E. McMilin, and S. Katti, "Full duplex radios," *Proceedings of the ACM SIGCOMM 2013 conference on SIGCOMM - SIGCOMM '13*, vol. 43, no. 4, p. 375, 2013.

[5] M. Yilan, O. Gurbuz, and H. Ozkan, "Integrated linear and nonlinear digital cancellation for full duplex communication," *IEEE Wireless Communications*, vol. 28, no. 1, pp. 20–27, 2021.

[6] "WARP Project." http://warpproject.org.

[7] M. Yilan, H. Ayar, H. Nawaz, O. Gurbuz, and I. Tekin, "Monostatic Antenna In-Band Full Duplex Radio: Performance Limits and Characterization," *IEEE Transactions on Vehicular Technology*, pp. 1–1, 2019.

[8] J. Li, H. Zhang, and M. Fan, "Digital Self-Interference Cancellation Based on Independent Component Analysis for Co-Time Co-frequency Full-Duplex Communication Systems," *IEEE Access*, vol. 5, pp. 10222–10231, 2017.

[9] Z. Zhang, X. Chai, K. Long, A. V. Vasilakos, and L. Hanzo, "Full duplex techniques for 5g networks: self-interference cancellation, protocol design, and relay selection," *IEEE Communications Magazine*, vol. 53, no. 5, pp. 128–137, 2015.

[10] Y. Niu, Y. Li, D. Jin, L. Su, and A. V. Vasilakos, "A survey of millimeter wave communications (mmWave) for 5G: opportunities and challenges," *Wireless Networks*, vol. 21, no. 8, 2015.

[11] Z. Zhang, X. Wang, K. Long, A. V. Vasilakos, and L. Hanzo, "Large-scale MIMO-based wireless backhaul in 5G networks," *IEEE Wireless Communications*, vol. 22, no. 5, 2015.

[12] Z. Zhang, K. Long, A. V. Vasilakos, and L. Hanzo, "Full-Duplex Wireless Communications: Challenges, Solutions, and Future Research Directions," *Proceedings of the IEEE*, vol. 104, no. 7, pp. 1369–1409, 2016.

[13] A. C. Cirik, Y. Rong, and Y. Hua, "Achievable Rates of Full-Duplex MIMO Radios in Fast Fading Channels With Imperfect Channel Estimation," *IEEE Transactions on Signal Processing*, vol. 62, pp. 3874–3886, aug 2014.

[14] S. Hong, J. Brand, J. I. Choi, M. Jain, J. Mehlman, S. Katti, and P. Levis, "Applications of self-interference cancellation in 5g and beyond," *IEEE Communications Magazine*, vol. 52, pp. 114–121, February 2014.

[15] Y. Zhao, W. Zhai, J. Zhao, Z. Tinghao, S. Sun, D. Niyato, and K.-Y. Lam, "A comprehensive survey of 6g wireless communications," *arXiv:2101.03889*, 12 2020.

[16] H. Ji, Y. Kim, K. Muhammad, C. Tarver, M. Tonnemacher, T. Kim, J. Oh, B. Yu, G. Xu, and J. Lee, "Extending 5g tdd coverage with xdd: Cross division duplex," *IEEE Access*, vol. 9, pp. 51380–51392, 2021.

[17] C. B. Barneto, S. D. Liyanaarachchi, M. Heino, T. Riihonen, and M. Valkama, "Full duplex radio/radar technology: The enabler for advanced joint communication and sensing," *IEEE Wireless Communications*, vol. 28, no. 1, pp. 82–88, 2021.

[18] E. Ahmed, A. M. Eltawil, and A. Sabharwal, "Self-interference cancellation with nonlinear distortion suppression for full-duplex systems," *Asilomar Conference on Signals, Systems and Computers*, pp. 1199–1203, 2013.

[19] A. Sabharwal, P. Schniter, D. Guo, D. W. Bliss, S. Rangarajan, and R. Wichman, "In-band full-duplex wireless: Challenges and opportunities," *IEEE Journal on Selected Areas in Communications*, vol. 32, no. 9, pp. 1637–1652, 2014.

[20] D. Korpi, J. Tamminen, M. Turunen, T. Huusari, Y.-S. Choi, L. Anttila, S. Talwar, and M. Valkama, "Full-duplex mobile device: Pushing the limits," *IEEE Communications Magazine*, vol. 54, no. 9, pp. 80–87, 2016.

[21] M. Duarte, C. Dick, and A. Sabharwal, "Experiment-driven characterization of full-duplex wireless systems," *IEEE Transactions on Wireless Communications*, vol. 11, no. 12, pp. 4296–4307, 2012.

[22] M. A. Islam, G. C. Alexandropoulos, and B. Smida, "A Unified Beamforming and A/D Self-Interference Cancellation Design for Full Duplex MIMO Radios," in *2019 IEEE 30th Annual International Symposium on Personal, Indoor and Mobile Radio Communications (PIMRC)*, pp. 1–7, 2019.

[23] "Smart Networks in the context of NGI," Strategic Research and Innovation Agenda 2021–27, 2020.

[24] E. Ahmed, A. M. Eltawil, and A. Sabharwal, "Rate gain region and design tradeoffs for full-duplex wireless communications," *IEEE Transactions on Wireless Communications*, vol. 12, no. 7, pp. 3556–3565, 2013.

[25] H. Nawaz and I. Tekin, "Three Dual Polarized 2.4GHz Microstrip Patch Antennas for Active Antenna and In-band Full Duplex Applications," *16th Mediterranean Microwave Symposium (MMS)*, pp. 4–7, 2016.

[26] J. I. Choi, M. Jain, K. Srinivasan, P. Levis, and S. Katti, "Achieving single channel, full duplex wireless communication," *Proceedings of the sixteenth annual international conference on Mobile computing and networking*, p. 1, 2010.

[27] M. S. Amjad and O. Gurbuz, "Linear digital cancellation with reduced computational complexity for full-duplex radios," *IEEE Wireless Communications and Networking Conference, WCNC*, no. 215, 2017.

[28] J. Lee *et al.*, "LTE-advanced in 3GPP Rel -13/14: An evolution toward 5G," *IEEE Communications Magazine*, vol. 54, no. 3, pp. 36–42, 2016.

[29] IEEE, "802.11g - IEEE Standard for Information technology - Local and metropolitan area networks- Specific requirements - Part 11: Wireless LAN Medium Access Control (MAC) and Physical Layer (PHY) Specifications: Further Higher Data Rate Extension in the 2.4 GHz," tech. rep., 2003.

[30] K. Fazel and S. Kaiser, *Multi-Carrier and Spread Spectrum Systems: from OFDM and MC-CDMA to LTE and WiMAX*. Chichester, UK: John Wiley and Sons, Ltd, second ed., oct 2008.

[31] 3GPP TR 38.912, "Study on New Radio (NR) access technology (Release 15)," tech. rep., June 2018.

[32] H. Ayar and O. Gurbuz, "Reducing Cyclic Prefix Noise in OFDM Based Full-Duplex Systems," *Third International Balkan Conference on Communications and Networking Skopje, North Macedonia*, p. 6, June 10-12, 2019.

[33] M. Sakai, H. Lin, and K. Yamashita, "Self-interference cancellation in full-duplex wireless with IQ imbalance," *Physical Communication*, vol. 18, pp. 2–14, 2016.

[34] L. Anttila, D. Korpi, V. Syrjälä, and M. Valkama, "Cancellation of power amplifier induced nonlinear self-interference in full-duplex transceivers," *Conference Record - Asilomar Conference on Signals, Systems and Computers*, pp. 1193–1198, nov 2013.

[35] T. Riihonen and R. Wichman, "Analog and digital self-interference cancellation in full-duplex mimo-ofdm transceivers with limited resolution in a/d conversion," in *2012 Conference Record of the Forty Sixth Asilomar Conference on Signals, Systems and Computers (ASILOMAR)*, pp. 45–49, 2012.

[36] M. Yilan, O. Gurbuz, and H. Ozkan, "Nonlinear digital self-interference cancellation for full duplex communication," *Physical Communication*, 2019.

[37] D. Korpi, Y.-S. S. Choi, T. Huusari, L. Anttila, S. Talwar, and M. Valkama, "Adaptive nonlinear digital self-interference cancellation for mobile inband full-duplex radio: Algorithms and RF measurements," *2015 IEEE Global Communications Conference, GLOBECOM 2015*, pp. 1–7, 12 2015.

[38] M. Emara, K. Roth, L. Gomes Baltar, M. Faerber, and J. Nossek, "Nonlinear digital self-interference cancellation with reduced complexity for full duplex systems," in *WSA 2017; 21th International ITG Workshop on Smart Antennas*, pp. 1–6, 2017.

[39] A. T. Kristensen, A. Burg, and A. Balatsoukas-Stimming, "Advanced machine learning techniques for self-interference cancellation in full-duplex radios," in *2019 53rd Asilomar Conference on Signals, Systems, and Computers*, pp. 1149–1153, 2019.

[40] F. F. Tafuri, C. Guaragnella, M. Fiore, and T. Larsen, "Linearization of rf power amplifiers using an enhanced memory polynomial predistorter," in *NORCHIP 2012*, pp. 1–4, 2012.

[41] D. R. Morgan, Z. Ma, J. Kim, M. G. Zierdt, and J. Pastalan, "A generalized memory polynomial model for digital predistortion of rf power amplifiers," *IEEE Transactions on Signal Processing*, vol. 54, no. 10, pp. 3852–3860, 2006.

[42] J. Kim and K. Konstantinou, "Digital predistortion of wideband signals based on power amplifier model with memory," *Electronics Letters*, vol. 37, no. 23, pp. 1417–1418, 2001.

[43] A. Balatsoukas-Stimming, "Non-linear digital self-interference cancellation for in-band full-duplex radios using neural networks," in *2018 IEEE 19th International Workshop on Signal Processing Advances in Wireless Communications (SPAWC)*, pp. 1–5, 2018.

[44] Y. Kurzo, A. T. Kristensen, A. Burg, and A. Balatsoukas-Stimming, "Hardware implementation of neural self-interference cancellation," *IEEE Journal on Emerging and Selected Topics in Circuits and Systems*, vol. 10, no. 2, pp. 204–216, 2020.

[45] W. Zhang, J. Yin, D. Wu, G. Guo, and Z. Lai, "A self-interference cancellation method based on deep learning for beyond 5g full-duplex system," in *2018 IEEE International Conference on Signal Processing, Communications and Computing (ICSPCC)*, pp. 1–5, 2018.

[46] M. Elsayed, A. A. A. El-Banna, O. A. Dobre, W. Shiu, and P. Wang, "Low complexity neural network structures for self-interference cancellation in full-duplex radio," *IEEE Communications Letters*, vol. 25, no. 1, pp. 181–185, 2021.

[47] O. Gurbuz, I. Tekin, M. Yilan, and H. Ayar, "Low-complexity full-duplex radio system with enhanced digital self-interference cancellation," *United States Patent, US11081798B2*, 3 Aug 2021.

[48] V. Erceg *et al.*, "IEEE P802.11 Wireless LANs TGn Channel Models," *atftp://ieee: wireless@ ftp. 802wirelessworld. com/11/03/11-03-0940-04-000n-tgn-channel-models. doc*, no. May, pp. 1–45, 2004.

[49] N. Chayat, "Tentative criteria for comparison of modulation methods," *Doc. IEEE 802.11-97/96*, 1997.

[50] "WARPLab7 Reference Design, WARP v3 SDR, Mango Board.." http://warpproject.org/trac/wiki/WARPLab.

[51] H. Li *et al.*, "Self-interference cancellation enabling high-throughput short-reach wireless full-duplex communication," *IEEE Transactions on Wireless Communications*, vol. 17, no. 10, pp. 6475–6486, 2018.

[52] Xilinx®, "System Generator for DSP Reference Guide (UG639)," tech. rep., 2012.

[53] MATLAB, *version 8.0.0.783 (R2012b)*. Natick, Massachusetts: The MathWorks® Inc., 2012.

[54] A. A. M. Saleh, "Frequency-independent and frequency-dependent nonlinear models of twt amplifiers," *IEEE Transactions on Communications*, vol. 29, no. 11, pp. 1715–1720, 1981.

[55] Z. El-Khatib, L. MacEachern, and S. A. Mahmoud, "Modulation schemes effect on rf power amplifier nonlinearity and rfpa linearization techniques," in *Distributed CMOS Bidirectional Amplifiers*, pp. 7–28, Springer, 2012.

[56] S. Basterrech, S. Mohammed, G. Rubino, and M. Soliman, "Levenberg—marquardt training algorithms for random neural networks," *The Computer Journal*, vol. 54, no. 1, pp. 125–135, 2011.

[57] H. Nawaz and I. Tekin, "Dual-polarized, differential fed microstrip patch antennas with very high interport isolation for full-duplex communication," *IEEE Transactions on Antennas and Propagation*, vol. 65, no. 12, pp. 7355–7360, 2017.

[58] "FMC-RF-2X245: Dual-Radio FMC Module." https://mangocomm.com/products/modules/fmc-rf-2x245/.

[59] "Minicurcuits ZHDC-16-63-S+ Coaxial, High Directivity, Directional Coupler." https://www.minicircuits.com/pdfs/ZHDC-16-63-S+.pdf.

[60] G. Turin, F. Clapp, T. Johnston, S. Fine, and D. Lavry, "A statistical model of urban multipath propagation," *IEEE Transactions on Vehicular Technology*, vol. 21, pp. 1–9, feb 1972.

[61] "Xilinx." https://www.xilinx.com.

[62] "Mango Communications 802.11 Reference Design." http://mangocomm.com/802.11.

APPENDIX A: FPGA Implementation of Linear Digital SI Cancellation (DSIC) with CPNR

For FPGA implementation, we have chosen FE-TR with CPNR to be realized on the Virtex-6 LS240T FPGA of the WARP v3 SDR board from Mango Communications Inc. [6]. For the implementation, all the functional blocks within DSIC in Fig. 3.8 (i.e., the blocks in yellow with/without red for CPNR) are realized. All computations related to DSIC are performed by the FPGA, while the baseband TX chain and SoI RX processing (i.e., blue boxes in Fig. 3.8) are realized in WARPLab7 MATLAB environment.

WARP v3 FPGA Development Environment

WARP v3 board is designed as a software defined radio (SDR) where wireless communication algorithms are applied as open source codes on WARPLab7 framework as shown in Fig. A.1. By using the WARPLab7 framework, it is possible to realize many applications, algorithms and designs from the upper layer applications to the lowest physical layer algorithms for rapid prototyping.

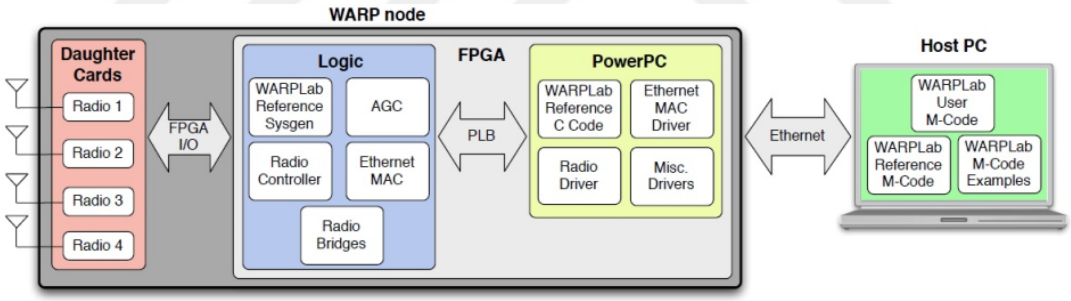

Figure A.1 WARPLab7 framework from Mango Communications Inc. [6]

In Fig. A.1, the Xilinx® FPGA on the WARP v3 board (indicated as WARP node) contains two parts for implementation. The first part is the programmable Logic (PL) part where the hardware of WARPLab7 Reference design, Radio Controller, AGC Controller, interface connections such as RF Interfaces, DDR3 Interface, Ethernet Interface, SD Card Interface, WARPLab7 buffers, etc., are designed as Hardware Description Language (HDL) and embedded; the second part is the Processing PowerPC System (PS) where WARPLab7 Reference C codes and the drivers in C/C++ language for the peripherals are located. PL is connected to PS via PLB bus. Host PC is utilized for running the MATLAB [53] side of the WARPLab7 framework as M-Codes. In MATLAB, the transmit packets are prepared and written into the transmit buffers via Ethernet connection. Transmit packets are sent

to the air via the antennas connected to the RF interface. On the receiving side, the packets received from the air are stored in the receive buffer and transferred to the MATLAB environment through Ethernet connection. Receive processing on the received pakets is performed in M-Code. The complete FPGA configuration for WARPLAB7 Reference Design can be found in Fig. A.2. This configuration is embedded into the FPGA as .bit file which is produced by going through various design and compilation flows using different Xilinx® tools as follows [61]:

- **XSG (Xilinx System Generator) Tool:** Modeling and simulation of the hardware blocks to be embedded in the PL of the FPGA are performed on XSG. This tool uses Simulink tool in MATLAB environment. The development of hardware blocks on Simulink are based on the logic gates library provided by Xilinx. The verified hardware model via simulations is converted to HDL format by means of XSG.
- **XPS (Xilinx Platform Studio) Tool:** The design in HDL format is connected to the PLB bus of PS in the FPGA by using XPS tool. Inter-block connections and appropriate addressing for the memory units are performed by this tool in order to obtain a driver-free bare FPGA hardware. Then, the bare FPGA hardware with PL and PS parts is synthesized for producing an intermediate .bit file.
- **SDK (Software Development Kit) Tool:** The driver software for the support package for the peripheral units on the board (BSP – Board Support Package) is written and compiled on SDK. An .elf file is obtained via the driver software after compilation. The .bit file containing the bare FPGA hardware and the .elf file containing the driver software information are compiled together in order to produce a new .bit file for the board to be embedded in the FPGA.
- **IMPACT Tool:** This tool is used to embed the generated .bit file into FPGA through a JTAG cable.

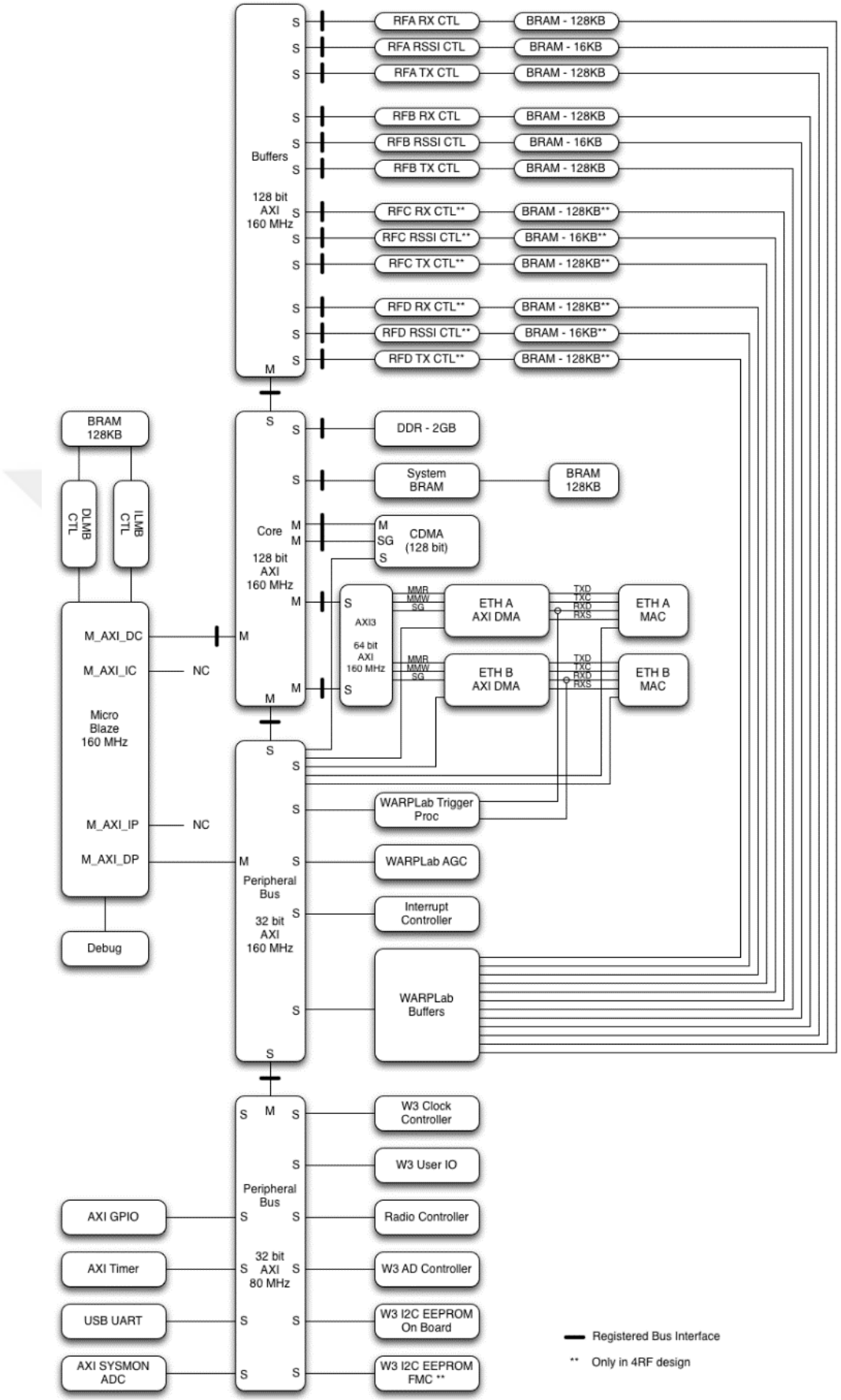

Figure A.2 WARPLab7 FPGA configuration [6]

Details of FPGA Implementation of Linear Digital SI Cancellation (DSIC) with CPNR

FE-TR with CPNR, as shown in Fig. A.3, is realized as an additional hardware module named as si_cancellation to be located inside WARPLab7 Reference design in PL part. While implementing si_cancellation, we re-utilize and modify relevant receiver modules from the 802.11 Reference Design of Mango Communications regarding 802.11g operations [62]. The high level XSG hardware model of si_cancellation module is depicted in Fig. A.4. si_cancellation module is converted into HDL, integrated with WARPLab7 framework, synthesized and embedded into the FPGA by following the steps and utilizing the tools explained in the previous section. Then real-time tests are performed on the board. During the real-time debugging of the implemented blocks, the signals to be observed for debugging purpose are connected to chipscope in the FPGA. Hence, relevant signals are collected from hardware to be compared with MATLAB algorithm.

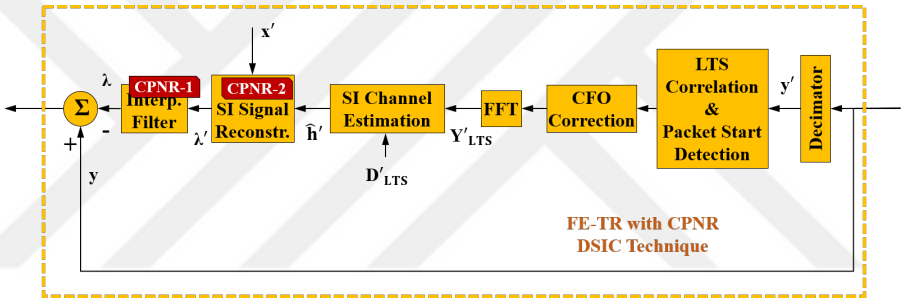

Figure A.3 FE-TR with CPNR DSIC technique in Fig. 3.8 from Section 3.4

The functionality of si_cancellation module is summarized as follows:

- Reading the received signal arriving from ADC and storing it in the RX Buffer
- Decimating the 40 MHz received signal into 20 MHz
- Synchronization:
  - LTS correlation and packet start detection
  - Carrier Frequency Offset (CFO) correction
- Frequency-domain channel estimation (FE)
- Time-domain SI signal reconstruction (TR)
  - Convolution of the generated transmit signal with channel estimation to obtain reconstructed signal
  - Applyin interpolation filter to the reconstructed signal
  - Alignment of the reconstructed and received signals
  - Gain measurement, scaling and subtraction

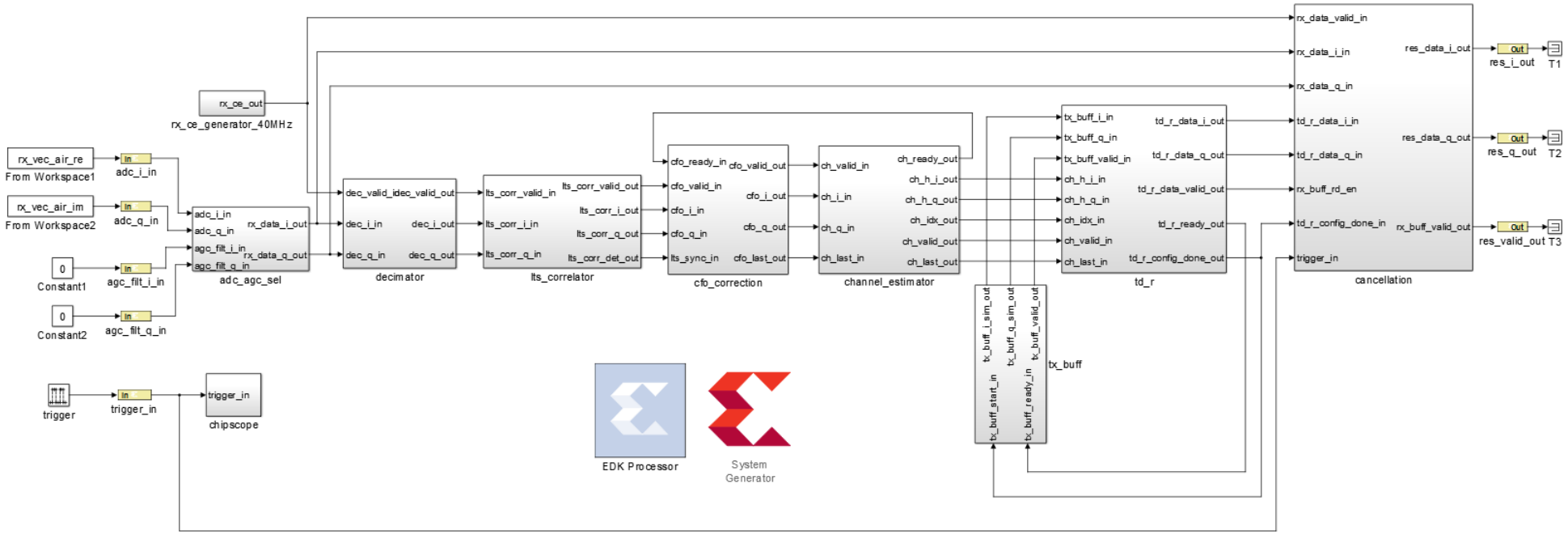

Figure A.4 Xilinx System Generator (XSG) model of the FE-TR with CPNR (si_cancellation module)

Table A.1 describes the input and output signals of si_cancellation module.

Table A.1 Desctipion of Inputs and Outputs for si_cancellation module

Name	Direction	HDL Type	System Generator Type	Description
axi_aresetn	in	std_logic	Bool	Asynchronous reset signal
clk	in	std_logic	Bool	160MHz clock signal
adc_i_in	in	std_logic_vector(11 downto 0)	Fix_12_11	In-phase ADC input signal
adc_q_in	in	std_logic_vector(11 downto 0)	Fix_12_11	Quadrature ADC input signal
agc_filt_i_in	in	std_logic_vector(15 downto 0)	Fix_16_15	In-phase AGC input signal
agc_filt_q_in	in	std_logic_vector(15 downto 0)	Fix_16_15	Quadrature AGC input signal
trigger_in	in	std_logic	Bool	Trigger signal
res_i_out	out	std_logic_vector(15 downto 0)	Fix_16_15	In-phase residual signal
res_q_out	out	std_logic_vector(15 downto 0)	Fix_16_15	Quadrature residual signal
res_valid_out	out	std_logic	Bool	Valid for residual signal

Detailed information about the blocks in si_cancellation module are given in the following.

Decimator

In the decimator block depicted in Fig. A.5, the received SI signal arriving from ADC is down-sampled from 40MHz to 20MHz. For this purpose, an interpolation filter is applied to the received SI signal, represented as in-phase dec_i_in and quadrature dec_q_in input signals, in order to produce dec_i_out and dec_q_out output signals along with an enabler dec_valid_out. Input signals and output signals are formatted as Fix_16_15. In the mean time, these signals are forwarded to "chipscope" with "cs_" prefix for real-time debugging after the design is embedded into the FPGA. Moreover, they are transferred to the MATLAB environment with "mdl_" prefix in order to compare their values with the values obtained from the algorithm in MATLAB environment. Further, the "scope" block from the simulink library is employed for observing the input and output signals prfixed as "ms_" with respect to time samples. Simulation waveform for decimator block is shown in Fig. A.6.

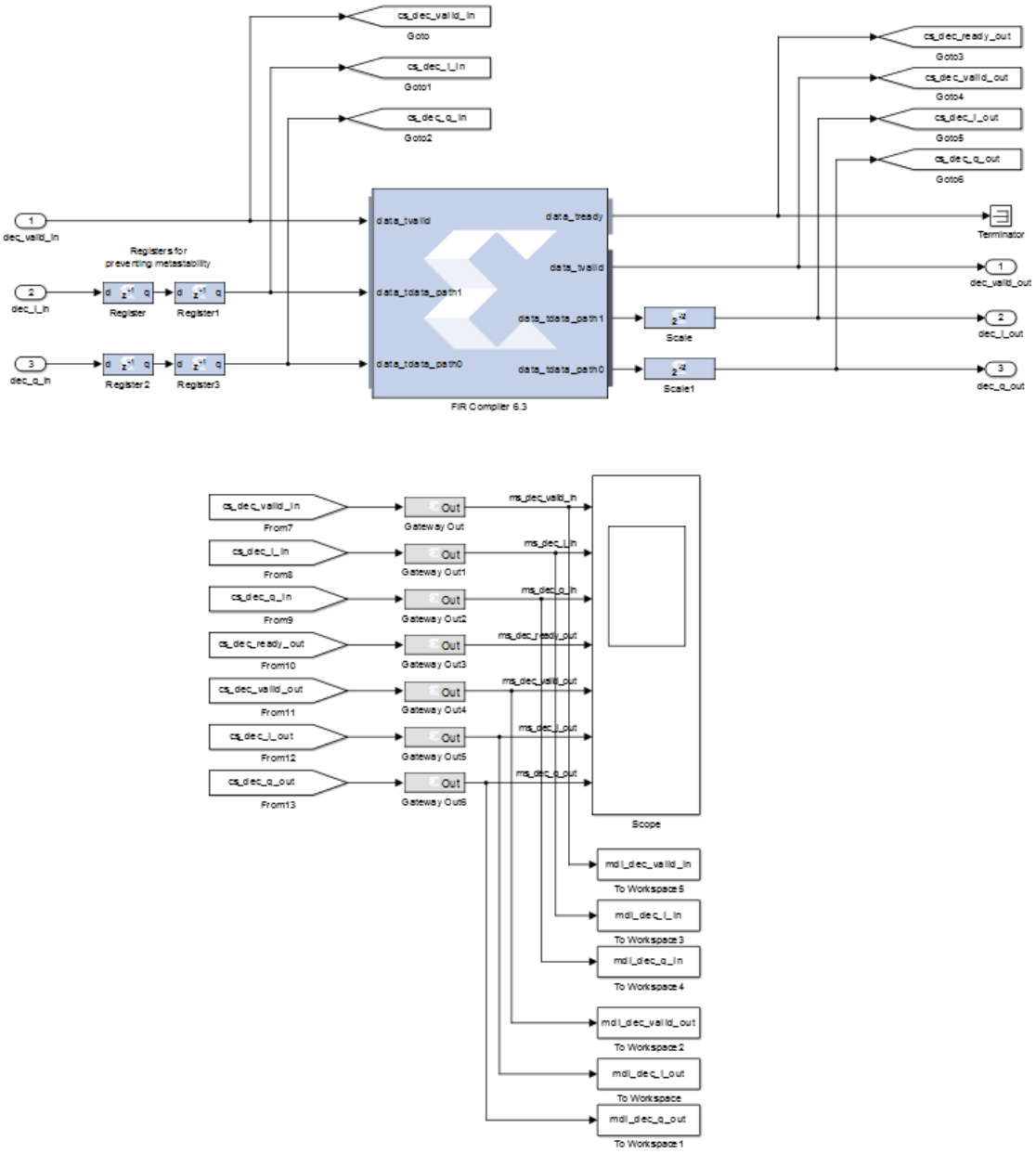

Figure A.5 Decimator block

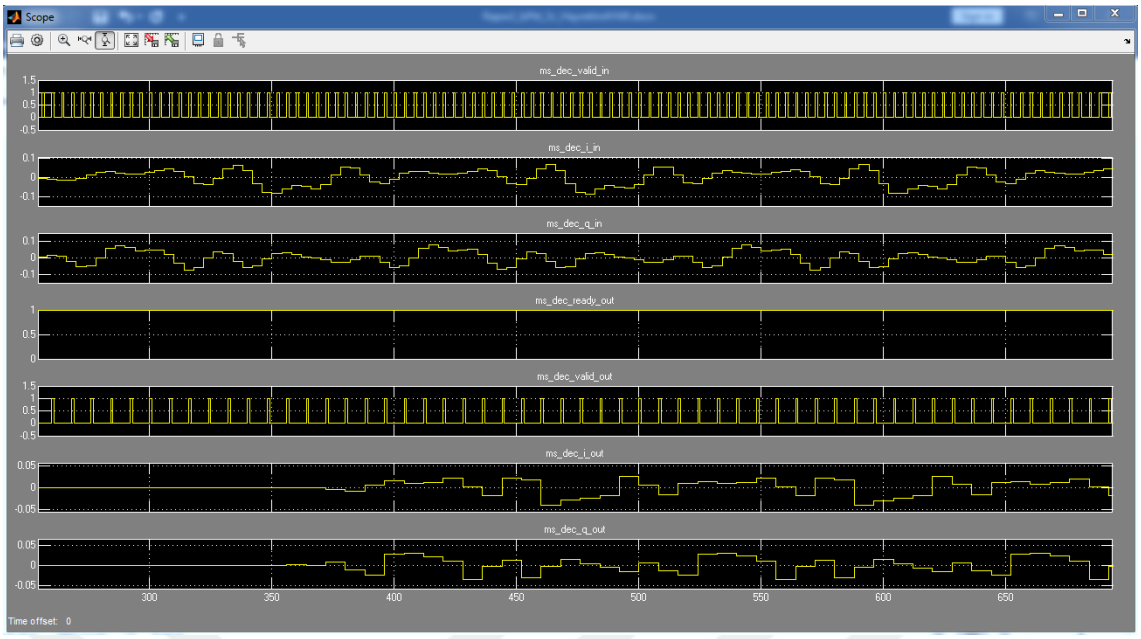

Figure A.6 Simulation of decimator block

LTS Correlator (lts_correlator) Block

In LTS correlator given in Fig. A.7, the decimated in-phase and quadrature signals arriving from decimator are cross-correlated with the known LTS samples stored in a read only memory (ROM) to find the starting point of the received packet. The corr_event_logic sub-block counts four and a half correlation peaks in lts_corr_out and generates the lts_corr_det_out detection signal as a pulse (as shown in Fig. A.8). Again signals are connected to "chipscope" and "scope" with "cs_" and "ms_" prefixes, respectively, and they are transferred to the MATLAB environment with "mdl_" prefix.

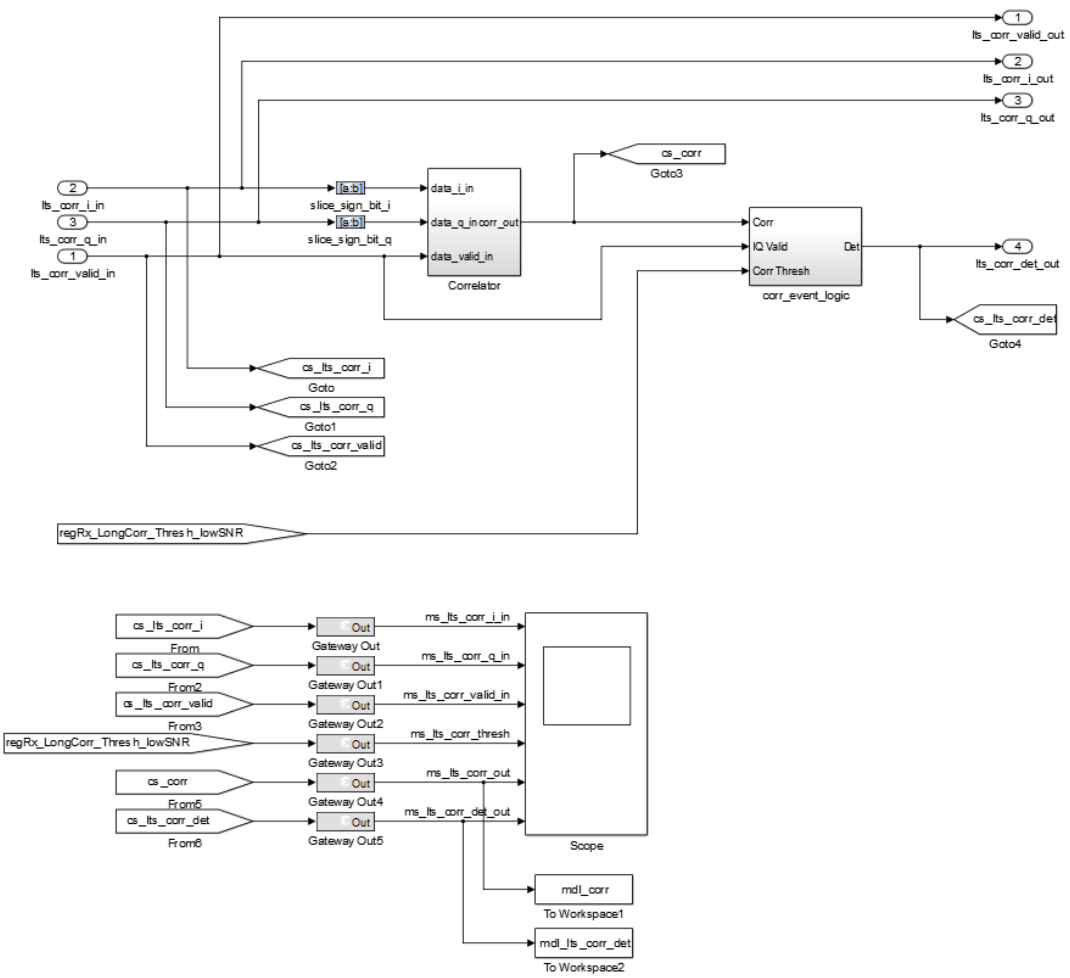

Figure A.7 LTS correlator block [62]

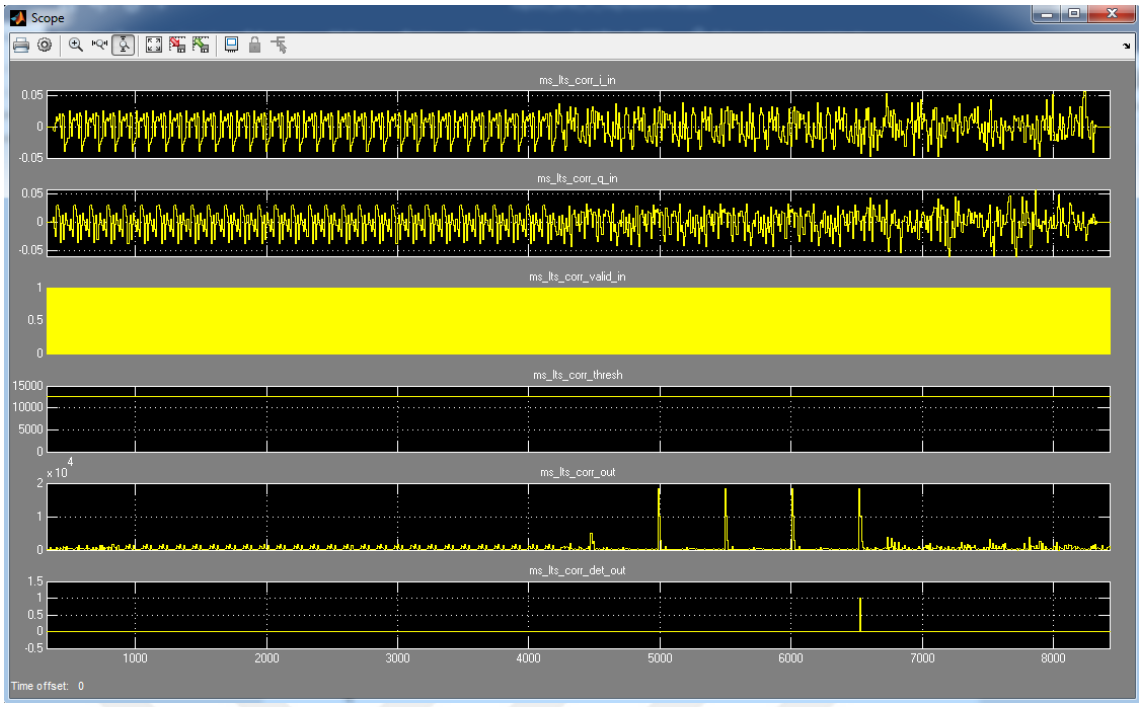

Figure A.8 Simulation of LTS correlator block

Carrier Frequency Offset (CFO) Correction (cfo_correction) Block

While the LTS correlation block described in the previous section operates on the detection of packet start, in CFO correction block, the received samples are stored in the Samp Buffer for cfo correction, as seen in Fig. A.9. The length of this buffer is large enough to store more than four LTS signals, each represented by 64 samples, in order not to dismiss any data sample until CFO Estimation is completed. After the packet start is indicated by lts_sync_in pulse, CFO Estimation sub-block works on the calculation of the carrier frequency offset by utilizing the LTS samples from the Samp Buffer. Then, the obtained carrier frequency offset is corrected on all the received samples. The corrected samples are written into the output First-In First-Out (FIFO) buffer. Again signals are connected to "chipscope" and "scope" with "cs_" and "ms_" prefixes, respectively, and they are transferred to the MATLAB environment with "mdl_" prefix. In Fig. A.10, ms_cfo_i_out and ms_cfo_q_out representing the corrected in-phase and quadrature signals are plotted as an example.

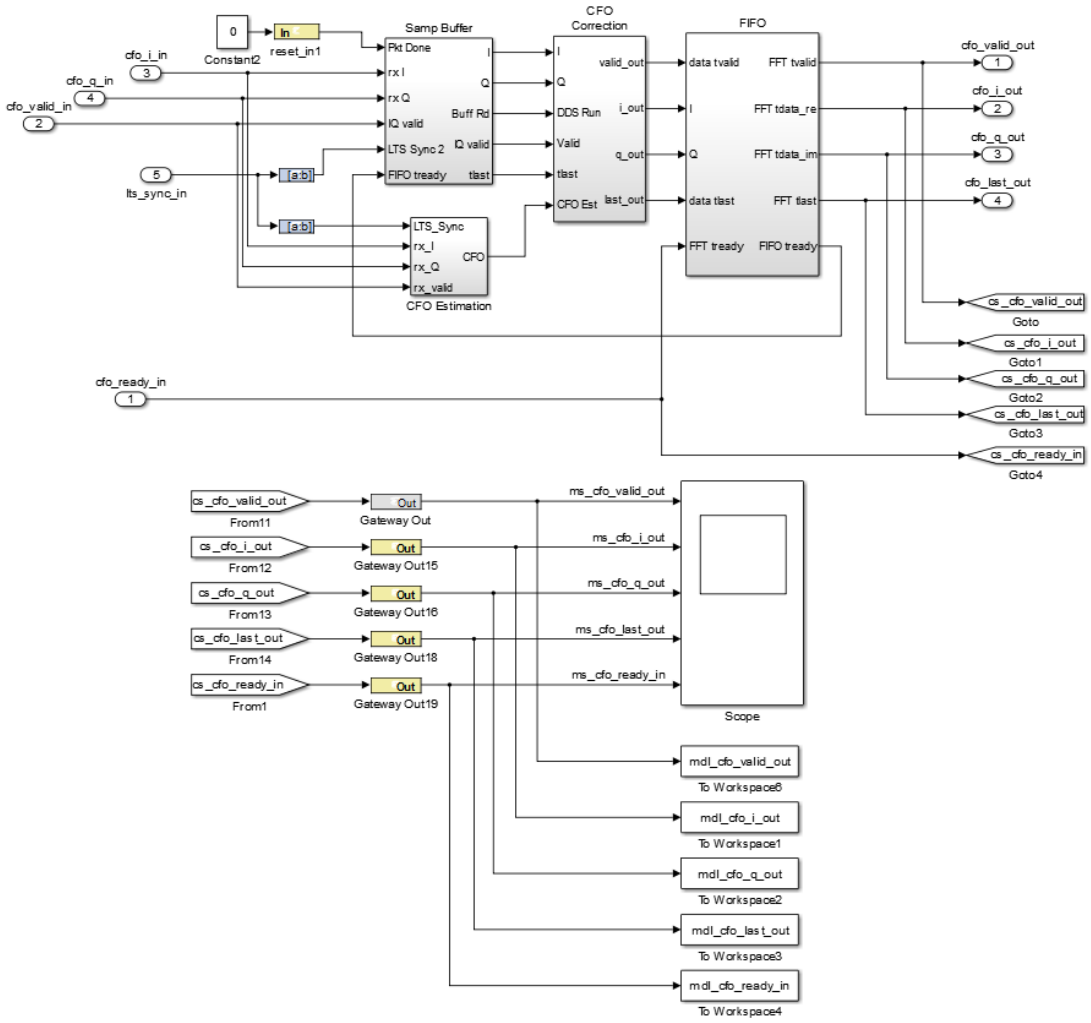

Figure A.9 CFO correction block [62]

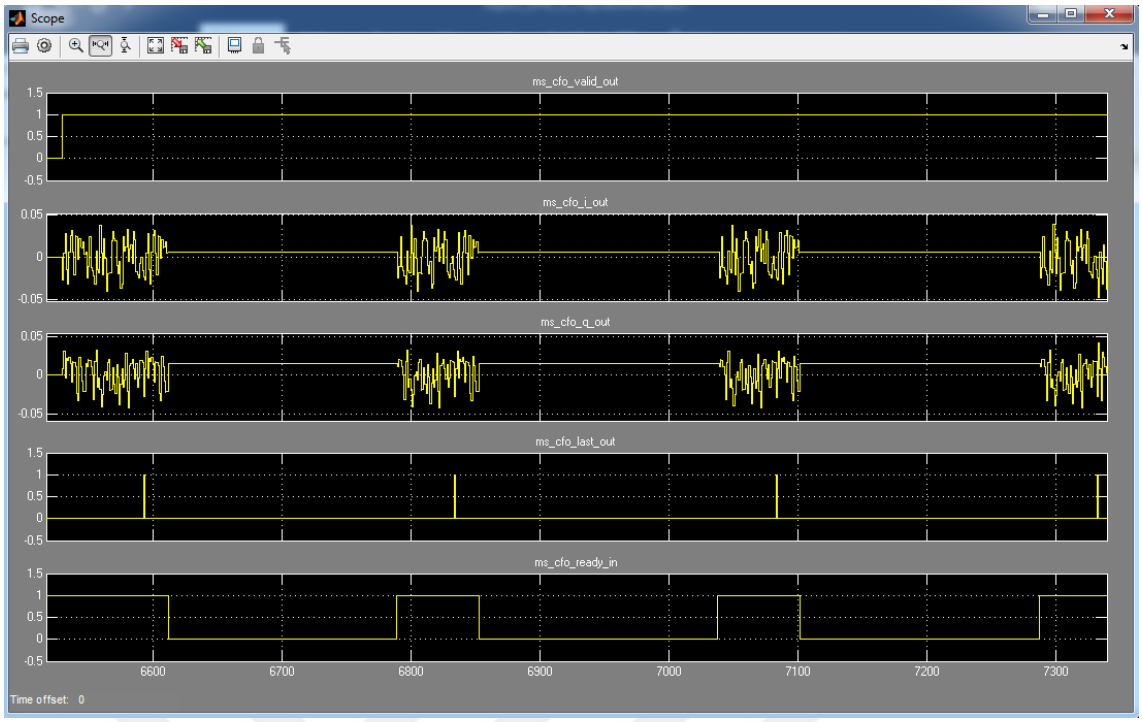

Figure A.10 Simulation of CFO correction block

Channel Estimator (channel_estimator) Block

Channel Estimator block estimates the channel coefficients by working on the CFO corrected LTS signals. As it is seen in Fig. A.11, LTS signals (ch_i_in, ch_q_in) are first converted into frequency-domain by employing FFT, and then channel estimation is performed in mult_by_LTS sub-block. In this sub-block, known LTS samples are stored in a ROM and the received LTS samples are compared with the known LTS samples for determining the channel coefficients. The determined channel coefficients in frequency-domain is converted back into time-domain by applying IFFT processing. Thus, the impulse response of the channel is ready to be used in the next block (td_r) where time-domain reconstruction takes place. In Fig. A.12, the 64-sample-length channel impulse response signals (ms_ch_h_i_out, ms_ch_h_q_out) are plotted along with ms_ch_h_last_out signal indicating the end of the channel impulse response.

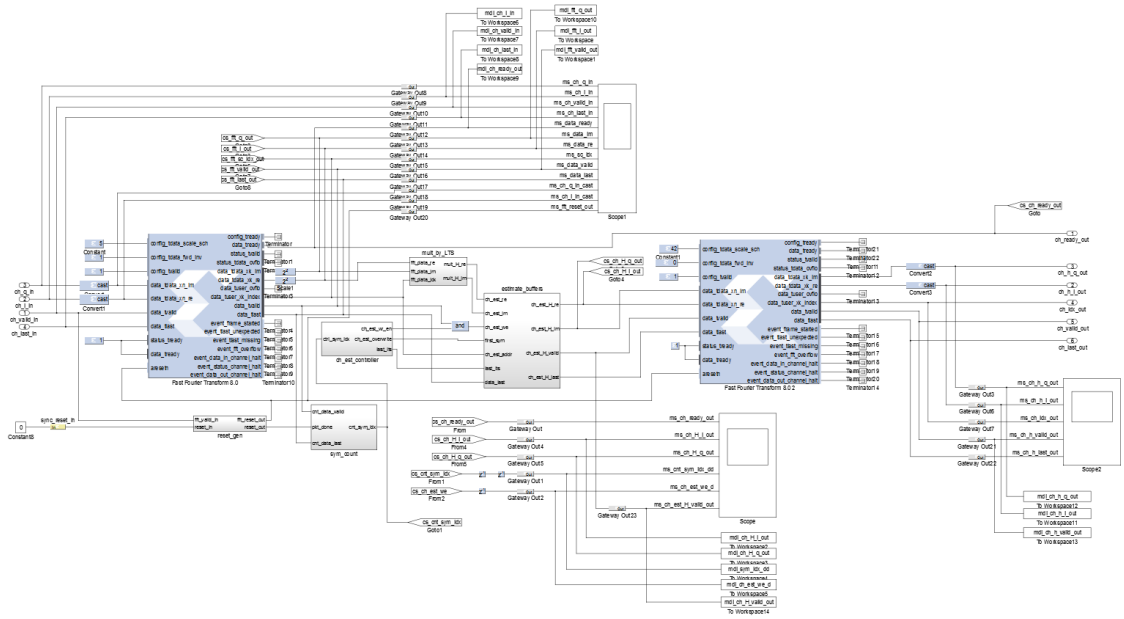

Figure A.11 Channel estimator block [62]

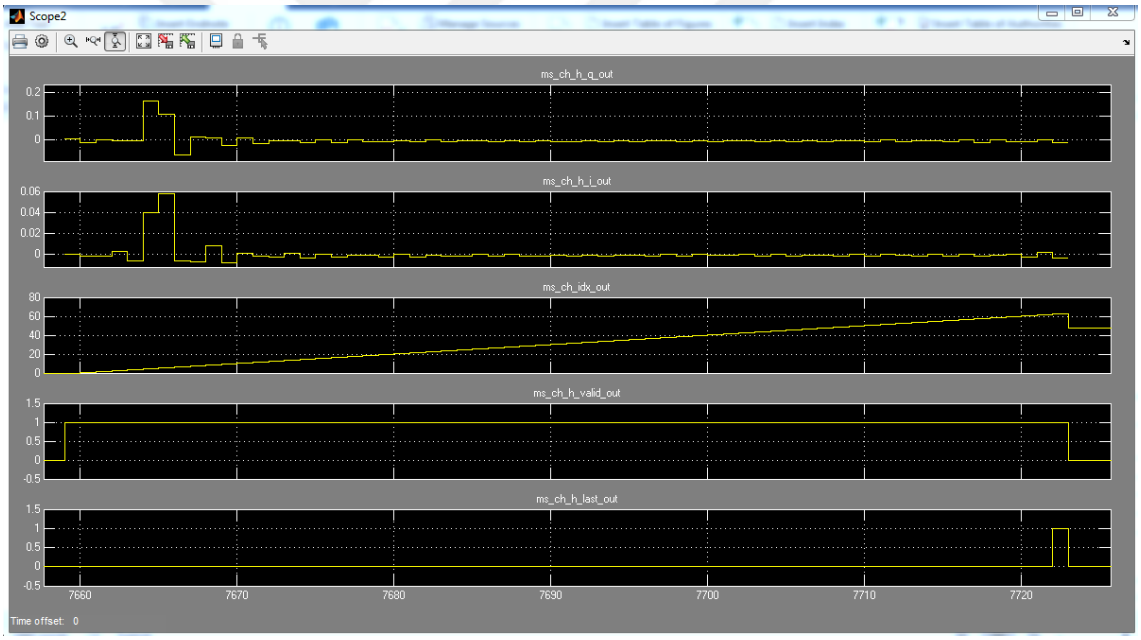

Figure A.12 Simulation of channel estimator block

Time-Domain Reconstruction (td_r) Block

The channel impulse response obtained in Channel Estimator is convoluted with the transmit signal stored in the transmit buffer (tx_buff) for reconstructing the SI signal. For this purpose, before the convolution operation, the coefficients of the convolution FIR filters in the td_r block shown in Fig. A.13 are loaded with the channel estimation impulse response (ch_i_in, ch_q_in) values. The sub-block that

performs this loading operation is the coeff_reload block. After loading the channel coefficients into the FIR filters, the td_r_config_done_out valid is asserted indicating the FIR filters are ready for convolution. This assertion triggers tx_buff block to provide the transmit signals (tx_buff_i_in, tx_buff_q_in) to the FIR filters as input for convolution; hence in-phase and quadrature of SI signal are reconstructed. Then they are up-sampled via interpolation filters. The amplitudes of the signals at the output of the interpolation filters are adjusted by rescaling and then the in-phase and quadrature signals are sent to the cancellation block. In Fig. A.14, simulation graphs are given for the reconstructed signals, ms_td_r_data_i_out and ms_td_r_data_q_out, in time-domain.

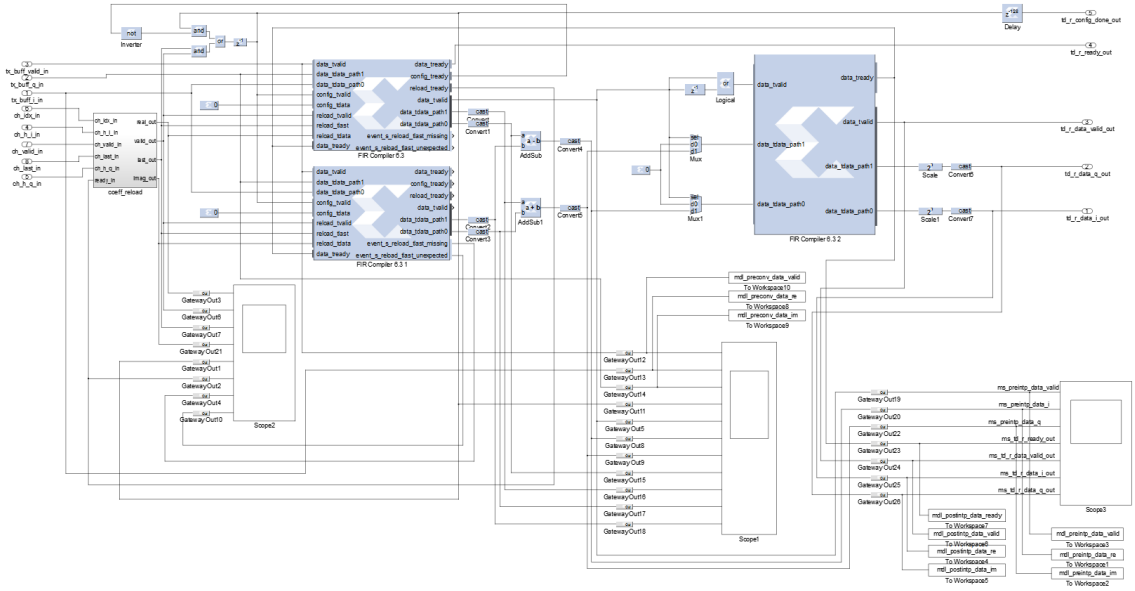

Figure A.13 Time-domain reconstruction block

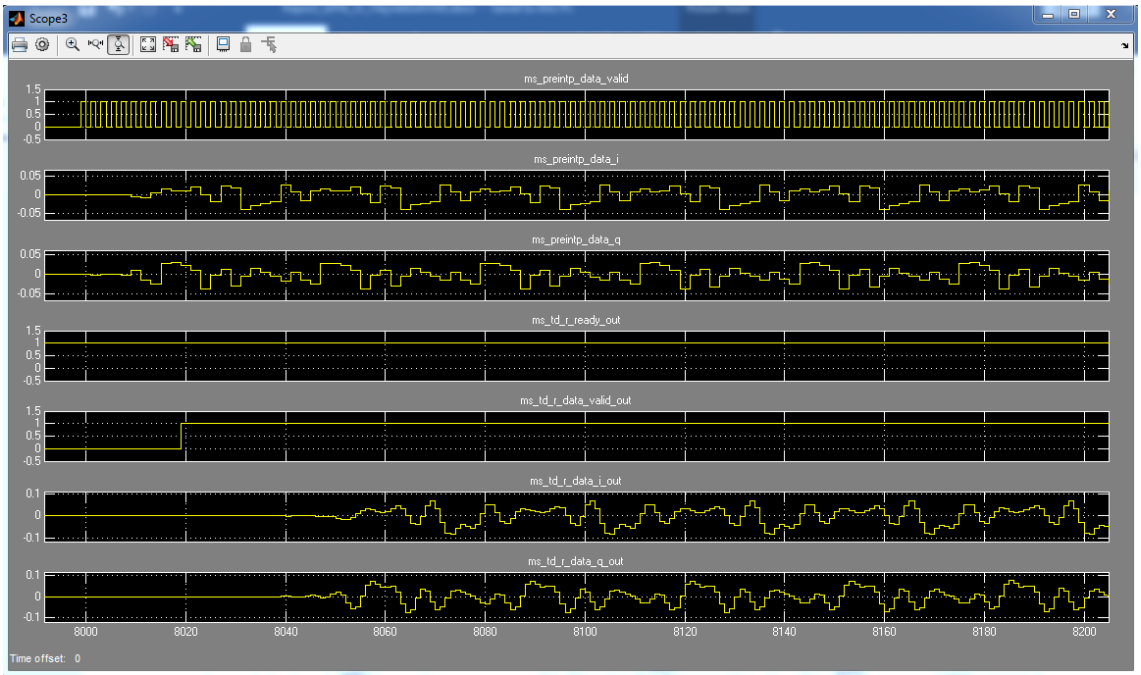

Figure A.14 Simulation of time-domain reconstruction block

Transmit Buffer (tx_buff) Block

The tx_buff block depicted in Fig. A.15 reads the transmit signals stored in the DDR memory and sends them to the td_r block. Signals (addr, wen, dout, enable) required to access DDR memory are generated in this block. Muxes are used for the selection of word swap and bit swap operations required on the WARPLab7 platform. The td_r_config_done_out valid signal from the td_r block triggers tx_buff, and as long as the td_r block is ready (tx_buff_ready_in), the address is incremented and the signals read from the DDR are sent to the td_r block (tx_buff_i_out, tx_buff_q_out).

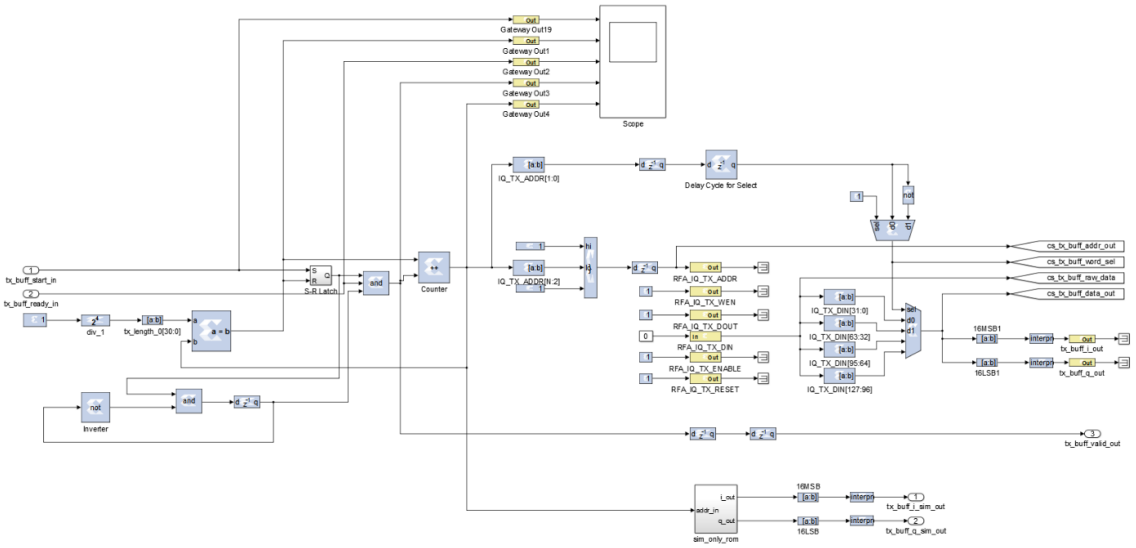

Figure A.15 Transmit buffer block [62]

Cancellation Block

SI cancellation takes place in the Cancellation block as shown in Fig. A.16. In the Cancellation block, dual-port RAMs are used to align the received SI signals (rx_data_i_in, rx_data_q_in) to the reconstructed SI signals (td_r_data_i_in, td_r_data_q_in) generated in td_r block. Triggered by the td_r_config_done_out valid signal arriving from the td_r block, the Cancellation block starts to read the received signals from the dual port RAMs by means of an address generator. Then, the reconstructed signals (td_r_data_i_in, td_r_data_q_in) are subtracted from the received signals. In the simulation graph in Fig. A.17, the residual ms_res_data_i_out and ms_data_q_out signals after subtraction appear to be close to zero.

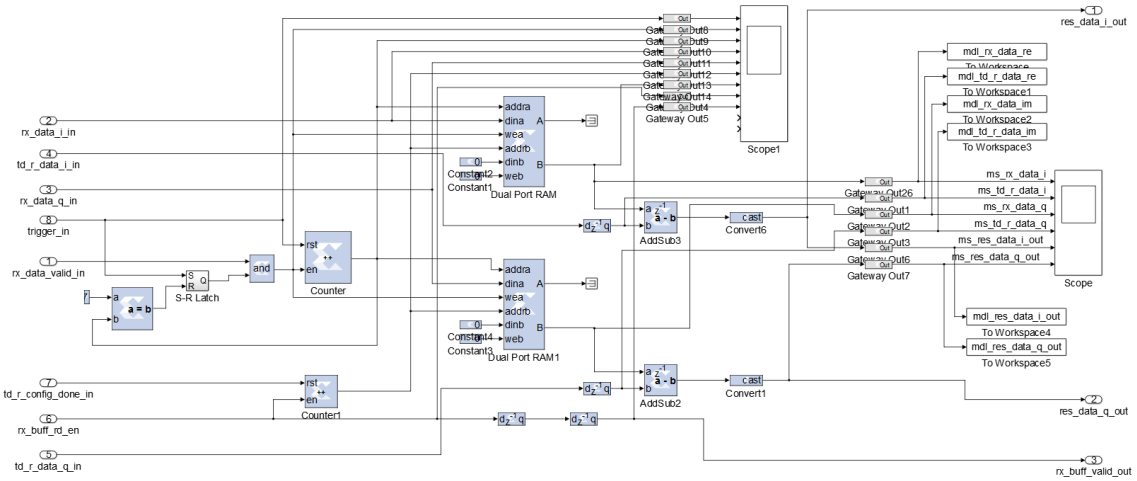

Figure A.16 Cancellation block

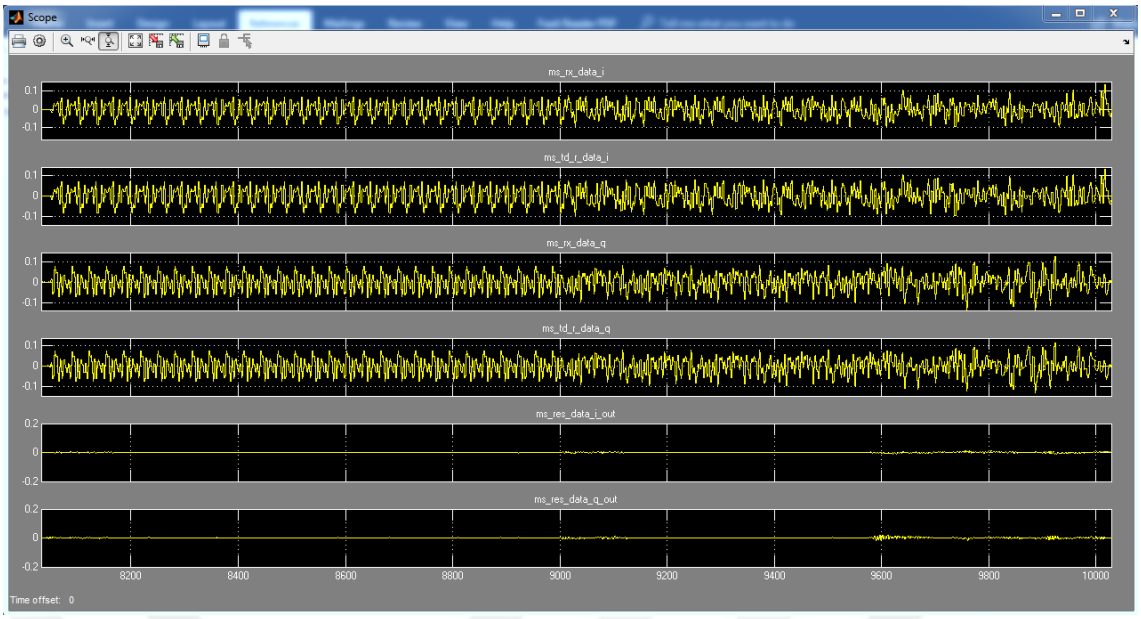

Figure A.17 Simulation of cancellation block

Verification of FPGA Implementation with MATLAB Results

In si_cancellation, the simulation results for the signals are transferred to the MATLAB workspace with prefix "mdl_" as explained in the previous section. By means of a separate .m file, Fig. A.18 - Fig. A.22 are generated where the signals obtained at the output of decimator, CFO correction, channel estimator, time domain reconstruction and cancellation blocks from hardware implementation along with the corresponding signals obtained from the algorithm are plotted. It is seen from the figures that the implementation signals and the algorithm signals are completely overlapping. This means that the implementation model is ready to be converted into HDL format by means of XSG. After the conversion, si_cancellation module is integrated with WARPLab7 framework and synthesized in the XPS environment, and then the whole implementation is embedded into the FPGA. In the following, as an example, code lines in the .m file for decimator block are provided:

```
mdl_dec_in = mdl_dec_i_in(find(mdl_dec_valid_in))+i*mdl_dec_q_in(find(mdl_dec_valid_in));
mdl_dec_out= mdl_dec_i_out(find(mdl_dec_valid_out))+i*mdl_dec_q_out(find(mdl_dec_valid_out));

dec_matlab = filter(interp_filt2, 1, mdl_dec_in);
dec_matlab = dec_matlab/4; % binary point adjustment for decimator out (Fix_16_15)
dec_matlab = dec_matlab(1:2:end);

figure(1)
subplot(2,1,1);
plot(real(dec_matlab),'r','LineWidth',2);
hold on
plot(real(mdl_dec_out),'b','LineWidth',1);
title('Decimator Real Output');
xlabel('sample');
ylabel('i');
legend('matlab algorithm', 'implementation')
subplot(2,1,2);
plot(imag(dec_matlab),'r','LineWidth',2);
hold on
plot(imag(mdl_dec_out),'b','LineWidth',1);
title('Decimator Imaginary Output');
xlabel('sample');
ylabel('q');
legend('matlab algorithm', 'implementation')
```

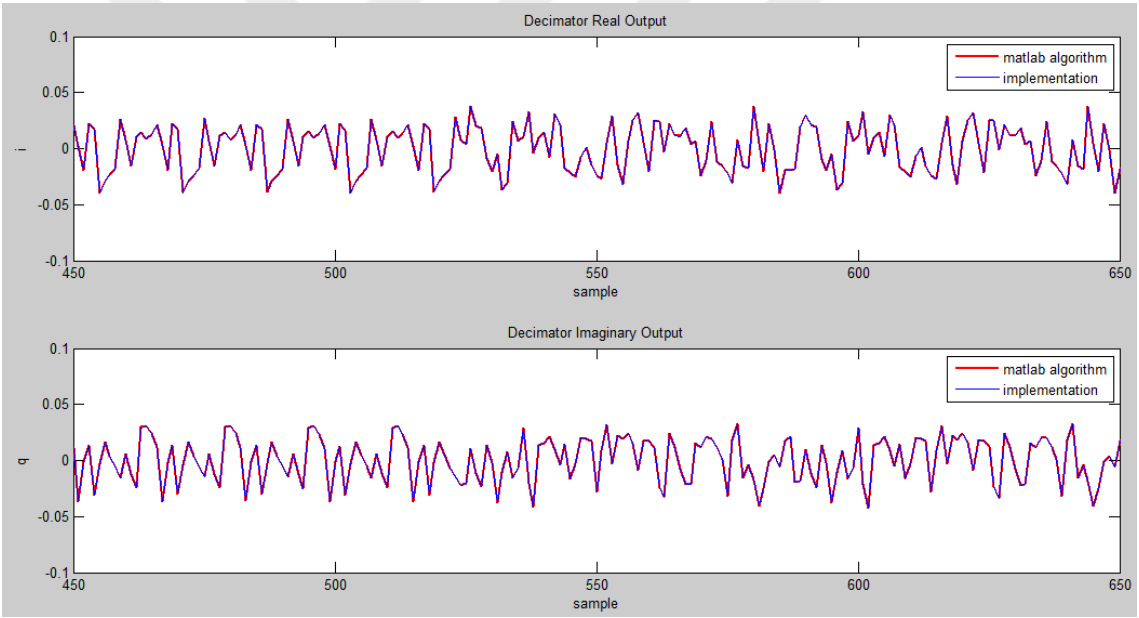

Figure A.18 Signals from decimator block

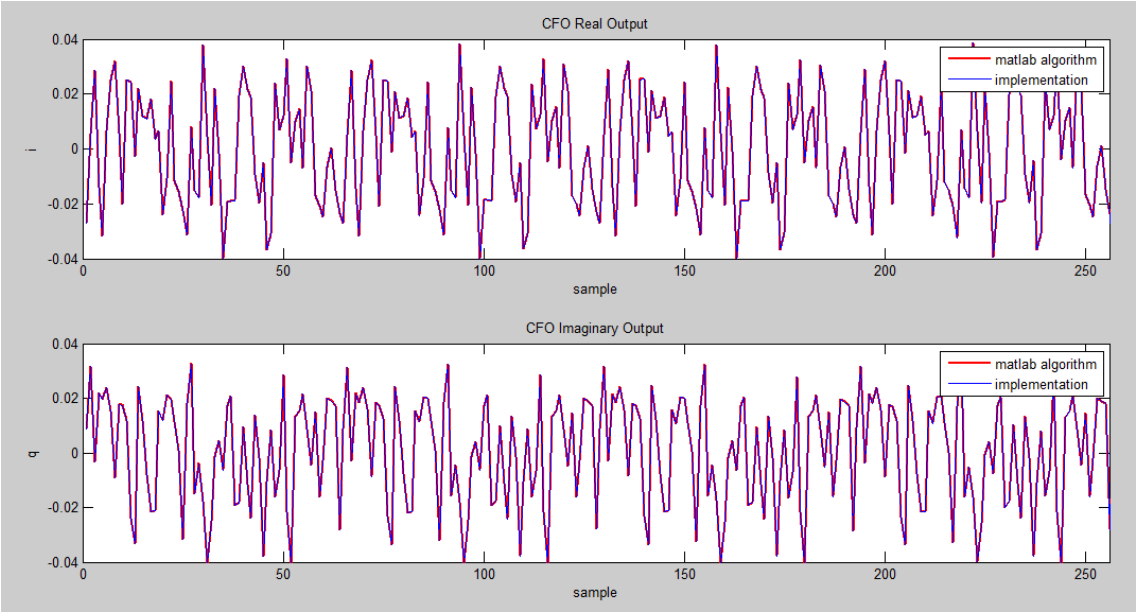

Figure A.19 Signals from CFO correction block

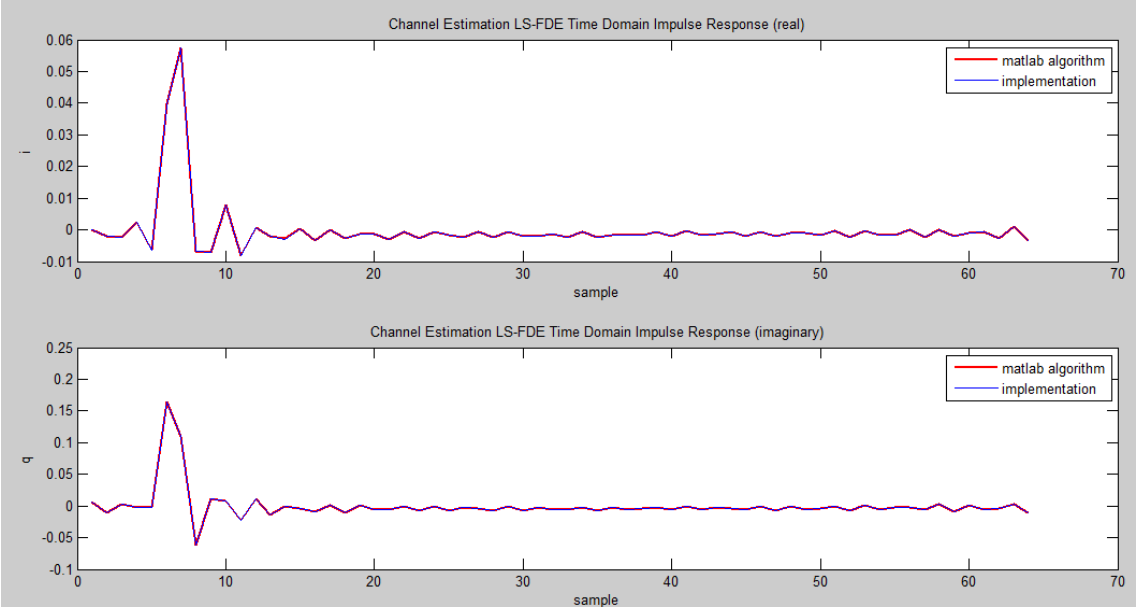

Figure A.20 Signals from channel estimator block in time-domain

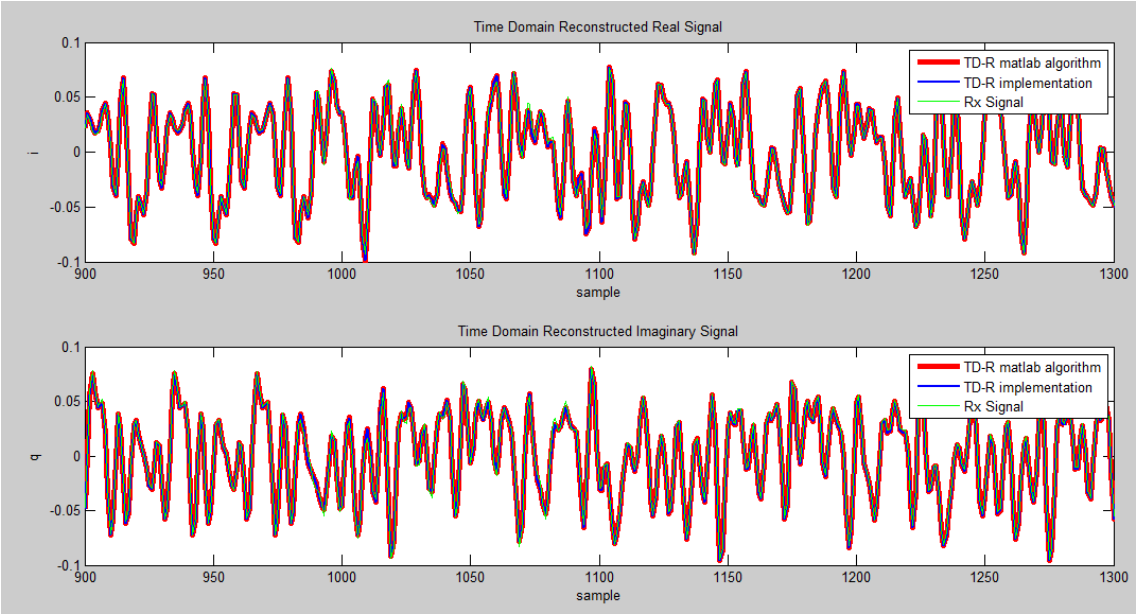

Figure A.21 Signals from time-domain reconstruction block

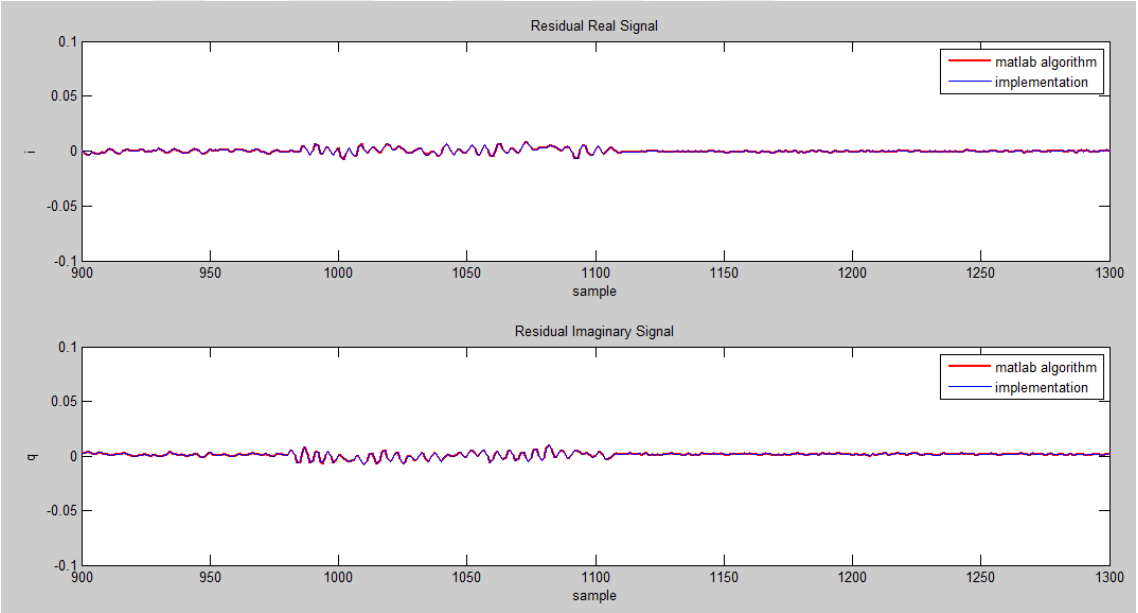

Figure A.22 Signals from cancellation block

Integration of FPGA Implementation with WARP Board

The si_cancellation module in HDL format is integrated into the existing FPGA implementation of WARPLab7 framework by using the XPS tool. For this purpose, firstly, it is connected to the PLB bus of the Microblaze processor in FPGA to be able to communicate with the processor. Connections of other ports with ADC and memory units are accomplished. Then, a suitable address range is assigned to the si_cancellation module. After the entire hardware environment is prepared in the XPS tool, the synthesis process is started for generating a bare hardware .bit file without containing driver software. In the next step of the flow, using the SDK tool, the bare hardware and the necessary driver software for the peripheral units are compiled together in order to generate a complete .bit file. The resulting .bit file is embedded in the FPGA on the board via the IMPACT tool. The real-time debugging of the implementation is performed by observing the signals connected to the chipscope as shown in Fig. A.23. At this point, via Chipscope Pro Analyzer tool, we plot the chipscope signals during the real-time operation. LTS correlation signal is given in Fig. A.24. The impulse responses of the estimated channel are shown in Fig. A.25 and Fig. A.26. Received and reconstructed signals are plotted in Fig. A.27 and Fig. A.28. In Fig. A.29 and Fig. A.30, the residual signal in the cancellation block and the received signal are presented together. After the debugging processes is completed, performance tests were carried out as explained in Section 3.4.2.

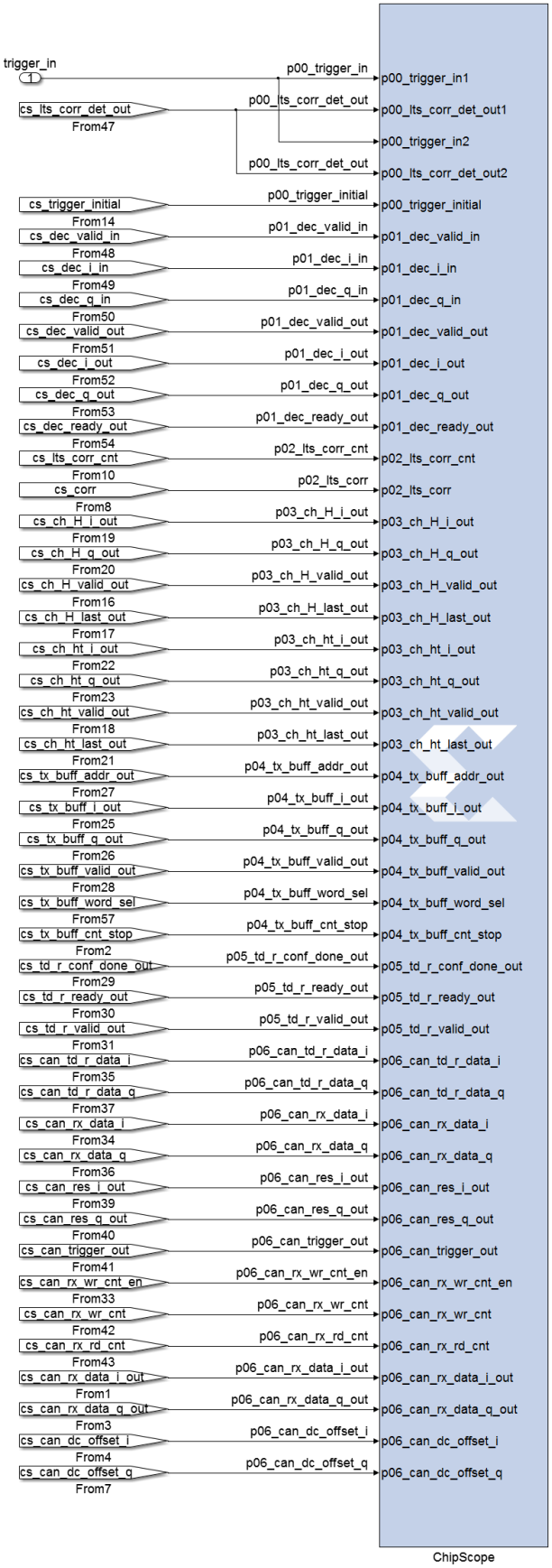

Figure A.23 Chipscope signals

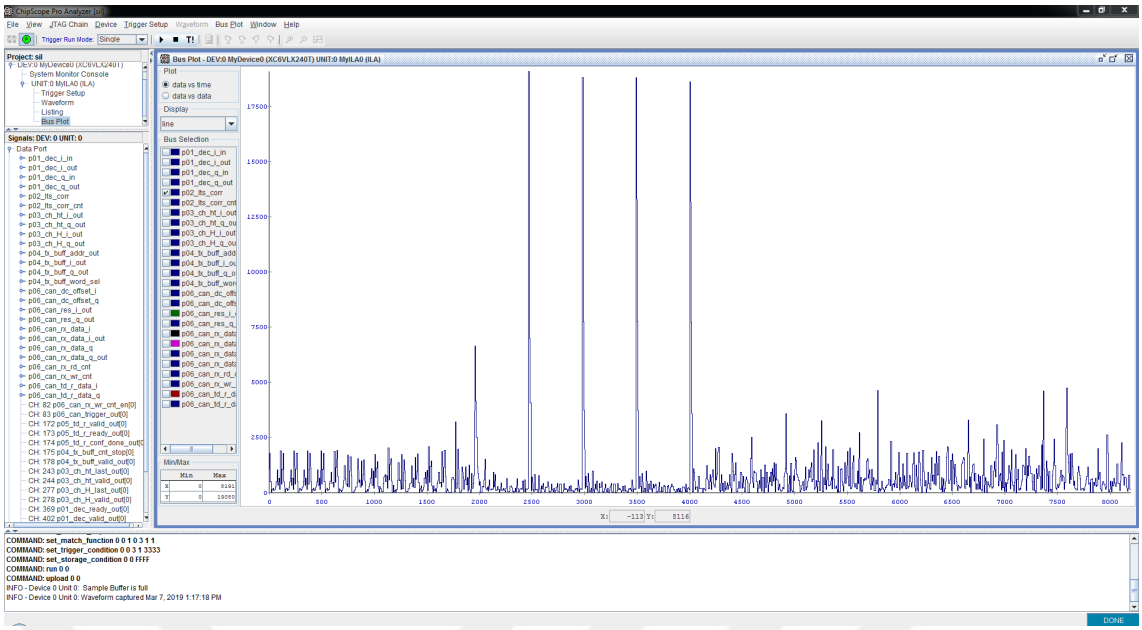

Figure A.24 LTS correlation signal obtained via chipscope (p02_lts_corr)

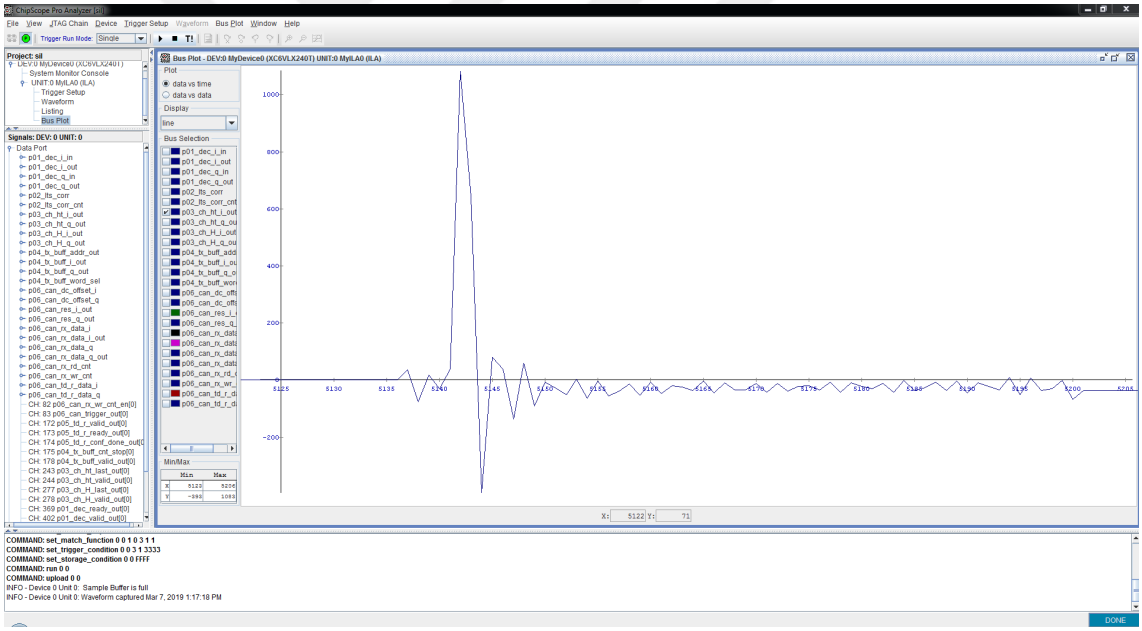

Figure A.25 In-phase of channel impulse response signal obtained via chipscope (p03_ch_ht_i_out)

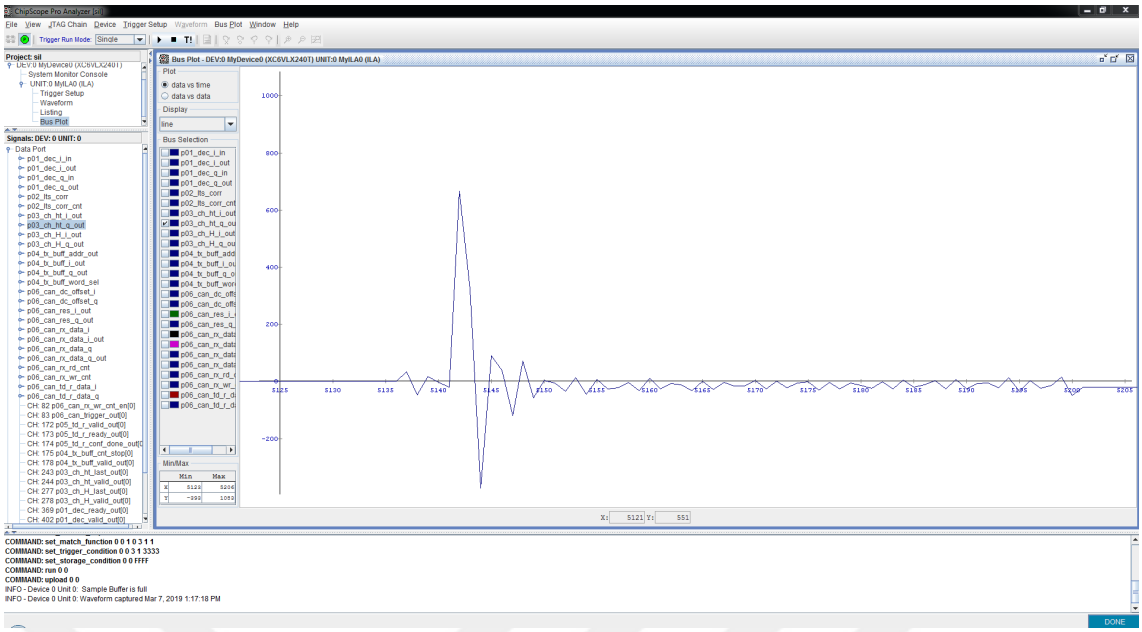

Figure A.26 Quadrature of channel impulse response signal obtained via chipscope (p03_ch_ht_q_out)

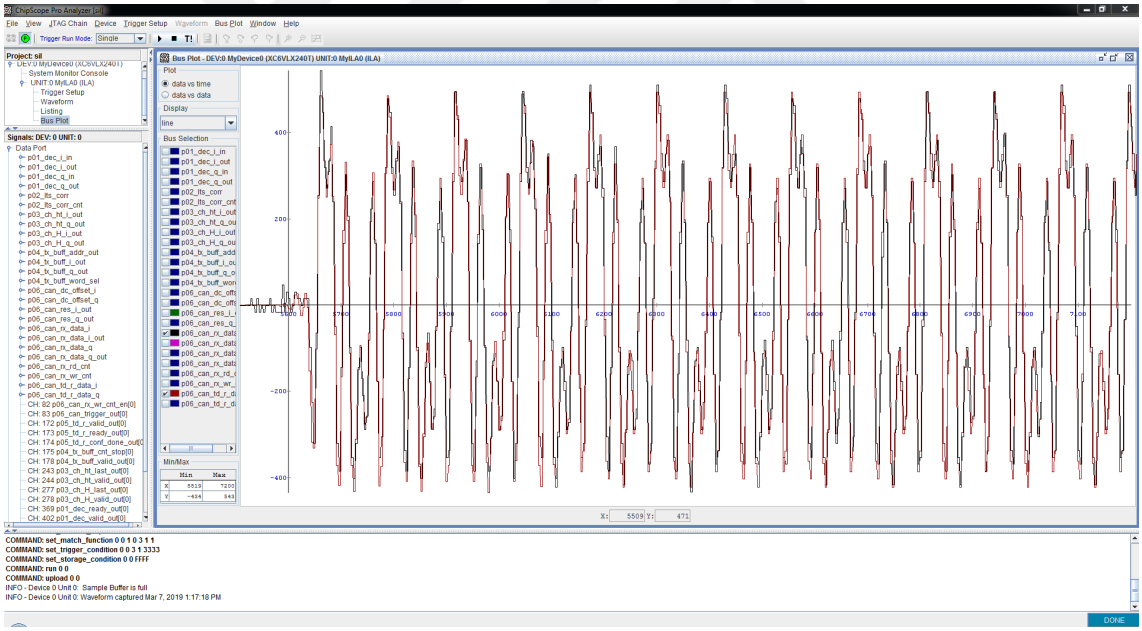

Figure A.27 In-phase of received and reconstructed signals obtained via chipscope (p06_can_rx_data_i, p06_can_td_r_data_i)

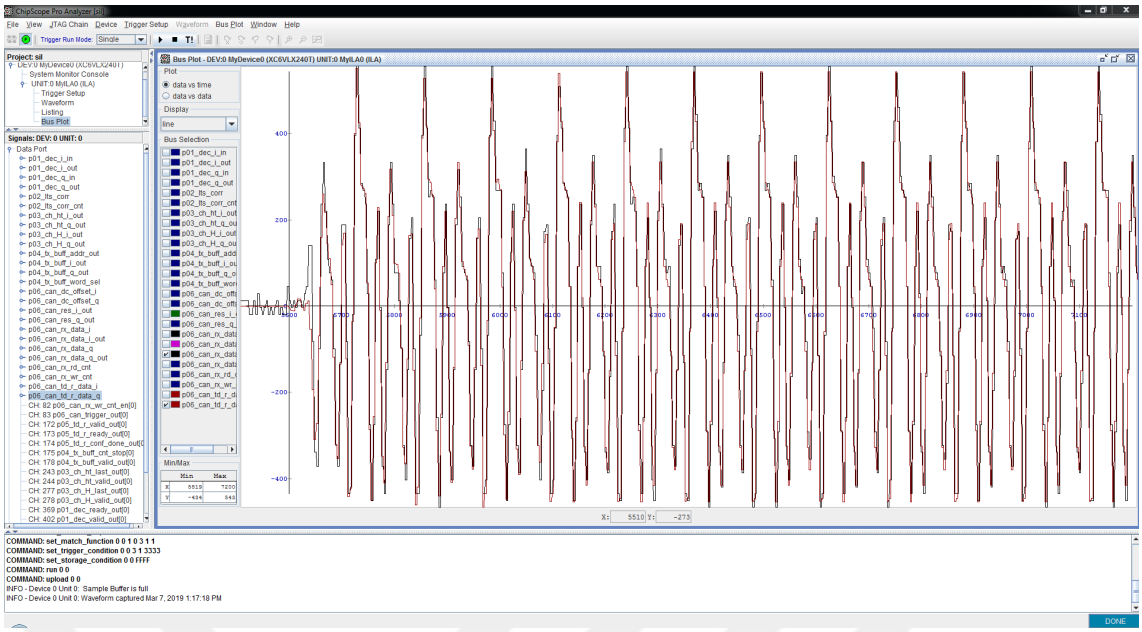

Figure A.28 Quadrature of received and reconstructed signals obtained via chipscope (p06_can_rx_data_q, p06_can_td_r_data_q)

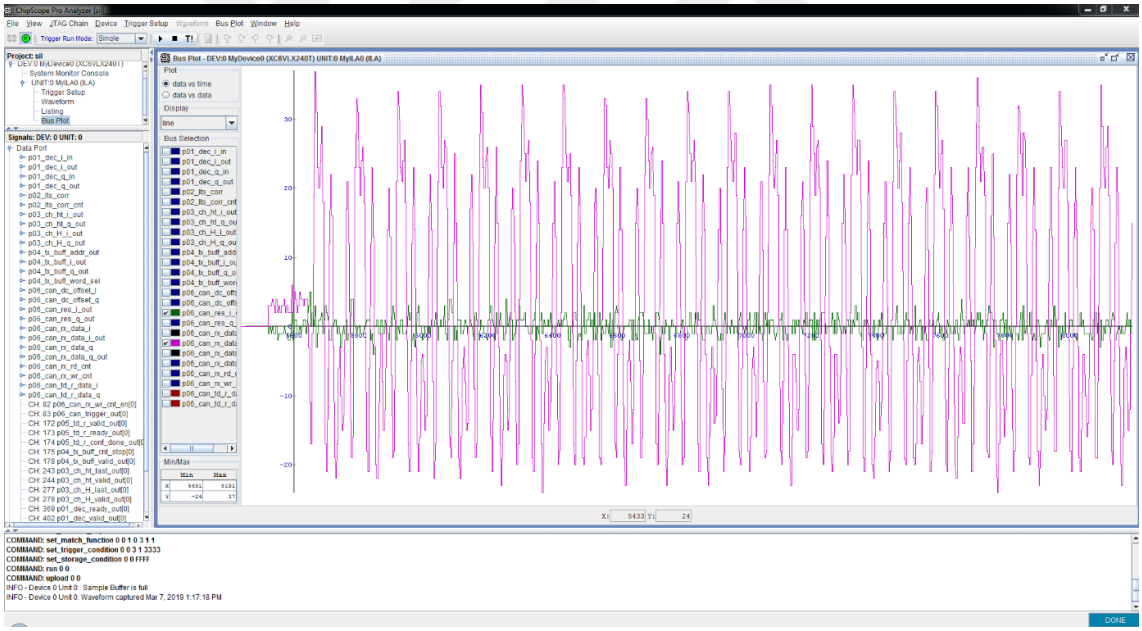

Figure A.29 In-phase of received and residual signals obtained via chipscope (p06_can_rx_data_i_out, p06_can_res_i_out)

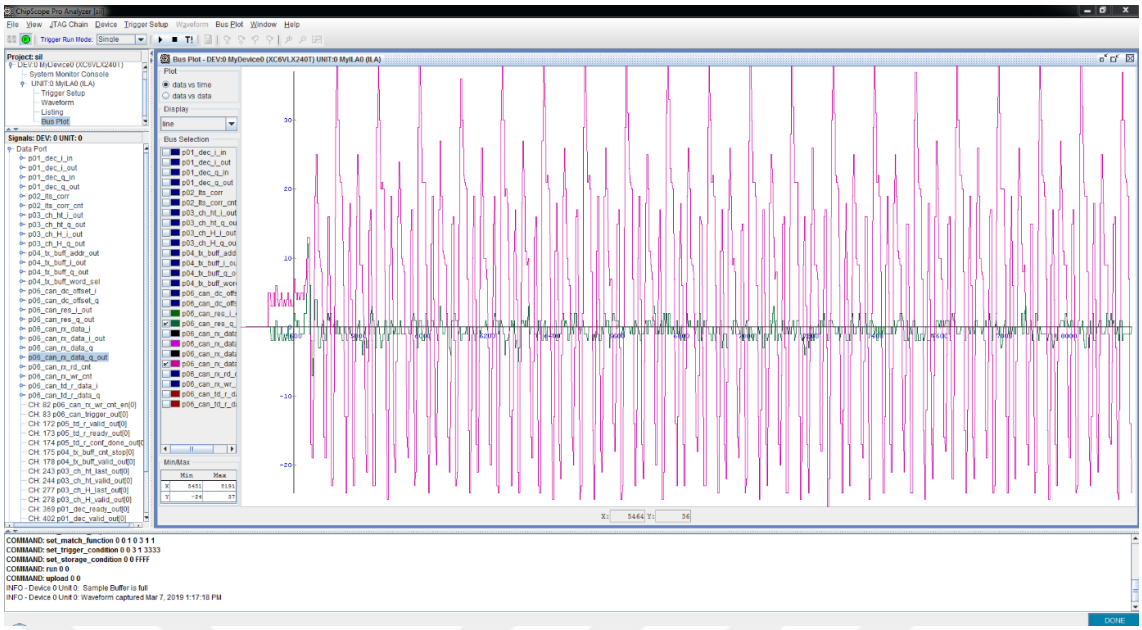

Figure A.30 Quadrature of received and residual signals obtained via chipscope (p06_can_rx_data_q_out, p06_can_res_q_out)

The experiments performed in Section 3.4.1 are repeated and the performance results are obtained by measuring the residual signal retrieved from the implementation. As it is shown in Fig. A.31, the Total SI suppression and EVM results obtained from MATLAB and FPGA implementations are overlap perfectly, with negligibly small deviations due to quantization errors.

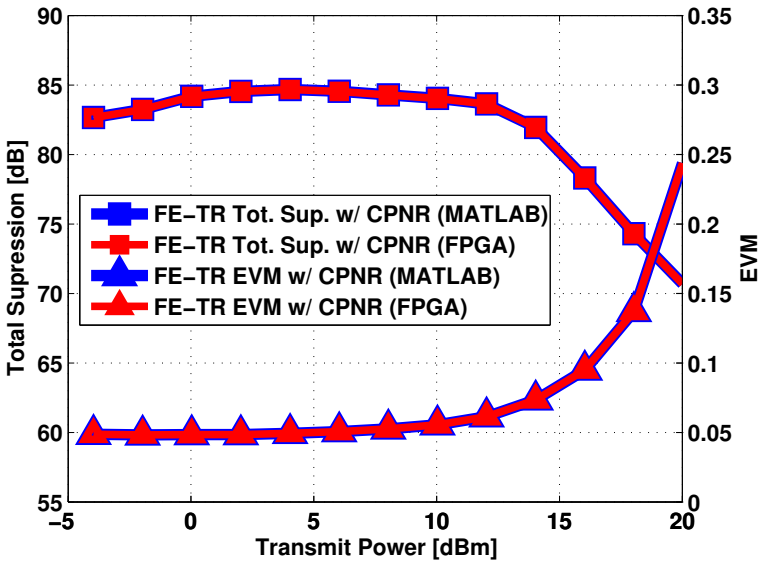

Figure A.31 Comparison of total SI suppression and EVM performances obtained from bidirectional communication experiment ($t_{\mathrm{p}} = 2.4\ \mu$s) for MATLAB and FPGA implementations.

Synthesis Report

The synthesis report obtained from the XPS tool is shown in Fig. A.32. The total number of flip flops used in the system is 74205, and the number of LUTs (look up tables) is 67254. The number of flip flops used by the si_cancellation block is 3606 and corresponds to 5 percent of the total number of flip flops used in the system. The number of LUTs used by the block is 2445, which is around 4 percent of the total number of LUTs used.

Project Status (03/07/2019 - 14:07:48)			
Project File:	system.xmp	**Implementation State:**	Programming File Generated
Module Name:	system	**•Errors:**	
Product Version:	EDK 14.4	**•Warnings:**	

XPS Reports				[-]
Report Name	**Generated**	**Errors**	**Warnings**	**Infos**
Platgen Log File	Wed Mar 6 08:46:50 2019	0	87 Warnings (47 new)	70 Infos (1 new)
Simgen Log File				
BitInit Log File				
System Log File	Wed Mar 6 10:54:26 2019			

XPS Synthesis Summary (estimated values)						[-]
Report	**Generated**	**Flip Flops Used**	**LUTs Used**	**BRAMS Used**	**Errors**	
system	Wed Mar 6 08:52:46 2019	74205	67254	370	0	
system_w3_userio_wrapper	Wed Mar 6 08:46:12 2019	614	985		0	
system_boot_jo_mux_wrapper	Wed Mar 6 08:45:56 2019		9		0	
system_clock_generator_mpmc_clocks_wrapper	Wed Mar 6 08:45:50 2019				0	
system_clock_generator_procbussamp_clocks_wrapper	Wed Mar 6 08:45:43 2019				0	
system_clock_generator_asyncclks_wrapper	Wed Mar 6 08:45:36 2019				0	
system_radio_controller_0_wrapper	Wed Mar 6 08:45:29 2019	1399	1997		0	
system_si_cancellation_axiw_0_wrapper	Wed Mar 6 08:44:46 2019	3606	2445		0	
system_w3_ad_bridge_onboard_wrapper	Wed Mar 6 08:44:25 2019	98	2		0	
system_w3_ad_controller_0_wrapper	Wed Mar 6 08:44:18 2019	587	1053		0	
system_w3_clock_controller_0_wrapper	Wed Mar 6 08:44:00 2019	461	631	1	0	
system_w3_iic_eeprom_onboard_wrapper	Wed Mar 6 08:43:47 2019	340	560		0	
system_axi_sysmon_adc_0_wrapper	Sun Mar 3 14:20:59 2019	183	237		0	
system_axi_timer_0_wrapper	Sun Mar 3 14:20:48 2019	222	323		0	
system_clk_gen_locked_and_wrapper	Sun Mar 3 14:20:30 2019		1		0	
system_debug_module_wrapper	Sun Mar 3 14:20:03 2019	69	49		0	
system_microblaze_0_wrapper	Sun Mar 3 14:19:54 2019	2377	2355		0	
system_microblaze_0_bram_block_wrapper	Sun Mar 3 14:19:10 2019			32	0	
system_microblaze_0_d_bram_ctrl_wrapper	Sun Mar 3 14:18:58 2019	2	6		0	
system_microblaze_0_dlmb_wrapper	Sun Mar 3 14:18:51 2019	1			0	
system_microblaze_0_i_bram_ctrl_wrapper	Sun Mar 3 14:18:44 2019	2	6		0	
system_microblaze_0_ilmb_wrapper	Sun Mar 3 14:18:37 2019	1			0	
system_proc_sys_reset_0_wrapper	Sun Mar 3 14:18:30 2019	69	56		0	
system_rfa_iq_rx_buffer_wrapper	Sun Mar 3 14:17:38 2019			32	0	
system_rfa_iq_rx_buffer_ctrl_wrapper	Sun Mar 3 14:17:26 2019	575	419		0	
system_rfa_iq_tx_buffer_wrapper	Sun Mar 3 14:17:14 2019			32	0	
system_rfa_iq_tx_buffer_ctrl_wrapper	Sun Mar 3 14:17:02 2019	575	419		0	
system_rfa_rssi_buffer_wrapper	Sun Mar 3 14:16:51 2019			4	0	
system_rfa_rssi_buffer_ctrl_wrapper	Sun Mar 3 14:16:43 2019	575	419		0	
system_rfb_iq_rx_buffer_wrapper	Sun Mar 3 14:16:32 2019			32	0	
system_rfb_iq_rx_buffer_ctrl_wrapper	Sun Mar 3 14:16:19 2019	575	419		0	
system_rfb_iq_tx_buffer_wrapper	Sun Mar 3 14:16:08 2019			32	0	
system_rfb_iq_tx_buffer_ctrl_wrapper	Sun Mar 3 14:15:54 2019	575	419		0	
system_rfb_rssi_buffer_wrapper	Sun Mar 3 14:15:41 2019			4	0	
system_rfb_rssi_buffer_ctrl_wrapper	Sun Mar 3 14:15:33 2019	575	419		0	
system_usb_uart_wrapper	Sun Mar 3 14:14:59 2019	85	109		0	

Figure A.32 XPS synthesis report for si_cancellation module

APPENDIX B: Optimization of Non-Linear Model Parameters for Switched IBFD Radio

A. Optimization for Time-Domain Non-Linear Estimation

We have implemented the IBFD-SW architecture on our SDR based IBFD radio set-up as described in Section III and shown in Fig. 4.5, and we have conducted experiments by employing the MP model in (2.13), considering various polynomial order (P), memory length (M), and training length (L) values, to determine the optimal settings providing the highest total suppression at all transmit power levels.

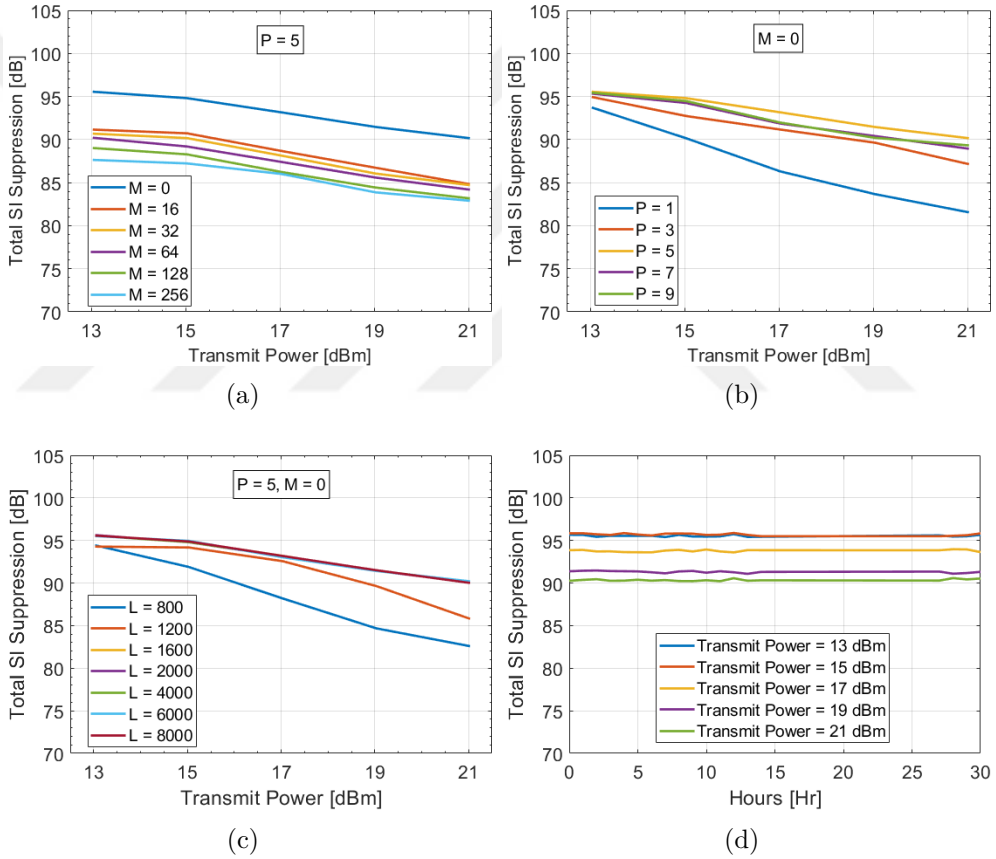

Figure B.1 Evaluation of total SI suppression performance for the proposed IBFD-SW radio architecture with employing MP model for various P, M and L values (a) $P = 5$ and $L = 4000$ (b) $M = 0$ and $L = 4000$ (c) $P = 5$ and $M = 0$ (d) Observation of total SI suppression performance with stored non-linear coefficients during 30 hours with optimum parameters ($P = 5$, $M = 0$, $L = 1600$)

In Fig. B.1 (a), P is set as 5 and L is provided as 4000 samples, and the amount of total SI suppression is plotted as a function of transmit power for different values of M. Here, in this test, the highest performance is observed when $M = 0$. Next,

in Fig. B.1 (b), by setting M as 0 and keeping L as 4000 samples, the amount of total SI suppression is plotted for different values of P. In this figure, the highest total SI suppression performance for all the transmit power levels is achieved for $P = 5$. Finally, in Fig. B.1 (c), having set $P = 5$ and $M = 0$, different values of L are considered while observing the total SI suppression. For $L = 1600$, the total SI suppression reaches up to its highest value, and beyond 1600 samples it remains the same. Consequently, the MP model in (2.13) is simplified to (4.1) in our proposed IBFD-SW architecture. Hence, with the optimized parameters, the required computation for the model in (4.1) is reduced to estimating only the c_i coefficients during the estimation phase. In the next experiment, by applying the optimum parameters in (4.1), we have obtained the model coefficients, c_i's and stored them after the initial transmission. Then, we have reused the stored coefficients in the subsequent transmissions for 30 hours, considering different (high) power levels, as depicted in Fig. B.1 (d). The performance for each transmit power does not change with time, indicating that re-estimation of non-linear coefficients is not required.

B. Optimization for Frequency-Domain Non-Linear Estimation

For NLF, we have observed the effect of number of neurons in the MSE performance and found that the performance is not effected after 5 neurons. On the other hand, for weight adaptation of each layer, various numerical optimization algorithms have been utilized in the literature such as gradient descent, resilient propagation, conjugate gradient, bayesian regularization, one step secant, Levenberg-Marquardt, etc.. The MSE performance of different algorithms is observed under the same condition by setting the number of neurons as 5 and by applying up to 8000 training samples. Among the rest of the algorithms, Levenberg-Marquardt algorithm is shownn to provide lowest MSE value with the fastest convergence rate which is 2400 samples. The activation function, f, used in the neurons is *tansig* function expressed as $tansig(x) = (e^x - e^{-x})/(e^x + e^{-x})$.

APPENDIX C: Validation of Results for IBFD Radio with Auxiliary Receive Chain

The IBFD-AUX radio implemented on our SDR set-up is capable of suppressing the SI signal to the noise floor of the WARP v3 board. We prove this by comparing the amount of total SI suppression performance in Fig. C.1 (a) with the digital SI cancellation values depicted in Fig. C.1 (b) obtained in [3]. First we utilize the measured received signal strength indicator (RSSI) value from Fig. C.1 (c), which indicates the power of SI signal remaining after the passive SI suppression from transmit port to the receive port. Then, to obtain the SNR value, we calculate the difference between RSSI and the noise floor of WARP v3 board which is -85 dBm. We read the digital SI cancellation amount from Fig. C.1 (b) corresponding to the calculated SNR and add this value to the amount of antenna suppression which is 73 dB to calculate the total SI suppression. Ultimately, we compare the measured total SI suppression with the calculated total SI suppression. All measurement and simulation values for high transmit power settings can be found in Table C.1 and an illustration of total SI suppression performance for various transmit power settings is depicted in Fig. C.1 (c). As an example, at 5 dBm transmit power setting, the measured RSSI value is -68 dBm and the difference between RSSI value and the noise floor is 17 dB (SNR) and we obtain 17 dB digital SI cancellation performance corresponding to this SNR value from Fig. C.1 (b). Adding 73 dB antenna suppression to 17 dB digital SI cancellation results in 90 dB total SI suppression. The calculated total SI suppression value is same as the maximum measured total SI suppression amount given in Fig. C.1 (a). However, as the transmit power level is increased beyond 15 dBm, due to saturation of received signal appearing as RSSI values between -56.5 and -54.5 dBm as plotted in Fig. C.1 (c), the SNR value is limited around a certain value which limits the performance of linear SI cancellation.

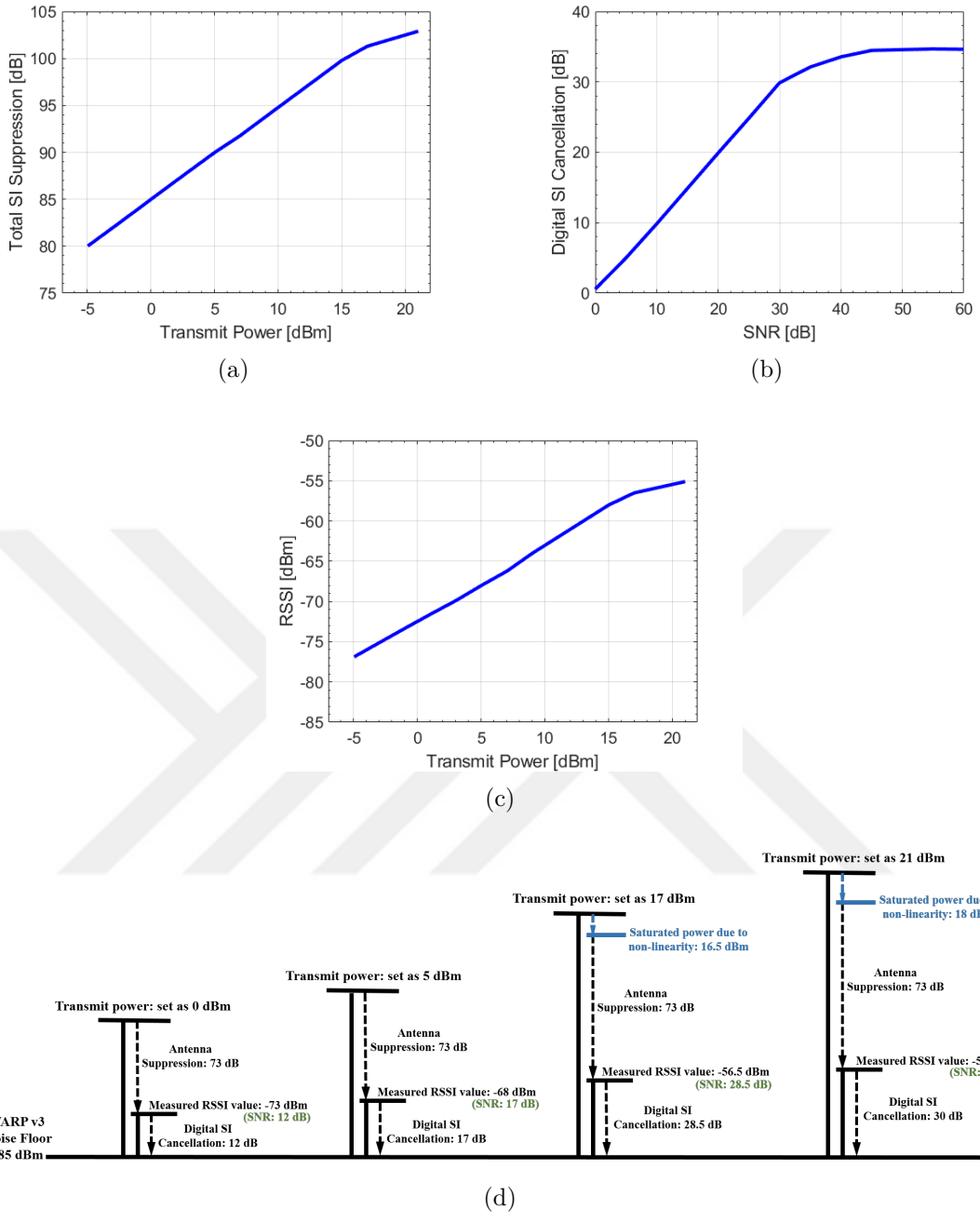

Figure C.1 (a) Measured total SI suppression performance on IBFD-AUX with TE-TR (b) Digital SI cancellation performance obtained from simulations for TE-TR (c) Measured received signal strength indicator (RSSI) at the receiver (d) Illustration of total SI suppression for various transmit power settings

Table C.1 Values from measurements and simulations for IBFD-AUX with TE-TR

Antenna Suppression: 73 dB					
Transmit Power [dBm] (set as)	RSSI [dBm]	SNR [dB]	Digital SI Cancellation [dB]	Residual Signal Power [dBm]	Total Suppression [dB]
11	-62	23	23	-85	96
13	-60	25	25	-85	98
15	-58	27	27	-85	100
17	-56.5	28.5	28.5	-85	101.5
19	-56	29	29	-85	102
21	-55	30	30	-85	103